

Series 01 Aerodynamics 09

Orientation on Quantitative IR-thermography in Wall-shear Stress Measurements

R. Mayer



Delft University Press

706381

Orientation on Quantitative
IR-thermography in Wall-shear
Stress Measurements

Bibliotheek TU Delft



C 3021858

2392
349
2



Orientation on Quantitative IR-thermography in Wall-shear Stress Measurements

R. Mayer



Delft University Press / 1998

Published and distributed by:

Delft University Press
Mekelweg 4
2628 CD Delft
The Netherlands
Telephone +31 (0)15 278 32 54
Fax +31 (0)15 278 16 61
e-mail: DUP@DUP.TUdelft.NL

by order of:

Faculty of Aerospace Engineering
Delft University of Technology
Kluyverweg 1
P.O. Box 5058
2600 GB Delft
The Netherlands
Telephone +31 (0)15 278 14 55
Fax +31 (0)15 278 18 22
e-mail: Secretariaat@LR.TUdelft.NL
website: <http://www.lr.tudelft.nl/>

Cover: Aerospace Design Studio, 66.5 x 45.5 cm, by:
Fer Hakkaart, Dullenbakkersteeg 3, 2312 HP Leiden, The Netherlands
Tel. +31 (0)71 512 67 25

90-407-1572-6

Copyright © 1998 by Faculty of Aerospace Engineering

All rights reserved.

No part of the material protected by this copyright notice may be reproduced or utilized in any form or by any means, electronic or mechanical, including photocopying, recording or by any information storage and retrieval system, without written permission from the publisher: Delft University Press.

Printed in The Netherlands

Contents

1	Introduction	1
1.1	Role of the wall-shear stress	1
1.2	Measurement techniques	2
1.3	Quantitative infrared thermography in wall-shear stress measurements	2
1.4	Aim of the report	4
1.5	Outline of the report	4
2	Basics of mass, momentum and energy transport	5
2.1	Phenomena of fluid motion	5
2.2	Navier-Stokes equation	8
2.3	Boundary layer equations	9
2.4	Characteristic numbers	11
2.5	Similarity equations	11
3	Wall-shear stress measurement techniques	15
3.1	Mechanical methods	15
3.2	Tracer methods	17
3.3	Thermal methods	18
4	Theory of heat transfer mechanisms	21
4.1	Heat transfer in fluids	21
4.1.1	Arbitrary wall temperature	24
4.2	Heat transfer in solids	25
4.2.1	Steady approach	25
4.2.2	Unsteady approach	26
4.3	Thermal radiation	29
5	Experimental aspects	33
5.1	Temperature measurements	33

CONTENTS

5.1.1	Resistance temperature detectors	34
5.1.2	Thermocouples	34
5.1.3	RTD measurement check	36
5.2	IR-camera	37
5.2.1	Sensor	37
5.2.2	Scanning system	39
5.2.3	Focussing	42
5.3	Quantitative IR-Thermography	44
5.3.1	Split response function	44
5.3.2	Modulation transfer function	45
5.3.3	Time response	46
5.3.4	Emissivity of real objects	48
5.4	Experimental setup	51
5.4.1	IR-Camera operating module	53
5.4.2	Laser	54
5.5	Calibration procedure	56
5.6	Laser irradiation measurement	60
6	Numerical analysis	62
6.1	Data acquisition	62
6.1.1	Format of the BRUT output file	62
6.1.2	Raw data manipulation	64
6.1.3	Data-processing program BRUT_S	66
6.2	Numerical calculation of heat transfer in solids	69
6.3	Wall-shear stress calculation	72
7	Results	75
7.1	Test plate	75
7.2	Preliminary experiments	76
7.2.1	Temperature decay	89
7.3	Numerical calculations	91
7.3.1	Thermal properties of the solid	91
7.3.2	Thermal boundary conditions	93
7.4	Wall-shear stress measurement	97
8	Conclusions	99
	Reference	102

SUMMARY

Wall-shear stresses are highly important in the aerodynamic design of aircraft, because they determine the drag and thus the fuel consumption of an airplane. Due to this importance many different measurement techniques have been developed. Most of these techniques are intrusive, which means that the flow is disturbed by the presence of a measurement probe. The hot film technique is non-intrusive, because hot films measure the heat transfer from an electrical heated surface of an object to the flow, which is related to the wall-shear stress. Using the theory of the hot film technique, we have developed a new non-intrusive wall-shear stress measurement technique, which is based on quantitative IR-thermography. In this technique a hot spot is externally generated by a laser. The surface temperature measurements, from which the heat flux to the flow is derived, is measured externally by an IR-camera. The external heating and the external temperature measurement provides three main advantages:

- o the measurement is non-intrusive
- o the measurement point can easily be varied
- o this technique can be applied in flight tests

This measurement technique has been tested for a laminar flow along a flat plate in a wind-tunnel. The laser generates a hot spot on the plate until the steady state condition is reached. After turning off the laser the IR-camera monitors the temperature decay. From these data the heat flux to the flow and the wall-shear stress can be derived.

The results show that it is indeed possible to apply quantitative IR-thermography to measure local wall-shear stresses. The obtained accuracy of the measurement technique is $\pm 10\%$ for free stream velocities larger than 10 m/s . However it has to be noted that this technique has some limitations due to the capabilities of the IR-camera, such as the spatial resolution and the signal to noise ratio.

In the near future this measurement technique will be extended to flows with non-zero pressure gradients and with turbulence.

NOMENCLATURE

symbols	quantity		unit
a	thermal diffusivity		m^2/s
Bi	Biot number	$Bi = \alpha h/k$	
c	speed of sound		m/s
c_0	speed of light in vacuum	$c_0 = 2.99 \times 10^8$	m/s
c_f	dimensionless wall-shear stress	$c_f = \tau_w / \frac{1}{2} \rho U_\infty^2$	
c_p	specific heat at constant pressure		J/kgK
c_v	specific heat at constant volume		J/kgK
e_b	spectral emissive power of a blackbody		W/m^3
f	dimensionless stream function		
Fo	Fourier number	$Fo = at/h^2$	
h	enthalpy		J/kg
h	solid thickness		m
h	Planck's constant	$h = 6.62 \times 10^{-34}$	J/s
k	thermal conductivity		W/Km
k	Boltzmann's constant	$k = 1.382 \times 10^{-23}$	J/K
L	characteristic length		m
m	pressure gradient parameter	$U_e = Cx^m$	
Ma	Mach number	$Ma = U/c$	
Nu	Nusselt number	$Nu = \alpha L/k$	
Nu_x	local Nusselt number	$Nu_x = \alpha x/k$	
Pr	Prandtl number	$Pr = \nu/a$	
p	static pressure		N/m^2
p_t	total pressure		N/m^2
q_{in}	irradiated energy		W/m^2
q_c	convective heat flux		W/m^2
q_k	conductive heat flux		W/m^2
q_{rad}	radiative heat flux		W/m^2
Re	Reynolds number	$Re = UL/\nu$	
Re_x	local Reynolds number	$Re_x = Ux/\nu$	

CONTENTS

symbols	quantity	unit
S	Seebeck constant	V/K
S	digital value	
t	time	t
T	temperature	K
T_t	total temperature	K
T_w	wall temperature	K
ΔT	reference temperature difference	K
u	velocity component in x -direction	m/s
U	flow velocity	m/s
U	current	V
v	velocity component in y -direction	m/s
x	spatial coordinate along the plate	m
y	spatial coordinate normal to the plate	m
greek		
symbols	quantity	unit
α	heat transfer coefficient	W/K
α_r	absorptivity	
γ	c_p/c_v	
δ	distance between two numerical grid points	m
δ_T	thermal boundary layer thickness	m
δ_u	velocity boundary layer thickness	m
ϵ_r	emissivity	
η	dimensionless coordinate	
Θ	dimensionless temperature	
λ	wavelength	m
μ	dynamic viscosity	kg/ms
ν	kinematic viscosity	m^2/s
ξ	dimensionless coordinate	
ψ	stream function	m^2/s
ρ	density	kg/m^3
ρ_r	reflectivity	
σ	Stefan-Boltzmann's constant	$k = 5.67 \times 10^{-8}$ $W/m^2 K^4$
τ	shear stress	N/m^2
τ_r	transmissivity	
τ_w	wall-shear stress	N/m^2

CONTENTS

subscripts

e	edge (outside the boundary layer)
i	spatial direction
n	normal direction to the surface
r	radiative property
s	solid
t	tangential direction to the surface
0	start condition
∞	free stream condition



Chapter 1

Introduction

In times of increasing environmental awareness and exhausting natural energy resources, reducing energy consumption is essential. Part of the required energy in industrial applications is lost by fluid friction. Minimizing these losses leads to a reduction of costs and environmental burden.

Also in aeronautical applications friction plays an important role. In order to design fuselages and wings of aircraft, that have a minimum friction drag, there is a large need to develop accurate measurement techniques. A new non-intrusive measurement technique to measure wall-shear stresses with the help of an infrared camera is investigated in the present study.

1.1 Role of the wall-shear stress

In fluid mechanics basically two different kinds of forces are acting on solids. These are normal forces and tangential forces. The normal forces are generated by pressure, and tangential forces result out of viscous effects. As the molecules of the fluid adhere at the surface of the solid, a velocity gradient normal to the surface is generated, which produces shear stresses. The magnitude of the shear stress depends on the velocity gradient and on the viscosity of the fluid.

The normal stresses cause the so-called pressure drag and the tangential stresses cause the viscous drag. The sum of these forces in the flow direction determines the total drag of a body. The total drag can be further split up into 2D profile drag (including wave drag due to shock waves) and 3D induced drag.

The shape and surface roughness of a body determine the magnitude of the different drag producing effects. The contribution of the viscous drag to the total drag of the object is large in applications like high speed aircraft (30 – 40%), transport aircraft and tankers (50%), underwater bodies (> 70%) and long distance pipelines (\approx 100%). Previous research on pressure drag minimization decreased the drag coefficient of most air and underwater bodies to very low values, because the measurement of the local pressure on the object is rather

simple. Current attention is paid to viscous drag reduction. This is especially the case in the aircraft industry, where the rapidly expanding transportation market is pushing this development, because even small improvements can have tremendous economic benefits. For example, viscous drag reduction for the complete US domestic airline fleet of about 5 – 10%, would save half a 500 million dollar per year due to the decreased fuel consumption [1].

1.2 Measurement techniques

To evaluate and validate methods to minimize viscous drag, accurate measurement techniques are required. Most of the present measurement techniques are only suitable in wind tunnel tests. The experimental setup of the measurement techniques itself or disturbances and vibrations make in-flight tests very difficult.

Although with the help of weighing systems or wake rakes, the *total* viscous drag can be measured, to optimize the shape of a body to minimize drag, definite knowledge about the *local* shear stress at the body surface is essential. Mechanical techniques like floating elements measure directly the tangential forces on a movable device, mounted into the surface of the object. Since the wall-shear stresses are usually too small to accurately measure them mechanically, also indirect techniques were developed, which use physical phenomena related to the wall-shear stress to determine the skin friction.

In the first place there are measurement methods, which use the dependence of the wall-shear stress on the velocity gradient. These are pressure probes (Stanton and Preston probes) on the one hand and hot-wires on the other hand. Both methods are intrusive, which means that they generate disturbances due to their presence in the flow. Laser-Doppler anemometry is a non-intrusive velocity measurement technique, but because of the large experimental and data processing effort, this technique is difficult to implement in cases such as in industrial wind tunnels and flight tests.

Other non-intrusive measurement techniques are heat transfer (hot-film) methods, which use the Reynolds analogy to derive wall-shear stresses out of the measured local convective heat flux from a heated surface into the flow. Like floating elements, hot-films are mounted into the surface of the object, which minimize their intrusive effect. Since the measurement is fixed to a definite position, hot films are not very practical in measuring complete wall shear-stress distributions.

1.3 Quantitative infrared thermography in wall-shear stress measurements

The fact that wall-shear stresses can be related to the heat transport from the object to the flow, which is determined by temperature measurements, leads to the employment of

the infrared (IR)-thermography. In existing aerodynamical investigations, IR-thermography is mainly applied to the *qualitative* detection of the position of transition and of separation bubbles. Transition is the change from a laminar flow to a turbulent flow. This change leads to a sudden increase in the wall-shear stress and with it to an increase in the wall-heat transfer. Due to the variation of the wall-heat transfer, the position of the transition point can be detected at a rapid change of the surface temperature, measured by an IR-camera. This non-intrusive technique is used as a qualitative measurement technique in large scale experiments like in-flight tests, which are of high industrial interest.

Figure 1.1 sketches an example of the Fokker 100 experimental setup (ELFIN Project), showing how the infrared camera monitors the wing in an in-flight test. The result of a temperature measurement along an airfoil in a wind tunnel, performed in our laboratory, is given in figure 1.2.

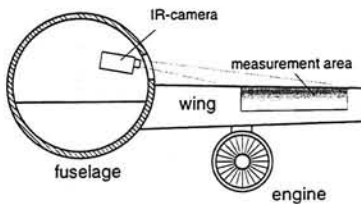


Figure 1.1: In-flight experiment.

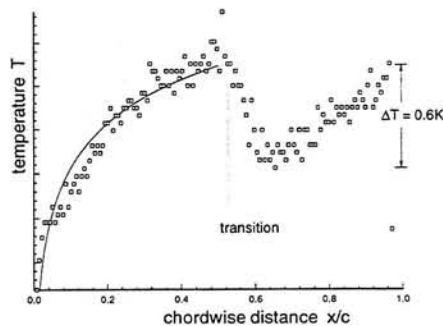


Figure 1.2: $T(x)$ along an airfoil.

The improvement of modern IR-cameras during the last years has led to an increase of its spatial resolution and thermal sensitivity. This makes it interesting to investigate whether *quantitative* IR-thermography can also be employed to the measurement of wall-shear stresses. In the present investigation a non-intrusive wall-shear stress measurement technique is developed. This technique is based on the same theoretical background as the hot-film probes, but the heat generation and the temperature measurement is performed fully externally, instead of internally within the surface. The required temperature difference between the object and the flow, to force the convective heat flux, is delivered by thermal irradiation and the temperature measurements on the surface of the object are performed with the help of quantitative IR-thermography.

Basically two different measurement techniques will be presented. In the steady technique the IR-camera measures the temperature distribution in a laser heated spot on the surface, while the laser continuously heats the surface of the object. The second method operates in the transient regime. The temperature measurement starts immediately after turning off the laser. The decay of the temperature is monitored by the camera in a series of pictures. The steady procedure is advantageous, because of a smaller data post-processing effort, but

it requires detailed information about the distribution of irradiated emissive power across the beam diameter. Generally speaking the non-intrusivity and the flexibility of the measurement point positioning of both infrared measurement techniques and thus the possibility of application to in-flight tests are striking advantages in contrast with other techniques.

It has to be emphasized, that the suitability of the present measurement technique is not restricted to aerospace applications. It can easily be transferred to other fields, in which wall-shear stress effects play a major role, like shipbuilding, aerodynamic car design, forces on buildings due to wind and processes in the chemical industry.

1.4 Aim of the report

This report first presents a summary of the current state of the development of quantitative IR-thermography in wall-shear stress measurements. Emphasis is set on the derivation of the mathematical model and on the detailed description of the experimental components, especially the IR-camera. Secondly also the performance of the IR-camera is investigated in preliminary experiments, which are described in this report. To determine the capabilities of both measurement methods (steady and unsteady), the IR-technique is first applied to a flow along a flat plate under low speed wind-tunnel conditions. The results are compared with the well-known existing values of the wall-shear stress in a Blasius flow.

1.5 Outline of the report

To develop this measurement technique, detailed knowledge about different technical processes is required. Chapter 2 presents the basic equations for the mass, momentum and energy transport in the fluid flow along a solid and the heat transport mechanisms inside the solid. To judge the possibilities of the developed method, some existing wall-shear stress measurement methods are described in chapter 3. The derivation of the equation to calculate the wall-shear stress out of the measured temperature data can be found in chapter 4. Since highly accurate temperature measurements are required, chapter 5 describes each component of the camera and its performance under experimental conditions in detail. The presented measurement technique requires the development of software, which is described in chapter 6. It is divided into two main sections. There is a description of the developed data-processing programs on the one hand and of the numerical calculations inside the flow and the solid on the other hand. These calculations are used to validate the experimental procedure. The results of the experiments and the calculations can be found in chapter 7. The conclusions and the recommendations to further research in chapter 8 close this report.

Chapter 2

Basics of mass, momentum and energy transport

This chapter is intended to introduce the terminology and the basic equations for mass, momentum and energy transport in flows around solid objects.

Fluid motion is determined by the action of the contact forces on surfaces in a flow. These surfaces may either be physical boundaries like the surface of an object, or imaginary interfaces between two adjoining fluid layers.

To derive the describing equations for the velocity components u_i , the pressure p and the temperature T depending on the spatial directions x_i and the time t , a closer look on different fluid motion phenomena is required.

2.1 Phenomena of fluid motion

Normal forces acting on the flow lead to varying static pressures, which cause the acceleration of the fluid. If the influence of friction and gravitational forces can be neglected, like in forced convection flows, the mathematical relation between the change of the static pressure p and the flow velocity U follows out of a momentum balance along a streamline in an inviscid flow

$$dp = -\rho U dU \quad \Rightarrow \quad p + \frac{1}{2} \rho U^2 = p_t. \quad (2.1)$$

The variable ρ denotes the density of the fluid and p_t is the total pressure, which is constant along a streamline and equal to the static pressure in the stagnation point, where $U = 0$. The second part of equation 2.1 is known as the incompressible *Bernoulli* equation.

Next to the acceleration of the flow, normal forces compresses the fluid, which leads to a change of the density ρ .

A common quantity, to describe the compressibility of a fluid, is its speed of sound c . For a perfect gas c can be represented by

$$c = \sqrt{\frac{\gamma p}{\rho}} \quad (2.2)$$

with $\gamma = c_p/c_v = 1.4$ for a perfect diatomic gas.

The coefficients c_p and c_v denote the specific heat for constant pressure p and constant specific volume v respectively. With the help of equation 2.2, the following relation can be derived for adiabatic conditions

$$\frac{1}{\rho} d\rho = \frac{1}{\gamma p} dp = \frac{\rho U}{\gamma p} dU = \frac{1}{2c^2} dU^2. \quad (2.3)$$

To describe the ration between the flow velocity and the speed of sound, the *Mach* number Ma is introduced

$$Ma = \frac{U}{c}. \quad (2.4)$$

From equation 2.3 it can be concluded that for air at normal ambient conditions and a flow speed up to $Ma = 0.3$ the variation of the density ρ can be neglected. This Mach number can be accepted as the upper limit to assume *incompressible* flow conditions.

Although air is a real gas, it behaves like a perfect gas below $Ma = 5$. Thus γ for air is equal to 1.4 (see eqn. 2.2).

As already mentioned in the introduction, there are also tangential forces, caused by viscous effects inside the flow. As a result of viscous molecule interaction inside the fluid, momentum transport is established. The existence of a tangential shearing stress τ is the fundamental difference between a real and a perfect fluid. Perfect fluids do not generate tangential forces and therefore a flow of a perfect fluids is inviscid (frictionless).

The shear stress τ of a real fluid, like air or water, is proportional to the gradient of the tangential velocity component u_t in normal direction x_n

$$\tau = \mu \frac{\partial u_t}{\partial x_n}. \quad (2.5)$$

The fluid constant μ is called the dynamic viscosity.

Applying equation 2.5 to the produced shear stress at a surface of an object, the wall-shear stress τ_w is defined by

$$\tau_w = \mu \left. \frac{\partial u_t}{\partial x_n} \right|_{x_n=0}. \quad (2.6)$$

The dimensionless equivalent for τ_w is the wall-shear stress coefficient c_f

$$c_f = \frac{\tau_w}{\frac{1}{2}\rho U_e^2}. \quad (2.7)$$

The quantity U_e describes the velocity at the outer edge of the boundary layer, as will be explained in the following section.

Although μ is small in case of air, tangential forces can be significant due to large velocity

gradients $\partial u_i / \partial x_n$.

Similar to momentum, thermal energy is also transported inside the fluid under the influence of forces. The relevant mechanisms are convection and thermal diffusion due to thermal conduction. The quantity analogue to the viscosity $\nu = \mu / \rho$, to describe the ability of a fluid to transport energy, is the thermal diffusivity $a = k / \rho c_p$ (k =thermal conductivity). In the molecular gas theory energy and momentum transport are caused by the motion of molecules. The ratio of the two material constants is the *Prandtl* number

$$Pr = \frac{\nu}{a} = \frac{\nu \rho c_p}{k} = \frac{\mu c_p}{k}. \quad (2.8)$$

Pr will be of importance in the next section. The Prandtl number for air is about 0.71 for a wide temperature range.

Under the influence of work due to compression and friction, heat is produced inside the fluid. To study the effect of compression, the flow of a perfect gas is examined first. Based on the conservation of energy, it can be stated that the sum of the kinetic energy and the enthalpy of the fluid $h = c_p T$ is constant in an frictionless flow

$$c_p T + \frac{1}{2} U^2 = c_p T_i. \quad (2.9)$$

Like the total pressure p_t , the term T_i represents the temperature in the stagnation point; it is also referred to as the total temperature.

The effect of frictional heating is of the same order as the heating due to compression, as long as Pr is of the order one. Both can be neglected for low speed applications in the presence of artificial heating.

In that case heat convection and conduction are the relevant processes. Each temperature gradient in any substance along a direction x_i causes a conductive heat flux adverse to the gradient. The relation between temperature gradient and the heat flux per unit area q_k is described by the *Fourier* law

$$q_k = -k \frac{\partial T}{\partial x_i}. \quad (2.10)$$

Conduction effects occur both in solids and in fluids. However in case of fluid flows, the fluid molecules move and carry energy in flow direction. This energy transport influences the temperature gradients in the flow and with it the heat conduction inside the fluid. Heat transfer in a moving fluid close to a solid wall is called *heat convection*.

With the help of the Fourier law 2.10, the convective heat from a surface element to the flow can be determined by

$$q_c = -k \left. \frac{\partial T}{\partial x_n} \right|_{x_n=0}. \quad (2.11)$$

One of the dimensionless heat transfer parameters is the *Nusselt* number, which is defined as

$$Nu = \frac{q_c L}{k \Delta T} = \frac{\alpha L}{k}, \quad (2.12)$$

here α is the heat transfer coefficient, ΔT a characteristic temperature difference between the surface and the flow and L is the characteristic length of the object. The Nusselt number represents the ratio of the actual transported energy and the energy transport in case of pure conduction for the linear temperature gradient $\Delta T/L$.

2.2 Navier-Stokes equation

With the just described relations, the mass, momentum and energy balances can be set up. To simplify the discussion, the following restrictions for the flow are introduced:

- o two dimensional
- o incompressible
- o no heat generation by friction
- o no gravitational forces

Implementing these restrictions, three well-known equations can be derived. For the used Cartesian coordinate system the velocity component u is defined in x direction tangential to the object surface and the velocity component v is defined normal to it.

The equations for the mass, momentum and energy transport are

continuity equation (conservation of mass)

$$\frac{\partial u}{\partial x} + \frac{\partial v}{\partial y} = 0 \quad (2.13)$$

Navier-Stokes equation (conservation of momentum)

$$\frac{\partial u}{\partial t} + u \frac{\partial u}{\partial x} + v \frac{\partial u}{\partial y} = -\frac{1}{\rho} \frac{\partial p}{\partial x} + \nu \left(\frac{\partial^2 u}{\partial x^2} + \frac{\partial^2 u}{\partial y^2} \right) \quad (2.14)$$

$$\frac{\partial v}{\partial t} + u \frac{\partial v}{\partial x} + v \frac{\partial v}{\partial y} = -\frac{1}{\rho} \frac{\partial p}{\partial y} + \nu \left(\frac{\partial^2 v}{\partial x^2} + \frac{\partial^2 v}{\partial y^2} \right) \quad (2.15)$$

energy equation (conservation of energy)

$$\rho c_p \left(\frac{\partial T}{\partial t} + u \frac{\partial T}{\partial x} + v \frac{\partial T}{\partial y} \right) = k \left(\frac{\partial^2 T}{\partial x^2} + \frac{\partial^2 T}{\partial y^2} \right). \quad (2.16)$$

As mentioned before, in general the velocity distribution in the flow interacts with the temperature field. Thus the equations for momentum and energy transport have to be solved simultaneously. But if the influence of temperature effects on the thermodynamic properties like ρ and ν remains small, as in the case for incompressible flow or for moderate forced heating, the velocity field can be assumed to be independent of the temperature distribution.

2.3 Boundary layer equations

The concept of a boundary layer was introduced by Prandtl in 1904. He has proven that a flow around an object can be divided into two regions. On the one hand there are region where viscous effects are dominant, like the region very close to the surface of the object (boundary layer) and behind the object (wake), and on the other hand there is the remaining outer flow, which can assumed to be inviscid. The flow around a body is sketched in figure 2.1. The velocity and the thermal boundary layer are shown in figure 2.2.

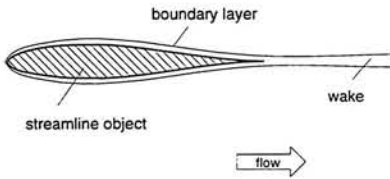


Figure 2.1: Flow around an object.

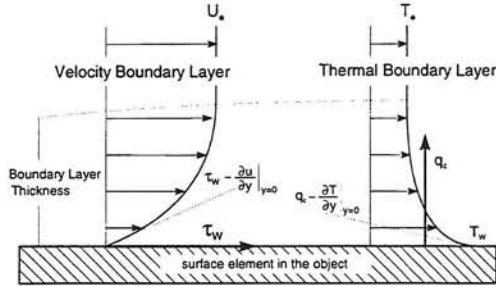


Figure 2.2: Boundary layers.

Due to viscous interaction between the fluid and the surface of an object, the fluid adheres to the surface, which leads to $u = 0$ and $v = 0$ at $y = 0$. This effect is the so called no-slip condition. Thus the tangential velocity increases rapidly from zero at the surface to the velocity of the inviscid outer flow U_e at the edge of the boundary layer. As already mentioned, the temperature distribution is determined by the flow field. Thus the shape of the thermal boundary layer is influenced by the velocity boundary layer, in which the temperature at the surface T_w rapidly changes to T_e at the edge of the thermal boundary layer. Because of the small thickness of the boundary layer and the no-slip condition, the following facts inside the boundary layer can be inferred:

- gradients of the variables u , v , and T in x -direction are much smaller than in y -direction
- the velocity component v is much smaller than the component u
- the pressure p is rather constant across the boundary-layer thickness

These simplifications lead to the boundary equations

$$\frac{\partial u}{\partial x} + \frac{\partial v}{\partial y} = 0 \quad (2.17)$$

$$\frac{\partial u}{\partial t} + u \frac{\partial u}{\partial x} + v \frac{\partial u}{\partial y} = -\frac{1}{\rho} \frac{dp}{dx} + \nu \frac{\partial^2 u}{\partial y^2} \quad (2.18)$$

$$\frac{\partial T}{\partial t} + u \frac{\partial T}{\partial x} + v \frac{\partial T}{\partial y} = a \frac{\partial^2 T}{\partial y^2} \quad (2.19)$$

The momentum equation can be further modified by using the Bernoulli equation at the outer edge

$$\frac{\partial u}{\partial t} + u \frac{\partial u}{\partial x} + v \frac{\partial u}{\partial y} = \frac{\partial U_e}{\partial t} + U_e \frac{\partial U_e}{\partial x} + \nu \frac{\partial^2 u}{\partial y^2}. \quad (2.20)$$

The equation for the momentum in x -direction 2.18 and the energy equation 2.19 show a striking similarity. Under special circumstances, like a flow along a flat plate ($dp/dx = 0$) and a fluid with $Pr = \nu/a = 1$, a complete analogy can be achieved. This analogy was first noticed by Osborne Reynolds and is called the *Reynolds Analogy*.

Since the Prandtl number represents the ratio of the momentum to the energy transport in the fluid, it influences the ratio of the boundary layer thicknesses of the velocity and the thermal boundary layer.

Figure 2.3 compares the thicknesses of the velocity δ_V and the thermal boundary layer δ_T for very large and very small values of the Prandtl number.

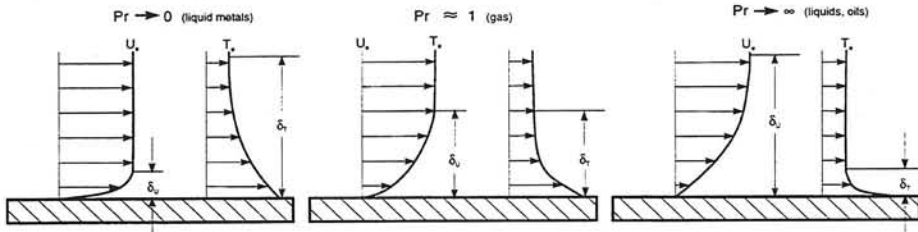


Figure 2.3: Velocity and thermal boundary layer for different Prandtl numbers.

Basically the just described concept of the boundary layer holds for laminar and turbulent flows.

In laminar flows the fluid flows in layers (*lamina*) of different velocities, which interact on a microscopic scale. That means, that slower moving molecules migrate upward to the faster layer and decelerate it and the faster molecules move downward. The magnitude of the transverse velocity can be neglected.

In particular for adverse pressure gradients, a laminar velocity boundary layer can become unstable and turn into a turbulent boundary layer, which leads to a macroscopic turbulent particle transport in addition to the microscopic interaction. Through these fluctuations fast moving particles from higher regions of the boundary layer move closer to the wall and generate high velocities there. This increase of the velocity gradient $\partial u/\partial y$ at the wall produces large wall-shear stresses (see eqn. 2.5) and with it an increase of the convective heat transfer. To represent turbulent flow mathematically, the instantaneous velocity u is assumed to consist of an arbitrary unsteady fluctuating velocity u' , that is superimposed on a time averaged velocity \bar{u} . The term $u = \bar{u} + u'$, and similarly the other velocity

components, can be inserted in the Navier-Stokes equation and in the energy equation. When the representing equations are averaged in time the so-called Reynolds averaged Navier-Stokes equations (RANS) result. Due to the additional terms these equations are more difficult to solve for the turbulent case in contrast to the laminar case.

To illustrate and to simplify the determination of solutions of the boundary layer equations, the following discussion is restricted to steady laminar flows.

2.4 Characteristic numbers

Normalizing the variables in the equations with characteristic scales leads to new parameters. Commonly the variables are transformed to

$$x_i^* = \frac{x_i}{L} \quad u_i^* = \frac{u_i}{U_\infty} \quad p^* = \frac{p}{\rho U_\infty^2} \quad T^* = \frac{T - T_w}{T_\infty - T_w},$$

where the velocity U_∞ denotes the velocity of the undisturbed outer flow and T_w the wall temperature. Introducing the dimensionless magnitudes into the Navier-Stokes and the energy equation, leads to the following formulations

$$u^* \frac{\partial u^*}{\partial x^*} + v^* \frac{\partial u^*}{\partial y^*} = \frac{1}{Re} \left(\frac{\partial^2 u^*}{\partial x^{*2}} + \frac{\partial^2 u^*}{\partial y^{*2}} \right) - \frac{\partial p^*}{\partial x^*} \quad (2.21)$$

$$u^* \frac{\partial v^*}{\partial x^*} + v^* \frac{\partial v^*}{\partial y^*} = \frac{1}{Re} \left(\frac{\partial^2 v^*}{\partial x^{*2}} + \frac{\partial^2 v^*}{\partial y^{*2}} \right) - \frac{\partial p^*}{\partial y^*} \quad (2.22)$$

$$u^* \frac{\partial T^*}{\partial x^*} + v^* \frac{\partial T^*}{\partial y^*} = \frac{1}{RePr} \left(\frac{\partial^2 T^*}{\partial x^{*2}} + \frac{\partial^2 T^*}{\partial y^{*2}} \right). \quad (2.23)$$

The parameter Re is known as the *Reynolds* number, which is defined as

$$Re = \frac{LU_\infty}{\nu}. \quad (2.24)$$

The Reynolds number represents the ratio between inertia and frictional forces. As can be concluded from the dimensionless equations, two different flows are similar as long as the parameters Re and Pr are equal in both cases. The concept of characteristic numbers is not restricted to the mentioned simplified flow conditions. In most cases there are other dimensionless parameters, describing the investigated phenomena, like the Mach number for compressible flows and the Grashof number for natural convection flows.

2.5 Similarity equations

To solve the boundary layer equations 2.18 and 2.19, the principle of similarity can be applied. Physically this means that for certain flow conditions the velocity profile $u(y)$, respectively

the temperature $T(y)$, differ only in a scale factor for arbitrary coordinates x . Mathematically the coordinates x and y can be replaced by new coordinates, which leads to a simplification from partial differential equations to ordinary differential equations for the velocity and the thermal boundary layer. These new coordinates are defined as

$$\xi = \frac{x}{L} \quad \eta = \frac{y}{x} \sqrt{\frac{U_e x}{\nu}}$$

The dimensionless forms of the velocity f' and the temperature Θ are

$$f'(\eta) = \frac{u}{U_e} \quad \Theta(\eta) = \frac{T - T_w}{T_e - T_w},$$

where $f(\eta)$ is equal to the stream function $\psi(x, y)$ in the coordinate system ξ, η .

The definition of the stream function is

$$u = \left(\frac{\partial \psi}{\partial y} \right)_x \quad v = - \left(\frac{\partial \psi}{\partial x} \right)_y$$

Since the stream function ψ satisfies automatically the continuity equation 2.13, the number of equations is reduced by one. Inserting the transformed variables and the stream function into the boundary layer equations, the similarity of the boundary layers can be achieved for flows with an edge velocity $U_e = U(x/L)^m$, where U and L are arbitrary velocity and length scale. The velocity distribution of such a flow corresponds to a potential flow around a wedge with an included angle of $\pi\beta = \pi 2m/(m+1)$. Boundary layers of this kind are called Hartree boundary layers or wedge flows.

Some Hartree flows are sketched in figure 2.4.

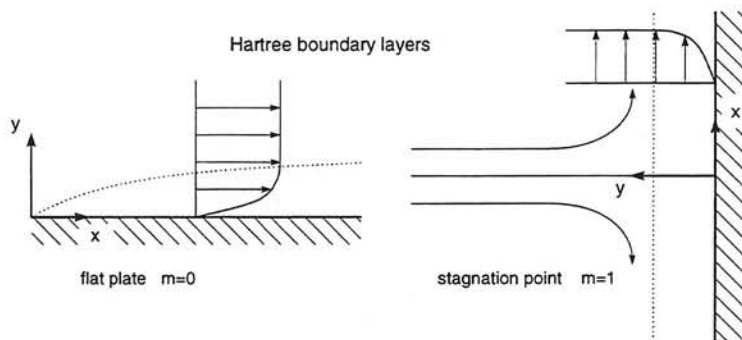


Figure 2.4: Similar laminar boundary layers.

The similarity equations for the velocity boundary layer, which is known as the Falkner-Skan equation, and the thermal boundary layer are derived from

$$f''' + \frac{m+1}{2} f f'' + m(1-f'^2) = 0 \quad (2.25)$$

$$\Theta'' + \frac{m+1}{2} Pr f \Theta' = 0 \quad (2.26)$$

with the boundary conditions

$$\begin{aligned} \eta = 0 &\Rightarrow u = 0 \quad v = 0 \quad T = T_w = \text{const.} &\Rightarrow f = 0 \quad f' = 0 \quad \Theta = 0 \\ \eta \rightarrow \infty &\Rightarrow u \rightarrow U_e \quad T \rightarrow T_e &\Rightarrow f' \rightarrow 1 \quad \Theta \rightarrow 1. \end{aligned}$$

An important example for similar solutions is the boundary layer along a flat plate. The problem was first formulated by Prandtl in 1904. Blasius described the details in 1908. Thus a flow along a flat plate is often called a *Blasius flow*. In a Blasius flow the edge velocity U_e is constant and thus $m = 0$.

Solving the Falkner-Skan equation 2.25 for zero pressure gradients (i.e. $m = 0$), an equation for the local wall-shear stress coefficient $c_f = \tau_w / \frac{1}{2} \rho U^2$ can be obtained

$$c_f = 0.664 Re_x^{-1/2}. \quad (2.27)$$

From equation 2.26 a relation between Nu_x , Re_x and Pr can be derived for $Pr \ll 1$ and $Pr \gg 1$, while Re_x and Nu_x are defined as

$$Nu_x = \frac{\alpha x}{k} \quad Re_x = \frac{U_\infty x}{\nu}. \quad (2.28)$$

The expressions for the two borderline cases can be found in figure 2.5.

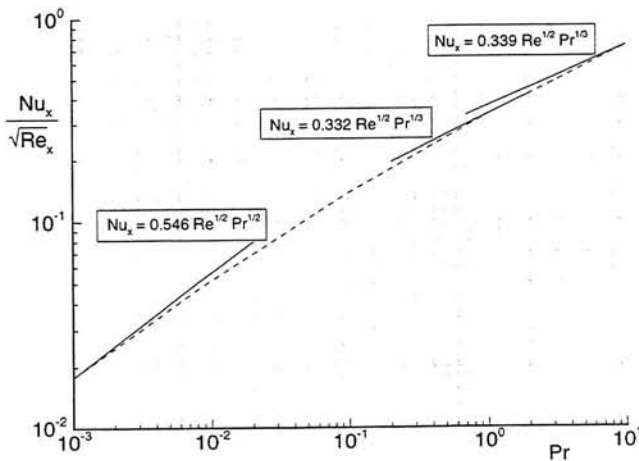


Figure 2.5: Relation between Nu_x , Re and Pr

The dashed line in figure 2.5 represents the numerical solution of the Falkner-Skan equation 2.26 with $m = 0$. It can also be observed in figure 2.5 that when the Prandtl number is near unity, Nu_x can be approximated by

$$Nu_x = 0.332 Re_x^{1/2} Pr^{1/3}. \quad (2.29)$$

With the help of equation 2.27 and 2.29 a relation between Nu_x and Re_x for $Pr \approx 1$ can be formulated:

$$Nu_x = \frac{1}{2} c_f Re_x Pr^{1/3} \quad (2.30)$$

For $Pr = 1$ equation 2.30 represents the simplest mathematical formulation of the Reynolds analogy for the flow along a flat plate.

At this point the short review of basic equations for mass, momentum and heat transfer is closed. The presented theory should be sufficient to understand the necessary theoretical background applied to the developed measurement technique.

Further details can be found in standard text books [2].

Chapter 3

Wall-shear stress measurement techniques

As mentioned in the introduction of this report, different types of wall-shear stress measurement techniques exist. These techniques may either measure the wall-shear stress directly, or indirectly via velocity or heat transfer measurements.

The most frequently encountered mechanical, tracer and thermal methods are presented in this chapter.

3.1 Mechanical methods

Since wall-shear stresses are tangential forces on surfaces, it would be obvious to measure these forces by a direct force measurement technique. One of these techniques is the *floating element*. The experimental setup of a floating element is sketched in figure 3.1.

A floating element consists of a flat element inserted into the surface. The horizontal position of the element is adjusted by springs. Under the influence of the wall-shear stress, the floating element moves in the direction of the flow until a force equilibrium between the tangential shear forces and the spring forces is reached. The displacement of the element can be measured by capacitive, piezoelectric or magnetic means.

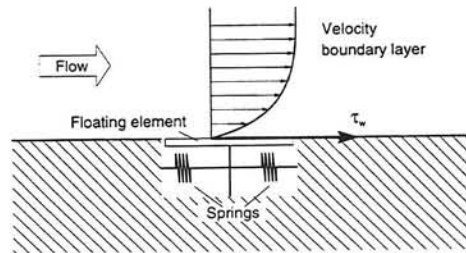


Figure 3.1: Floating element.

Concerning wall-shear stress measurements the floating element has got the following advantages and disadvantages:

Advantages

- o direct force measurement \Rightarrow small data post-processing effort
- o measurement of two velocity components
- o detection of back-flow areas

Disadvantages

- o fixed measurement position
- o limited spatial resolution
- o limited time response
- o complex manufacturing
- o fragile

Due to the fact that the force, generated by a the wall-shear stress, depends on the size of the floating element, the minimum size of the element is limited by the minimum detectable force. Because of this and the other disadvantages mentioned above, other indirect measurement techniques have been developed. These techniques use the unique relation between the wall-shear stress and other phenomena.

As described in chapter 2 wall-shear stresses are determined by the gradient of the tangential velocity component at the surface of an object. Thus velocity measurement techniques are introduced in wall-shear stress investigations.

A simple velocity measurement technique is the pressure probe. Such a pressure probe consists of a tube with an opening facing the flow, where the total pressure is measured, and one or more holes in the side of the probe for the static pressure. The pressure difference between the total and the static pressure is measured by a manometer. This difference is related to the local flow speed by $\Delta p = \rho U^2/2$.

To measure the velocity as close to the wall as possible, two special pressure probes are commonly used. These are the *Preston tube* and the *Stanton tube*.

The Preston tube is a simple tiny circular tube positioned at the surface, which can be traversed along the object. In the case of a Stanton tube the surface of the object itself forms one side of the tube. The other side is usually made of a razor blade covering a static pressure hole inside the object. Both tubes measure the total pressure. The required static pressure is measured at a pressure hole next to the tube.

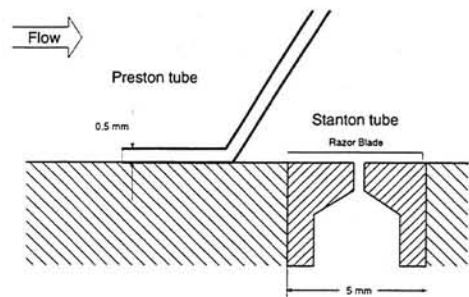


Figure 3.2: Preston and Stanton tube.

The presence of the probes in the flow leads to disturbances, which are even more critical inside the boundary layer, having a thickness of a few millimetres. Within the manufacturing restrictions the probes are constructed as small as possible.

Advantages

- o small experimental effort
- o cheap

Disadvantages

- o measurement of only one velocity component
- o no detection of back-flow
- o fixed measurement position (Stanton tube)
- o requires calibration
- o limited spatial resolution
- o limited time response
- o intrusive
- o susceptibility to pollutants in the flow

3.2 Tracer methods

In contrast to the just presented methods, tracer methods do not measure the velocity of the flow itself, but instead they monitor agents moving with the flow. These agents may be particles, heat waves or ultrasonic waves, which can be detected optically, thermally or acoustically, respectively. One of the optical tracer methods is the *Laser-Doppler Anemometry (LDA)*. It is a common technique in modern flowfield research. The basics of the LDA are illustrated in figure 3.3.

In the LDA two crossing laser beams are forming a measurement volume. Due to the monochromatic and coherent light of a laser, an interference pattern of dark and bright fringes is generated. Particles, which are injected in the flow, radiate light flashes passing the interference pattern. An optical device measures the frequency of the flashes. With the help of the geometry of the interference pattern the velocity component perpendicular to the fringes can be determined.

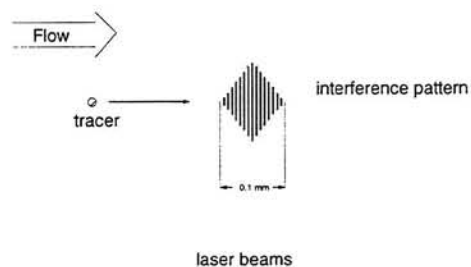


Figure 3.3: Laser-Doppler-Anemometry.

Since one pair of laser beams measures just one velocity component, one respectively two laser beam pairs under different angles to each other have to be included, to extend this technique to two and three dimensional measurements.

Advantages

- o non-intrusive
- o measurement of up to 3 velocity component
- o detection of back-flow
- o high spatial resolution
- o high time response

Disadvantages

- o high experimental effort
- o high data-processing effort
- o expensive

3.3 Thermal methods

One of the most used thermal methods to measure flow velocities is the *hot-wire* technique. Due to its high time response, this technique is mainly used in investigations of highly unsteady flow conditions like turbulent flows.

A tiny electrical heated wire is stretched between a prong. The specific electrical resistance of the wire is related to its temperature. Depending on the velocity of the flow around the wire, heat is transported to the flow, which cools down the wire. There are two different methods. In the constant current method, the current feeding the wire is kept constant and the temperature decrease is measured through the decrease of the electrical resistance. In the constant temperature method, the temperature is kept constant and the required current related to the flow velocity is measured.

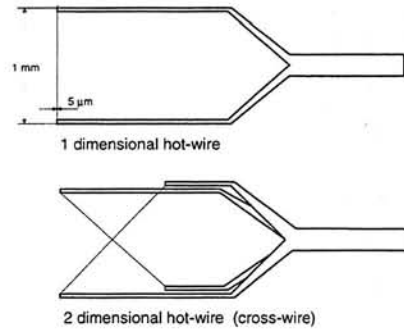


Figure 3.4: 1D and 2D hot-wire.

Similar to the LDA, the hot-wire technique can be extended to two dimensional measurements with the help of a second wire at a different angle to the flow. The relation between the temperature difference and the velocity around the wire or the relation between the current and the velocity, respectively, is determined by calibration.

Advantages

- o high time response
- o two-dimensional measurement
- o easy to manufacture

Disadvantages

- o intrusive
- o requires calibration
- o fragile

The last measurement techniques presented in this chapter is the *hot-film* technique. This method is based on the Reynolds analogy, in which the wall-shear stress is determined from the measured convective heat fluxes. Figure 3.6 shows the components of a hot-film sensor.

Embedded on an insulation to minimize heat conduction, the internal heating leads to a convective heat transfer from the sensor to the flow. The amount of transferred heat for a temperature difference $\Delta T = T_w - T_e$ depends on the wall-shear stress along the sensor. If the sensor is perfectly insulated from the object, the convection is equivalent to the electrical power P of the heater. A common calibration relation for surface mounted hot-films is:

$$P/\Delta T = b_1 + b_2 \tau_w^{1/3}$$

Since hot-film sensors are structurally simple, miniature hot-films are commercially available to increase its spatial resolution.

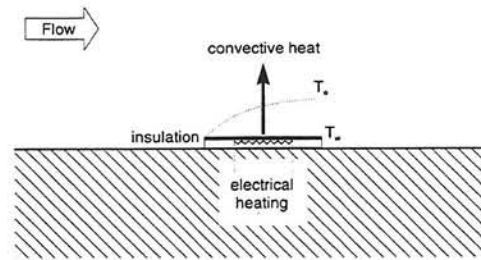


Figure 3.5: Hot-film sensor.

Advantages

- o non-intrusive
- o simple and cheap

Disadvantages

- o fixed measurement position
- o requires calibration
- o no detection of back-flow

Due to the advantages of hot-film sensors concerning wall-shear investigations, this measurement technique has been further improved. To these improved sensors belong the *integrated silicon flow sensors* [3]. In general thermal methods are very attractive for the development of silicon flow sensors, because of their electronic simplicity. The silicon flow sensor uses the same background as the hot-film probes, but the components of the silicon sensor are slightly modified.

The setup of this sensor and the temperature distribution with or without a flow is illustrated in figure 3.6.

The internal heating of the sensor generates a constant heat flux, which produces a symmetric temperature distribution on the sensor under no flow conditions. In this case the temperature difference $\Delta T_{12} = T_1 - T_2$ is zero. Under the influence of a flow the temperature distribution becomes asymmetric, due to the increasing thermal boundary layer thickness in downstream direction. The thicker the thermal boundary layer, the less heat is transferred to the flow and the wall temperature becomes higher. This phenomenon leads to $\Delta T_{12} \neq 0$.

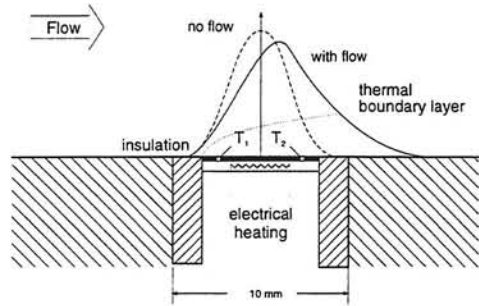


Figure 3.6: Silicon flow sensor.

To obtain a relation between ΔT_{12} and c_f , without a calibration procedure, the thermal boundary layer equation has to be used. This equation can be simplified for local heating conditions like the silicon flow sensor and solved analytically and numerically.

Adding two further temperature measurement points perpendicular to T_1 and T_2 , wall-shear stresses can be measured in two directions. With the help of this technique two disadvantages of the hot-film sensor could be eliminated.

Advantages

- o non-intrusive
- o two-dimensional measurement
- o detection of back-flow
- o simple and cheap

Disadvantages

- o fixed measurement position

Motivated by the advantages of the integrated silicon flow sensor, the presently developed infrared measurement technique is related to this thermal method. The disadvantage, that the measurement is fixed to a certain position on the surface of the object, is overcome by performing both the heating and the temperature measurement externally.

The theoretical background of this technique can be found in the next chapter.

Chapter 4

Theory of heat transfer mechanisms

This chapter deals with theoretical analysis of the heat transfer mechanism in the presented infrared measurement technique. Since the theory of this technique is based on the theory of the silicon flow sensor [3], the following discussion will be comparable in many aspects.

The theoretical description of the heat transfer mechanism in the fluid and inside a solid represents the main part of this chapter. Because of the importance for IR-thermography, a section about thermal radiation is included.

4.1 Heat transfer in fluids

Since the heat transfer from the surface of solid object to the flow is determined by the thermal boundary layer, the theory of this technique is derived from the thermal boundary layer equation.

For the thermal boundary layer equation the following assumptions can be introduced:

- o two dimensional
- o laminar
- o incompressible
- o no heat generation by friction

Although the velocity boundary layer is steady, the thermal boundary layer is not constant in the unsteady measurement technique (after turning off the laser). But since the heat capacity of the air layer is much smaller than the heat capacity of the solid, the unsteady term in the thermal boundary layer equation can be neglected. Therefore the mathematical model is based on the steady thermal boundary layer equation

$$u \frac{\partial T}{\partial x} + v \frac{\partial T}{\partial y} = a \frac{\partial^2 T}{\partial y^2}. \quad (4.1)$$

To fulfill the assumption of a two dimensional heat transfer problem and local heating in x -direction, a laser sheet in x -direction is required.

This laser sheet illustrated in the figure 4.1.

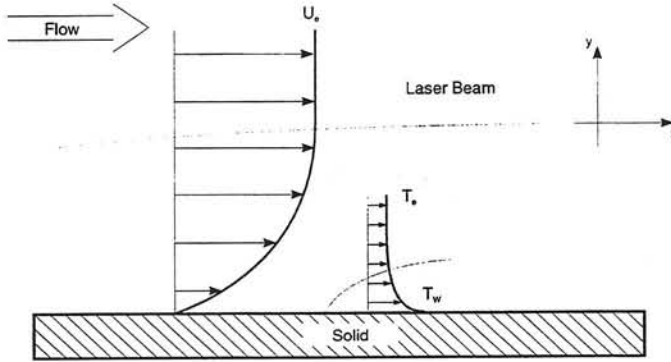


Figure 4.1: Velocity and thermal boundary layer for local heating.

If the hot spot is sufficiently small in x -direction, it can be assumed that:

- o the streamwise flow conditions are constant over the hot spot
- o the thickness of thermal boundary layer δ_T is much smaller than the velocity boundary layer δ_U
- o inside the thermal boundary layer the velocity component u varies linearly with y

Further, using the continuity equation 2.13, the following simplifications for the boundary layer equation in the hot spot can be made.

$ \begin{aligned} & - \partial u / \partial x \rightarrow 0 \quad \Rightarrow \quad \partial v / \partial y \rightarrow 0 \quad \Rightarrow \quad v(y) \rightarrow 0 \\ & - \delta_T \ll \delta_U \\ & - \quad y < \delta_T \quad \Rightarrow \quad u(y) = y \tau_w / \mu \end{aligned} $

Thus the thermal boundary layer equation 4.1 in the hot spot can be simplified to

$$\frac{\tau_w}{\mu} y \frac{\partial T}{\partial x} = a \frac{\partial^2 T}{\partial y^2}. \quad (4.2)$$

Although the temperature distribution in the hot spot is not constant, equation 4.2 is first solved for constant wall temperature by means of a similarity procedure.

Thus normalized variables have to be introduced.

$$\xi = \frac{x}{L} \quad \eta = y \left(\frac{\tau_w}{\mu a x} \right)^{1/3} \quad \Theta = \frac{T - T_\infty}{\Delta T} \quad \Delta T = T_w - T_\infty \quad (4.3)$$

This coordinate transformation leads to an ordinary differential equation (prime denotes differentiation with respect to η)

$$\Theta'' + \frac{1}{3}\eta^2\Theta' = 0 \quad (4.4)$$

with the boundary conditions

$$\Theta(0) = 1 \quad \Theta(\infty) = 0. \quad (4.5)$$

Equation 4.4 can be solved analytically, yielding

$$\Theta(\eta) = 1 - C \int_0^\eta \exp\left(-\frac{1}{9}\zeta^3\right) d\zeta. \quad (4.6)$$

The integration constant C is defined as

$$C = \left[\int_0^\infty \exp\left(-\frac{1}{9}\zeta^3\right) d\zeta \right]^{-1} = \frac{1}{9^{1/3}\Gamma(\frac{4}{3})} = 0.5384, \quad (4.7)$$

where Γ indicates the Gamma function.

To derive the required relation between the heat transport from the surface of the object to the flow and the wall-shear stress, the expression for this heat flux must also be transformed:

$$q_c = -k \left. \frac{\partial T}{\partial y} \right|_{y=0} = -k\Delta T \left. \frac{\partial \Theta}{\partial y} \right|_{y=0} = -k\Delta T \left. \frac{\partial \Theta}{\partial \eta} \frac{\partial \eta}{\partial y} \right|_{\eta=0} = -k\Delta T \Theta'(0) \left(\frac{\tau_w}{\mu a x} \right)^{1/3}. \quad (4.8)$$

Since the term $\Theta'(0)$ is equal to $-C$ the final relation for constant wall temperature T_w in non-dimensional form is:

$$\frac{q_c L}{k\Delta T} = C \left(\frac{\tau_w L^2}{\mu a} \right)^{1/3} \xi^{-1/3}. \quad (4.9)$$

From equation 4.9 the averaged Nusselt number for the hot spot can be derived

$$Nu = \int_0^1 \frac{q_c L}{k\Delta T} d\xi = \frac{3}{2} C \left(\frac{\tau_w L^2}{\mu a} \right)^{1/3}. \quad (4.10)$$

4.1.1 Arbitrary wall temperature

Due to a non-constant distribution of the irradiated energy of the laser and heat conduction inside the solid, a certain non-constant temperature distribution in the hot spot is generated. Since the thermal boundary layer equation 4.1 is a linear differential equation in T , its solution can be replaced by a superposition of stepwise variations.

Thus the continuous temperature distribution is approximated by surface temperature steps $d\Theta_{step}$ at discrete positions ξ_0 . This approximation is sketched in figure 4.2.

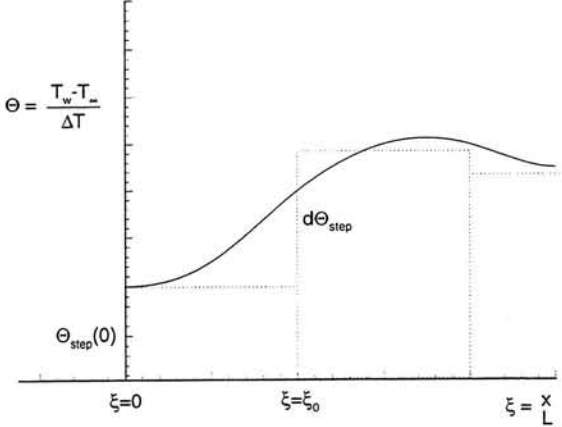


Figure 4.2: Step approximation for arbitrary wall temperatures

Replacing the equation

$$\frac{q_c L}{k \Delta T} = \frac{2}{3} Nu \xi^{-1/3} \quad (4.11)$$

for a single step of constant temperature by a series of steps, a relation between the heat flux q_c and the wall-shear stress τ_w for arbitrary wall temperatures can be derived

$$\frac{q_c L}{k \Delta T} = C \left(\frac{\tau_w L^2}{\mu a} \right)^{1/3} \left[\Theta_{step}(0) \xi^{-1/3} + \int_0^\xi (\xi - \xi_0)^{-1/3} \frac{d\Theta_{step}}{d\xi_0} d\xi_0 \right], \quad (4.12)$$

where Θ_{step} is defined as

$$\Theta_{step} = \frac{T_w - T_\infty}{\Delta T} \quad \Delta T = \text{temperature reference scale.} \quad (4.13)$$

With the help of equation 4.12 the wall-shear stress can be calculated from the given heat transfer to the flow q_c .

4.2 Heat transfer in solids

To measure the convective heat transfer q_c from a solid to the flow, it is necessary to determine the temperature distribution inside the solid.

All properties belonging to the solid are written with the subscript "s".

In a solid, energy is transported by heat conduction. The mathematical model to describe this heat transport is the *Poisson* equation. It can be derived out of a simple unsteady 2D energy balance over an infinitesimal small control volume in the solid

$$\rho_s c_s \frac{\partial T}{\partial t} = k_s \left(\frac{\partial^2 T}{\partial x^2} + \frac{\partial^2 T}{\partial y^2} \right). \quad (4.14)$$

Analytical solutions of the differential equation 4.14 exist only for a limited number of realistic boundary conditions.

To simplify the equation, the following derivations are restricted to one-dimensional cases. These solutions can be applied to simple experimental conditions and can be used to check the accuracy of numerical calculations.

Consider a flow along a flat plate with irradiated energy q_{in} on the upper side and a perfect isolation on the lower side:

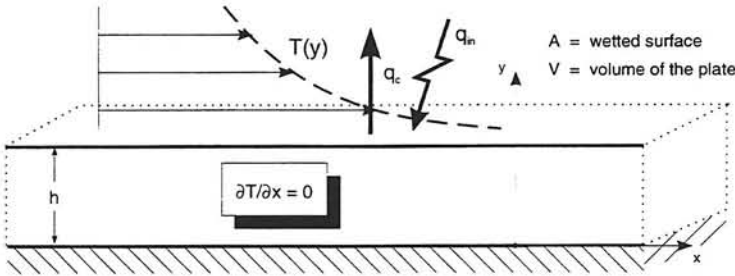


Figure 4.3: Boundary conditions for a flat plate.

This implies the following boundary conditions:

$$\begin{array}{ll} y = 0 & k_s \frac{\partial T}{\partial y} = 0 \\ y = h & k_s \frac{\partial T}{\partial y} = q_{in} - q_c \end{array}$$

Since it is possible to perform the presented measurement technique in the steady or unsteady mode, solutions for both modes are derived in the following subsections.

4.2.1 Steady approach

To achieve a steady convective heat flux q_c , a certain amount of energy q_{in} has to be added to the plate. Under steady conditions the left hand side of the Poisson-equation $\rho_s c_s \partial T / \partial t$

is zero, which simplifies the equation to

$$0 = k_s \left(\frac{\partial^2 T}{\partial y^2} \right). \quad (4.15)$$

Solving equation 4.15 leads to

$$T = \text{const.} \quad \text{and} \quad q_c = q_{in}. \quad (4.16)$$

In case of external heating with a laser, the determination of the term q_{in} is more complicated.

To evaluate the local wall heat transfer without knowing the energy of a heat source, temperatures have to be measured in the unsteady regime.

4.2.2 Unsteady approach

In the unsteady case, the irradiated heat q_{in} is turned off at $t = 0$. Thus the unsteady Poisson equation has to be solved to calculate the change of the temperature distribution inside the solid in time

$$\rho_s c_s \frac{\partial T}{\partial t} = k_s \left(\frac{\partial^2 T}{\partial y^2} \right). \quad (4.17)$$

The temperature distribution in a solid is mainly influenced by the ratio of the two heat transport mechanisms, convection in the fluid and conduction in the solid. A useful quantity to represent this ratio is the *Biot Number*. Since the temperature distribution is not steady, also a dimensionless time has to be introduced, the *Fourier Number*.

With the plate thickness h as the characteristic length these dimensionless numbers are defined as

$$Bi = \frac{\alpha h}{k_s}, \quad Fo = \frac{k_s t}{\rho_s c_s h^2} = \frac{at}{h^2}, \quad (4.18)$$

where the quantity α denotes the heat-transfer coefficient from the solid to the fluid, which is defined as

$$\alpha = \frac{k}{T_w - T_\infty} \left(\frac{\partial T}{\partial y} \right)_{y=h}^{fluid}. \quad (4.19)$$

The temperatures inside the plate can be calculated analytically for very large or very small Biot numbers

$$\begin{aligned} \circ \quad Bi \ll 1 & \quad \Rightarrow \quad 0 < y < h \quad : \quad \frac{\partial T(t)}{\partial y} = 0 \\ & \quad \frac{T - T_\infty}{T_0 - T_\infty} = \exp\left(-\frac{\alpha t}{\rho_s c_s h}\right) \end{aligned} \quad (4.20)$$

$$\begin{aligned} \circ \quad Bi \gg 1 & \Rightarrow y = 0 & : \quad \frac{\partial T(t)}{\partial y} = 0 \\ & & y = h & : \quad T = T_\infty \end{aligned}$$

$$\frac{T - T_\infty}{T_0 - T_\infty} = \frac{2}{\pi} \sum_{n=1}^{\infty} (-1)^{\frac{n-1}{2}} \frac{1}{n} \cos\left(\frac{n\pi y}{2h}\right) \exp\left[-\left(\frac{n\pi}{2}\right)^2 Fo\right]. \quad (4.21)$$

An asymptotic relation for equation 4.21 can be found under the following assumptions

$$\circ \quad \frac{h-y}{2\sqrt{a_s t}} \gg 1 \quad (\text{short times})$$

$$\frac{T - T_\infty}{T_0 - T_\infty} = \frac{1}{\sqrt{\pi}} \int_0^{\frac{h-y}{2\sqrt{a_s t}}} \exp[-z^2] dz \quad (4.22)$$

$$\circ \quad Fo \gg 1 \quad (\text{long times})$$

$$\frac{T - T_\infty}{T_0 - T_\infty} = \frac{2}{\pi} \exp[-\pi^2 Fo] \cos\left(\frac{\pi y}{2h}\right). \quad (4.23)$$

Figure 4.4 shows the temperature distributions in time for the just described combinations for the Biot and the Fourier number.

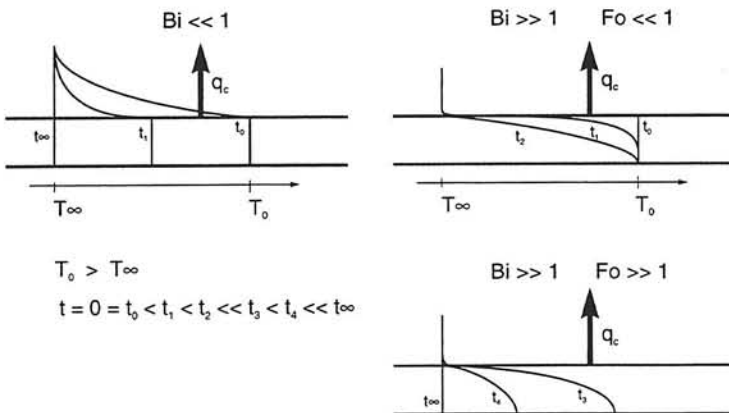


Figure 4.4: Unsteady temperature distribution within a flat plate.

Since solutions are difficult to find for realistic experimental conditions even for one-dimensional cases, the temperature distribution in a solid for arbitrary values of Bi and Fo and especially two- or three-dimensional heat transfer problems have to be determined by numerical

calculations (see chapter 6). However, for many applications, in which the conductivity of the solid material is of the same order as the conductivity of aluminium, the Biot number is much smaller than one. Thus the analytical solution 4.20 of the presented theory can be used.

Based on this equation, a method to measure the irradiated energy of a laser is developed. Further details can be found in section 5.6.

As can be extracted from the presented equations, the size and the thermal properties of the solid have strong impact on the temperature distribution. To achieve an accurate temperature with the help of an IR-camera, the expected temperature range has to be adapted to the performance of the camera by choosing proper materials. Experiments and numerical calculations will be made to obtain the optimum material.

The results can be found in chapter 7.

4.3 Thermal radiation

Besides convection and conduction, thermal radiation is another mechanism to transport heat. The energy is transported via electromagnetic waves and no physical medium is needed for this kind of heat transfer. For example solar energy is transferred to the earth through the vacuum of space.

This section delivers the necessary theory for IR-thermography and for the determination of the radiative heat fluxes from the solid to the surroundings.

All radiative properties are written with the subscript "r".

Concerning radiation, each substance has three different properties:

- o absorptivity α_r
- o reflectivity ρ_r
- o transmissivity τ_r

These properties are illustrated in figure 4.5.

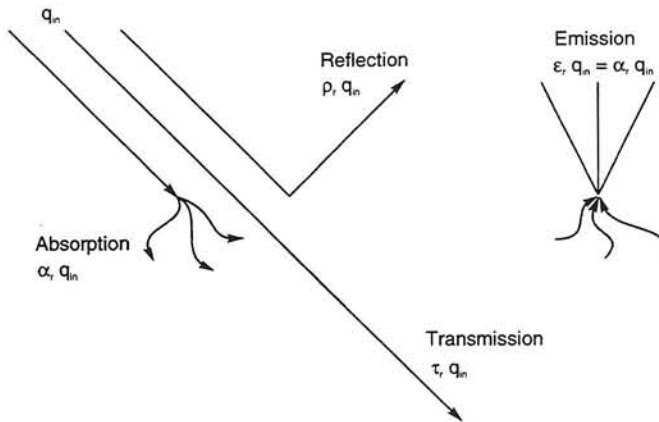


Figure 4.5: Radiative properties of a substance.

Two important mathematical relationships can be extracted from figure 4.5.

- o $\alpha_r + \rho_r + \tau_r = 1$
- o $\alpha_r = \epsilon_r$

For a substance in a vacuum the equilibrium of absorption and emission follows directly out of the energy conservation law. This equilibrium is known as *Kirchhoff's law*.

Two values for the radiative properties encountered in practice are:

- o opaque matter $\tau_r = 0$
- o blackbody $\epsilon_r = 1$

Although a blackbody does not exist in nature, it is used as a reference object. The properties of a blackbody can be derived from quantum mechanics. The basic equations were derived by Planck, Wien, Stefan and Boltzmann [4].

A blackbody is defined as a perfect absorber and thus also as a perfect emitter. Since it radiates energy diffusively, the spectral emissive power is constant over the hemisphere and thus only depends on the blackbody temperature T and the wavelength λ .

$$e_b(\lambda, T) = \frac{2\pi C_1}{\lambda^5 (e^{\frac{C_2}{\lambda T}} - 1)} \quad C_1 = hc_0^2 \quad C_2 = \frac{hc_0}{k} \quad (4.24)$$

Speed of light in vacuum	$c_0 = 2.99 \times 10^8 \frac{m}{s}$
Planck's constant	$h = 6.62 \times 10^{-34} \frac{J}{s}$
Boltzmann's constant	$k = 1.382 \times 10^{-23} \frac{J}{K}$

This formula is *Planck's radiation law*.

For a better impression, the solutions of this equation are plotted in figure 4.6.

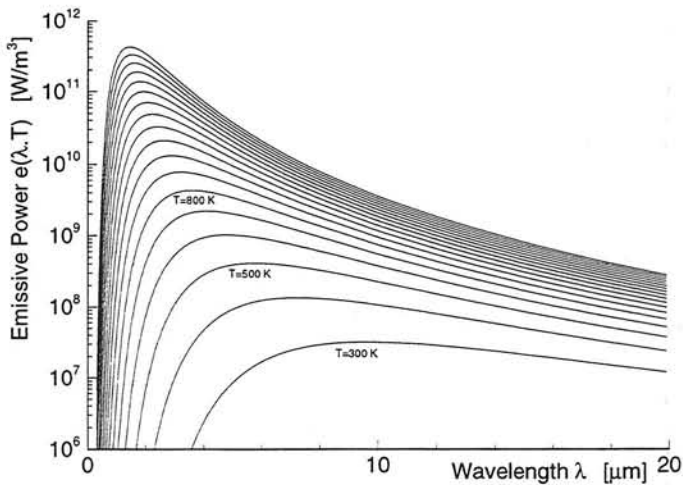


Figure 4.6: Hemispherical emissive power of a blackbody.

Deriving equation 4.24 with respect to the wavelength λ leads to *Wien's displacement law*. It describes at which wavelength an object of a certain temperature emits maximum energy:

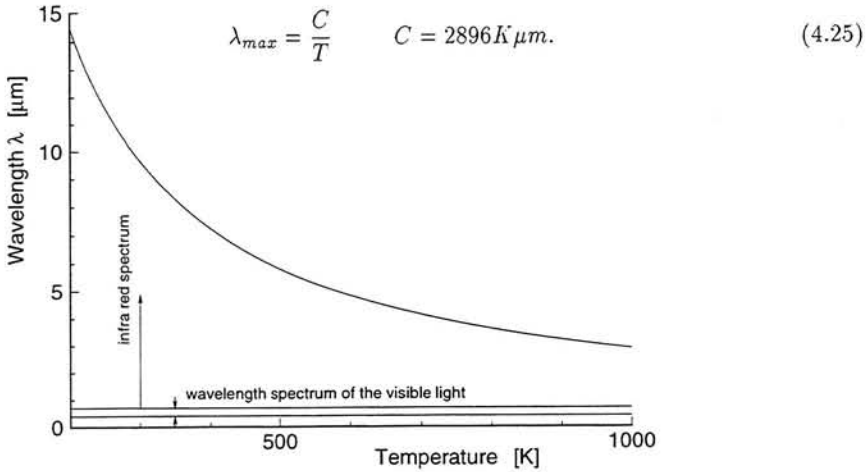


Figure 4.7: Wavelength for maximum emissive power versus temperature.

Applying these two elementary formulations on IR-thermography, some important facts can be derived:

- o objects at ambient temperature radiate mainly in the IR-spectrum
- o the wavelength of maximum emissive power decreases with increasing temperature
- o thermal radiation from objects at temperatures higher than 800 K can be seen by the human eye

In many cases the total hemispherical emissive power, without any restriction to a certain wavelength range, is of interest. Integrating Planck's law over the wavelength from zero to infinity leads to the *Stefan-Boltzmann law*

$$q_{rad} = \sigma T^4 \quad (4.26)$$

Stefan-Boltzmann constant $\sigma = 5.67 \cdot 10^{-8} \frac{W}{m^2 K^4}$.

An object is not only radiating itself, it is also receives a certain amount of energy from surrounding objects. The net heat transport depends on the equilibrium temperatures of these two bodies. With the help of the Stefan-Boltzmann law the radiative heat flux between two infinite parallel blackbodies facing each other can be derived as

$$q_{12} = \sigma [T_1^4 - T_2^4]. \quad (4.27)$$

In contrast to the blackbody, which absorbs irradiation perfectly, real objects split irradiated energy into three different parts depending on their radiative properties emissivity, reflectivity and transmissivity (see figure 4.5).

Due to Kirchoff's law (absorption=emission) the actual emitted energy of a real object at a certain temperature T_{obj} can be calculated from the expression

$$q_{obj} = \epsilon_{obj} \sigma T_{obj}^4. \quad (4.28)$$

With the help of the presented theory, the net heat transfer of a solid to the surrounding can be calculated as

$$q_{rad} = \epsilon_{obj} \sigma [T_{obj}^4 - T_{\infty}^4]. \quad (4.29)$$

As can be concluded from equation 4.29, the net heat transfer due to thermal radiation is small for objects at ambient temperature. If radiation is of the same order as convection, it must be added to the boundary conditions of the Poisson equation.

Developing theoretical models for the radiative performance of real objects is a rather difficult task, because emissivity, transmissivity and reflectivity are completely different for different types of materials. For practical use it is more suitable to determine these radiative properties empirically. Some values will be given in section 5.3.4.

Chapter 5

Experimental aspects

Next to the presented theory, the experimental aspects are an even more important part of this report. The wall-shear stress measurement relies on highly accurate surface temperature measurements and therefore detailed information about the IR-camera performance is essential. The following sections deal with temperature measurements techniques employed in the present investigation.

5.1 Temperature measurements

The temperature of any fluid or solid has a certain influence on its properties. This temperature dependence can be measured.

There are a variety of temperature measurement devices, which include:

- Thermometers
- Thermocouples
- Resistance Temperature Detectors (RTD)
- Liquid Crystals

Concerning IR-thermography, reference temperatures are needed for the calibration of the IR-camera. For that purpose special demands on the temperature measurement devices have to be fulfilled:

- accuracy higher than the IR-camera ($< 0.1^{\circ}C$)
- small size to fit into small models
- small measurement effort

These requirements can be satisfied best by thermocouples or RTD's. This choice will be easier understood, if the theoretical background of thermocouples and RTD's is taken into account. Some notes will be given in the following sections.

5.1.1 Resistance temperature detectors

The resistance temperature detector (RTD) utilizes the fact, that the specific electrical resistance of some materials depends on their temperature. One of these materials is platinum. In comparison with thermocouples, RTD's have an approximately ten times higher accuracy. The relation between the resistance and the temperature has to be calibrated only once. For the temperature measurement itself, no reference temperature is needed. These advantages lead to a higher price, because of the expensive material used in the measurement wire. Thus RTD's are only used if a high accuracy ($\approx 0.01^\circ\text{C}$ under best conditions) is required, like for the camera calibration or for the determination of the radiative properties in the experimental setup.

For the present experiments a standard Pt100 is used, where 'Pt' denotes platinum and '100' denotes the resistance in Ohm at 0° Celsius. The temperature range of this Pt100 and of some other types of thermocouples are given in table 5.1.

5.1.2 Thermocouples

The main advantages of thermocouples are their flexibility and their low price, as compared with other temperature measurement techniques.

Thermocouples are based on the thermal electrical effect. In principal electrons move freely through an electrical conductor. The kinetic energy of the electrons depends on the temperature of the conductor. The theory of this effect was described by Fermi and Dirac. A simple experiment can demonstrate this. Consider a conductor with different temperatures at both ends. Due to the higher kinetic energy at the warmer end, the electrons have a tendency to move to the colder end. A current U_{th} is built up until an equilibrium with the adverse acting electric field is reached. This phenomenon is sketched in figure 5.1.

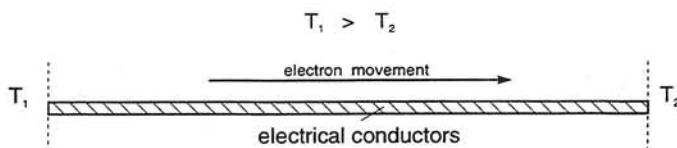


Figure 5.1: Electron movement in an electrical conductor.

If two different conductors a and b are coupled on one side, a voltage can be measured at the loose ends. This combination of two different electrical conductors is called a thermocouple. Figure 5.2 illustrates the setup of a thermocouple.

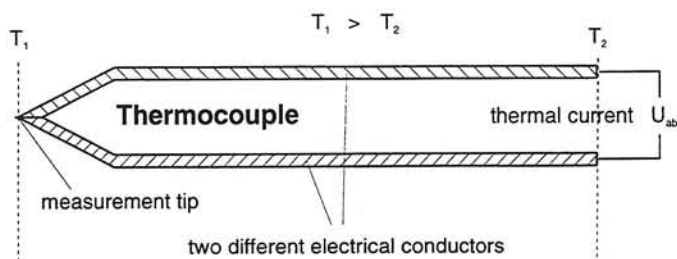


Figure 5.2: Measurement principle of a thermocouple.

Since the thermal voltage is proportional to the temperature difference over a wide temperature range, the current of the thermocouple is

$$U_{th} = S(T_1 - T_2) \quad U_{ab} = U_a - U_b = (S_a - S_b)(T_1 - T_2) = S_{ab}(T_1 - T_2). \quad (5.1)$$

The proportionality constant S_{ab} is called the Seebeck coefficient and defines the characteristic of the thermocouple. The coefficients for different metal pairs can be found in standard books on industrial norms [8].

Under experimental conditions the coupled tip is used as the measurement point, whereas the loose ends are kept at a certain reference temperature and are connected to a voltmeter. Depending on the expected temperature range, different metal combinations have to be chosen. The upper limit is determined by the melting points of the metals or by oxidation effects. If the temperature comes close to the upper limit, large errors are generated. On the other hand low temperatures lead to very small thermal currents, which are difficult to detect. To illustrate the employment of thermocouples and RTD's, the temperature range for different metals are presented in table 5.1:

Table 5.1: Types of thermocouples

	Type	Metals	Temperature Range	
Thermocouples	T	Cu - CuNi	-40	+350
	J	Fe - CuNi	-40	+750
	E	NiCr - CuNi	-40	+800
	K	NiCr - Ni	-40	+1200
	N	NiCrSi - NiSi	-40	+1200
	R	Pt13RH - Pt	0	+1600
	S	Pt10RH - Pt	0	+1600
	B	Pt30RH - Pt6RH	+600	+1600
RTD	Pt100		-200	650
	Pt100		-200	+850

In the present experiments, the standard type K thermocouples are used. Because of their small size, they can be mounted into the test objects to check the readout of the IR-camera. A sufficient contact between the temperature sensor and the measured surface is essential. In some setups this can be supported with special thermal sensor mounting paste.

5.1.3 RTD measurement check

Since the Pt100 RTD is used to calibrate the IR-camera, which demands accurate absolute temperature measurements, the accuracy of the RTD has to be checked.

The Pt100 is placed next to a standard mercury thermometer in a heated water bath. The accuracy of this thermometer is 0.02°C . A propeller inside the water bath takes care for a constant temperature in the water. To minimize heat conduction along the metal housing of the RTD, it must be fully immersed into the water. This increases the amount of water in the bath and with it the heat capacity of the system. The resulting long time period to generate a steady temperature leads to an experiment in the transient regime. The heating of the water bath induces a constant heat flux. The readout of the two devices can be seen in figure 5.3.

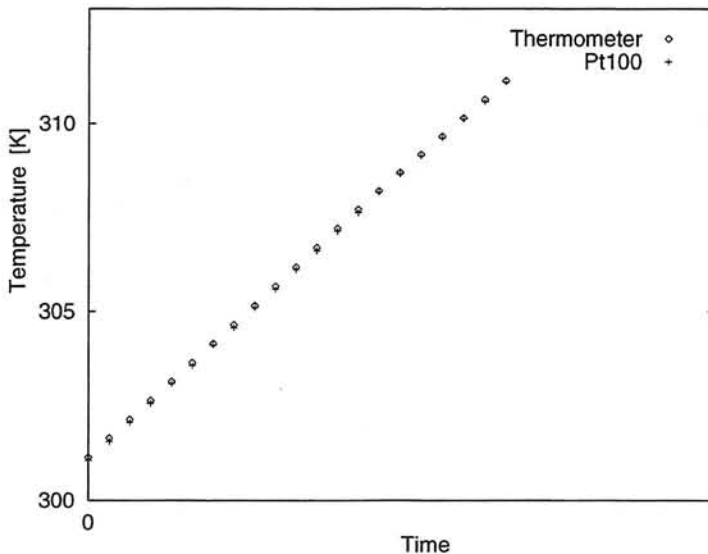


Figure 5.3: Comparison between Thermometer and Pt100 RTD.

The temperature measurements of the RTD and the thermometer show good agreement. The maximum absolute error is less than 0.08 K . Thus the accuracy of the Pt100 is sufficient for calibration purposes, because the maximum detectable temperature difference of the IR-camera, used in the present experiments, is approximately 0.1°C .

5.2 IR-camera

The infrared camera is the main tool in the presented measurement technique. With the sufficient spatial resolution, thermal sensitivity and response time of modern IR-cameras, they satisfy both qualitative and quantitative requirements. Especially for quantitative measurements, detailed information about all parts from the sensor and the scanning system to data processing is essential.

The following description refers to an AGEMA LWB880 IR-camera, which is used for all our experiments.

5.2.1 Sensor

The most important part of an IR-camera is its infrared sensor. As already mentioned, an IR-camera is meant to measure surface temperatures. The emitted radiation of an object passes the camera lens and the scanning system and finally falls upon the sensor inside the camera. The sensor generates an electrical current in relation to the irradiated energy. This process is based on the photo electrical effect. The resulting signal is processed by a 12 bit Analogue-Digital (AD) converter into sampled numerical values. These samples are the basis for further data processing like calculating temperature values, graphical output on the connected computer system or data readout.

Different sensors are available, each with its own sensitivity-wavelength characteristics. The choice of the sensor is determined by the temperature range (see Wien's law) on the one hand and the fluid surrounding the watched object on the other hand. In most applications the measurements are made in air. Thus the radiative properties like the emissivity and the transmissivity have to be taken into account. As already explained, both properties are coupled by the relation $\epsilon_{air} + \tau_{air} = 0$.

These magnitudes are influenced by many factors, like:

- o distance between IR-camera and object
- o air temperature
- o air pressure
- o air compounds (H_2O , CO_2 , CO , N_2O , O_3 , CH_4)
- o particles in the air

With exception of the distance and the compounds H_2O and CO_2 , each of these factors can be neglected at standard conditions. Water and carbon dioxide absorb certain wavelengths in the IR-spectrum, which leads to a decrease of the transmissivity. Figure 5.4 presents the transmissivity of air τ_{air} for different wavelengths at 1 atm pressure, 25° C temperature and 25% humidity at a distance of 30 m.

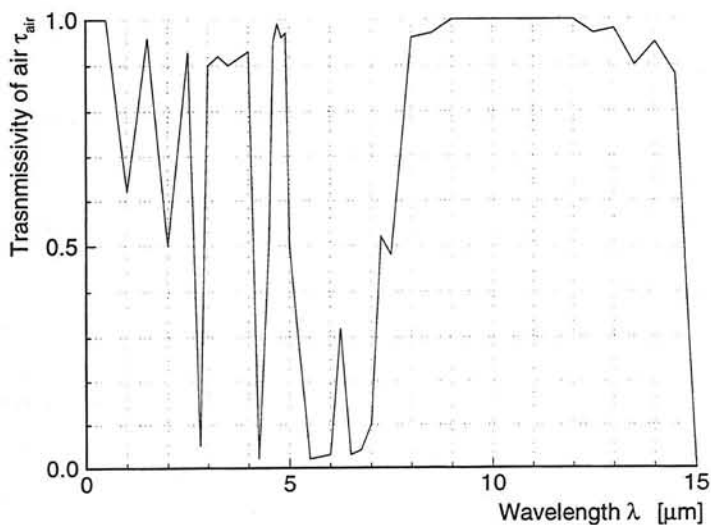


Figure 5.4: Transmissivity of air for different wavelengths.

Areas of reduced transmissivity can be seen in figure 5.4.

The region up to the wavelength of $\approx 5 \mu\text{m}$ is influenced by the absorbing effect of carbon dioxide and the low transmissivity values between $5 \mu\text{m}$ and $8 \mu\text{m}$ are caused by water vapour in the air. Wavelength ranges of high transmissivity are called atmospheric windows. Especially in measurements over long distances (more than 10 m) it is essential to maximize the transmissivity τ_{air} . Thus IR-sensors have to operate in these atmospheric windows. At the moment two main types of sensors are commercially available.

Short Wave Band	SWB	$3\mu\text{m}$	-	$5\mu\text{m}$
Long Wave Band	LWB	$8\mu\text{m}$	-	$12\mu\text{m}$

The choice of the sensor depends on the expected temperature range. Applying Wien's displacement law (see eqn. 4.25), the maximum emissive power of objects at ambient temperatures falls into the long wave band.

The IR-sensor is mounted at the bottom of a liquid nitrogen filled Dewar chamber, to cool it to a temperature of -192°C . This very low temperature of the sensor has two effects. In the first place it gives a large temperature difference between object and sensor, which increases the net energy transport to the sensor (see chapter 4.3). Secondly it improves the signal to noise ratio of the sensor.

Another important part of the IR-camera is its scanning system, to focus the emitted energy of the monitored object onto the infrared sensor.

5.2.2 Scanning system

Most IR-camera have just one sensor. Thus a scanning system is required, which approximates the continuous distribution of the thermal radiation of the surface inside the field of view (FOV) of the camera by a series of single measurements.

The thermal radiation of an instantaneous field of view (IFOV) of one single measurement falls upon the sensor. Since the size of the IFOV is not infinitely small, the sensor detects the integrated emitted radiation along the IFOV. The size of an IFOV is a function of the distance between the camera and the object and of the focal length of the used lens. The integrated radiative energy of one IFOV is converted to a single output value by the AD converter. This output can be displayed on a monitor. In the following one single measurement is called a pixel.

After this conversion the scanning system focusses on another IFOV and its radiation is measured. This procedure is repeated until the radiation of the whole FOV of the camera is determined.

This approximation of a continuum by a finite number of discrete measurements is called sampling and is sketched in figure 5.5.

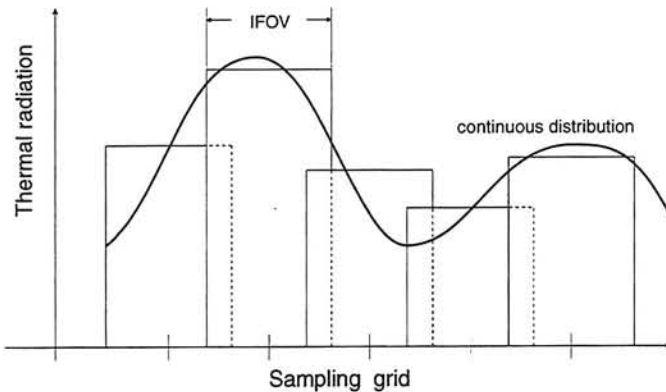


Figure 5.5: Sample procedure.

The positioning of the focus point of the IR-camera along the surface of the object is performed by a mechanical construction of mirrors. The focus point is moved horizontally by a mirror polygon and vertically by an oscillating mirror.

Since the mirrors are driven by motors, electrical fields are built up, which may generate noise in the signal of the IR-sensor. A significant magnitude to describe the influence of the

noise is the "Noise Equivalent Temperature Difference" (NETD), which is $\pm 0.2\text{ }^{\circ}\text{C}$ for the AGEMA 880 LWB camera. This value is independent of the measured temperature. This leads to significant relative errors for measurements of an object that has a temperature, which is only few degrees higher than the ambient temperature.

Figure 5.6 shows the interior of the IR-camera. It illustrates the working of the scanning system distinctly.

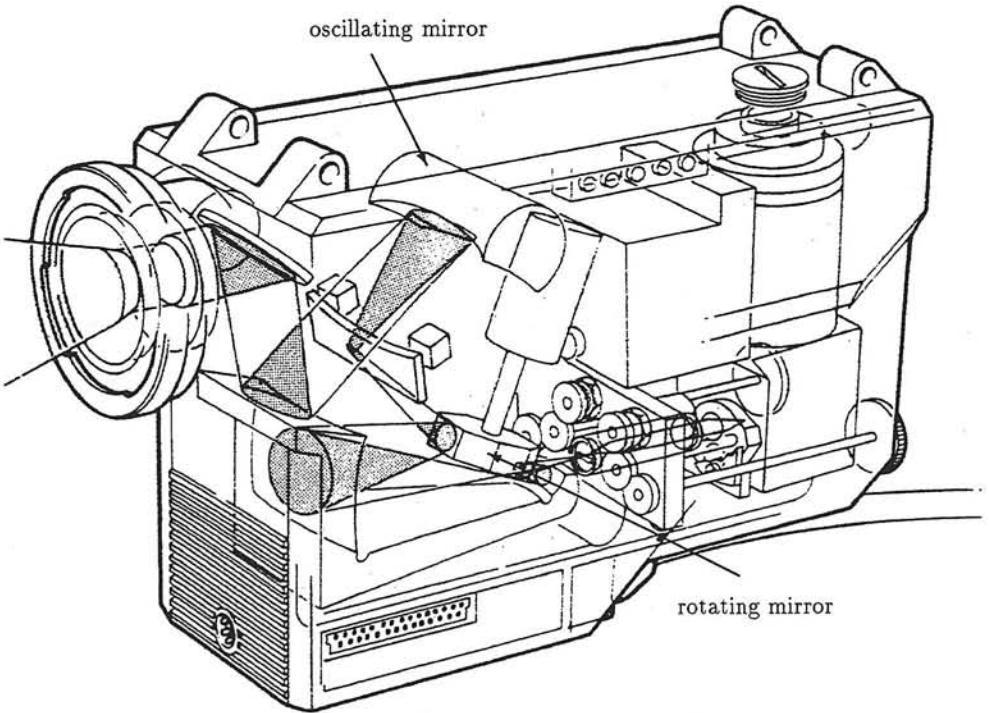


Figure 5.6: Interior of the IR-camera.

Without going into further details about all components of the IR-camera the main attention is given to the scanning system. As already mentioned, the scanning system samples the two dimensional temperature distribution sequentially.

The order in which the pixels are scanned is sketched in the following figure 5.7.

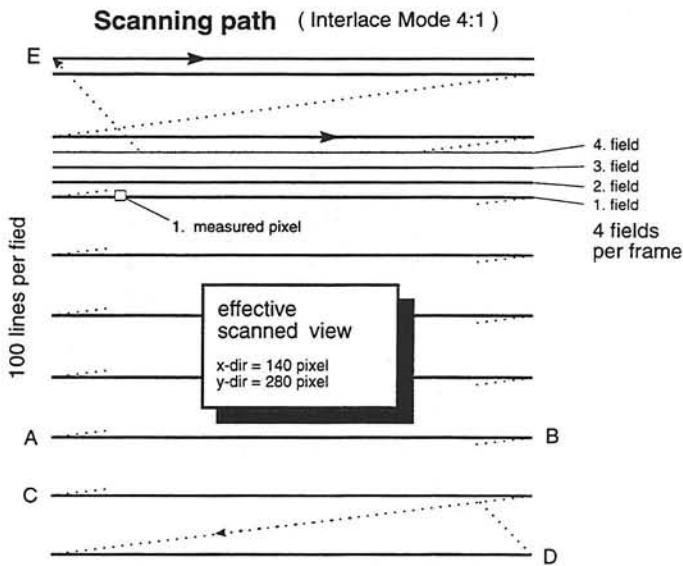


Figure 5.7: Scanning path of the IR-camera.

Defined by the rotational speed of the mirror polygon and the sampling rate of the AD converter, 140 pixels are generated in horizontal direction. The vertical scanning is determined by the frequency ratio of the two mirrors. The scanning system samples the first line at the top of the monitored area. 100 horizontal lines from the top to the bottom are generated before the top is reached again. This group of 100 lines is called a field. Since the frequency ratio between the two mirrors is 100.25, the position of the second field is above the first field. The spatial shift is exactly a quarter of the distance between two lines in one field. Thus four fields have to be scanned to create a complete thermographic frame of 400 lines. This method is called a four times interlaced scanning.

Actually only 70 lines per field can be used, because some lines at the top and the bottom of the field are disturbed by vibrations at the turning point of the oscillating mirror. Thus the maximum resolution of the effective scanned view is 140×280 pixels.

The time scales of the scanning system are given in the following list:

Time per frame	=	160 ms
Time per field	=	40 ms
Time per line	=	0.4 ms (path AB)
		0.0 ms (path BC)

These time scales are given by the manufacturer. To verify these values an experiment has

been performed. The results of this experiment are presented in section 5.3.3.

5.2.3 Focussing

Like any other optical device the IR-camera has to be focussed correctly, which means the minimization of the size of the IFOV. A large IFOV does not only lead to a loss of sharpness of the picture, it also leads to an underestimation of geometrically small temperature peaks, due to the integration of the irradiated energy along the IFOV (see subsection 5.2.2). The principle of focussing is sketched in figure 5.8.

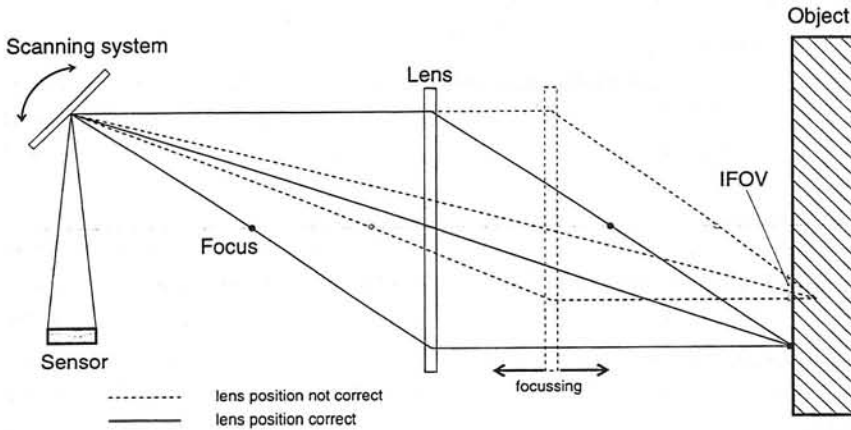


Figure 5.8: Geometrical optics inside the IR-camera.

Especially for the temperature measurement of the laser spot the correct focussing is extremely important. However the laser spot measurement enables a very accurate estimation of the correct focussing. Varying the focus, while the camera is viewing the laser spot, influences the temperature measurement. As the temperature reaches a maximum, the correct focussing is found.

To get an impression on the distances between camera and object that can be correctly focussed and on the resulting FOV, some values for different available lenses and extension rings are given in table 5.2. With the help of an extension ring the spatial resolution can be increased, but the camera has to be much closer to the object. The distance between camera and object is prescribed by the experimental setup in most cases.

Table 5.2: Spatial resolution for different lenses

Lens [Degree]	Extension ring length [mm]	Camera distance [m]	Width of view [m]
7 × 7	...	1.18 - 12.8	0.12 - 1.1
12 × 12	...	0.78 - ∞	0.12 - ∞
20 × 20	...	0.48 - ∞	0.12 - ∞
20 × 20	8	0.16 - 0.22	0.58 - 0.80
20 × 20	12	0.12 - 0.15	0.43 - 0.54
20 × 20	22	0.09 - 0.11	0.32 - 0.40
40 × 40	...	0.27 - ∞	0.17 - ∞

Tests with different extension rings have shown that the spatial resolution of the camera increases with increasing length of the extension ring, but the 22 mm ring leads to distortions at the edges of the field of view. In this investigation a 20 × 20 °C lens with an 8 mm extension ring has been used.

Since the IR-camera observes small objects like laser spots and highly unsteady temperature distributions, like the temperature decay of the laser spot in the unsteady measurement technique, the described sensor-scanner system generates large errors. They are mainly caused by the sampling method and the sequential data production.

In the following section methods are described to estimate and compensate these errors.

5.3 Quantitative IR-Thermography

Compared with the previous section, which mainly describes the working of the IR-camera, this section presents the consequences on the quantitative IR-Thermography.

An IR-camera transfers the emitted energy of an object, which depends on its surface temperature T , into digital values S . In general a relation between the output of the IR-sensor and the temperature of an object is found by calibration. However under certain circumstances the output signal is modulated and relevant deviations from the calibration curve are generated.

5.3.1 Split response function

Since the IR-camera is employed to measure the temperature of a surface with large spatial temperature gradients, those occurring in a laser spot, errors in the temperature measurements are generated. These errors are related to the temperature gradients and are caused by integration of the radiation emitted from an IFOV, which has a finite size even when the camera is correctly focussed. In the following experiment the size of the IFOV is determined. The experiment consists of a blackbody at a constant temperature T_b . The IR-camera watches the blackbody through a diaphragm with an adjustable split. By varying the split width w the relation between w and the measured sample value $S(w)$ can be determined.

The ratio between S_{max} and the actual $S(w)$ is called the Split Response Function (SRF). The SRF can be calculated from the following relation:

$$SRF(w) = \frac{S_{max}}{S(w)}. \quad (5.2)$$

The setup of this experiment is sketched in figure 5.9.

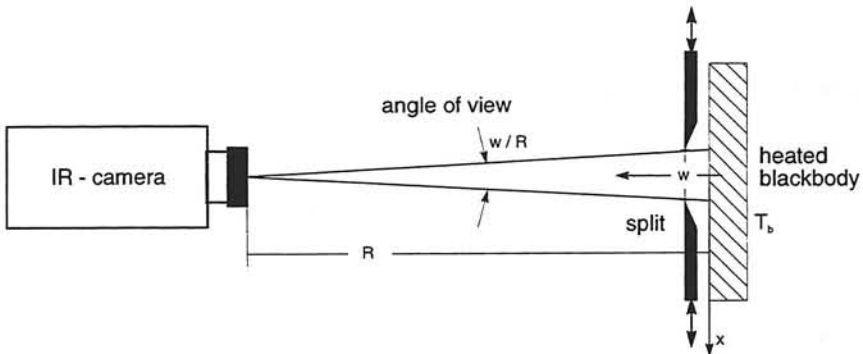


Figure 5.9: Determination of the SRF.

The sample values $S(w)$ for different spot widths w and the resulting SRF can be seen in

figure 5.10 and 5.11.

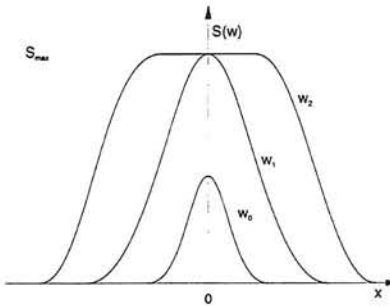


Figure 5.10: Digital camera output.

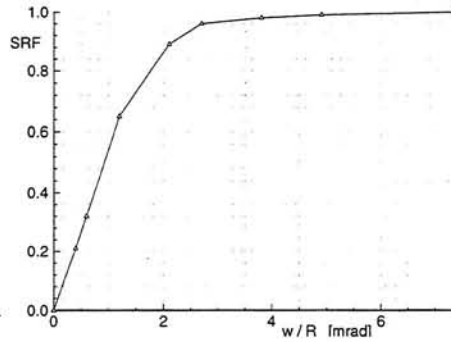


Figure 5.11: Split response function.

This experiment shows that the camera signal S_{max} is constant as long as w is larger than the size of the IFOV. Thus it can be concluded from figure 5.11, that the temperature of objects larger than 0.004 mrad is measured with a sufficient accuracy. This limit has to be kept in mind in the definition of the laser spot diameter.

5.3.2 Modulation transfer function

Another possibility to describe the spatial resolution of the camera is the modulation transfer function (MTF), which can be determined by a mathematical approach described by de Luca [5]. Basically the MTF is a normalized Fourier transform of an impulse response. Since the MTF depends mainly on the sampling procedure, detailed information about the size of the IFOV, the sample grid, the sample frequency and some more optical parameters is required. Generally the combination of lens, scanning system and sensor act like a low pass filter. The next two graphs illustrate this low pass filter effect.

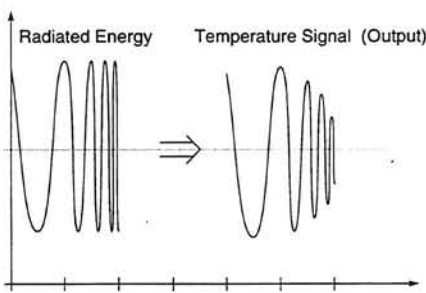


Figure 5.12: Input - output signal.

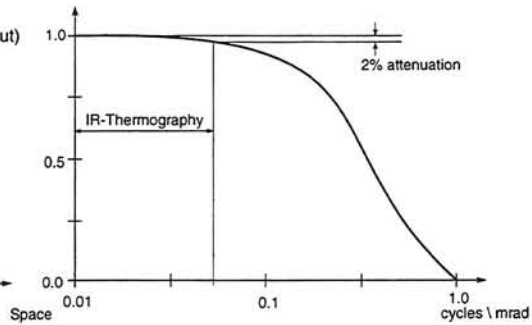


Figure 5.13: Modulation transfer function.

Since the necessary parameters are not available for the AGEMA 880 LWB camera, Figure 5.12 and 5.13 just serve as a general explanation of the MTF. In fact the MTF in figure 5.13 has been obtained by ONERA for a certain commercial IR-camera [6]. The results in later sections will show that the definition of the laser spot with the help of the SRF leads to sufficient accurate temperature measurements.

Besides the spatial resolution, also the time response contributes the performance of quantitative IR-thermography. This is the restricting factor in monitoring moving objects or transient temperature distributions.

5.3.3 Time response

As already described in section 5.2.2, the IR-camera scans the field of view in a certain pattern. One picture with a resolution of 140×280 pixels is generated in 160 ms . Especially the interlace mode of 4:1 leads to a time shift effect, which can not be neglected, even not for small areas of interest inside the field of view.

In the following description the 280 camera lines in y -direction are numbered from 1 at the top of the image to 280 at bottom. The scanning system begins with line 4, 8, 12 et cetera. After the first field has been completed, the sequence of lines 3, 7, 11 et cetera is measured, which determines the second field. In a similar way the third and the fourth field are scanned. This pattern leads to a time difference between two lines; for example there is a time difference of 40 s between line 3 and 4.

The time shift between the different lines can be verified with the help of a simple example. Consider a plate with $Bi \ll 1$ (constant temperature in the plate) in a quick cooling process. The temperature distribution in y -direction measured by the camera during this cooling process is sketched in figure 5.14.

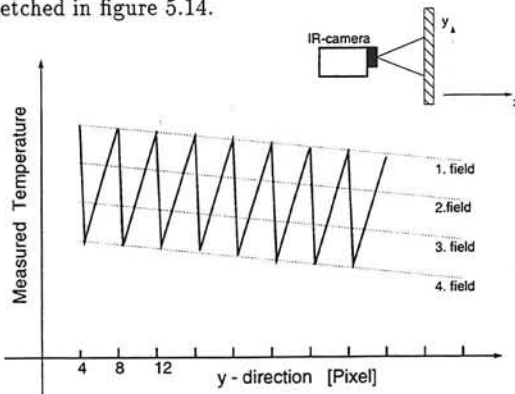


Figure 5.14: Temperature output in cooling process.

The just described phenomenon that two neighbouring pixels are measured at different time levels occurs also in x -direction. However the high line frequency of 2500 Hz , which means that one line is generated in 0.4 ms , leads to a negligible error in x -direction compared with the time between two pixels in y -direction.

To check the time scales given by ONERA for the AGEMA LWB 880 camera, an experiment very similar to the just mentioned example has been developed. An aluminium plate is heated by an electrical heater glued on the backside. Because of the large conductivity of aluminium it can be assumed that $Bi \ll 1$ which implies that the temperature is uniform at the surface and only depends on the time. It has to be pointed out that it is rather difficult to find a heater, which generates a constant temperature field at any time step, although $Bi \ll 1$. Since the plate is heated quickly, a sawtooth signal, similar to the one sketched in figure 5.14, is measured by the camera during heating up.

With the help of a simple linear interpolation procedure the time at which the pixel is generated can be calculated. To define the temperature gradient, the temperature difference between the first pixel of one frame $T_{1,4}^0$ and the first pixel of the following frame $T_{1,4}^1$ is divided by the time to generate one frame (160 ms). Since all the other pixels $T_{i,j}^0$ of the first frame are generated between $T_{1,4}^0$ and $T_{1,4}^1$ and their order of generation is known, the time at which they are generated can be calculated from the following expression:

$$t_{i,j} = \frac{T_{i,j}^0 - T_{1,4}^0}{T_{1,4}^1 - T_{1,4}^0} \cdot 160\text{ ms} \quad (5.3)$$

Figure 5.15 illustrates the interpolation procedure.

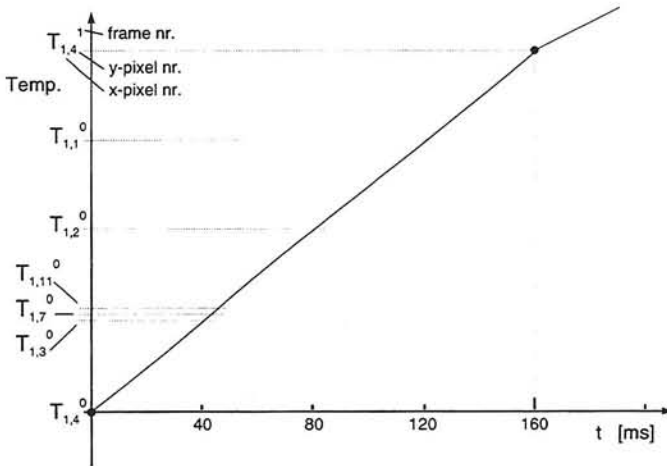


Figure 5.15: Interpolation procedure.

The following time scales are obtained by averaging the calculated values for $t_{i,j}$ over many frames:

Time per frame	=	160 ms
Time per field	=	39.97 ms
Time per line	=	0.39 ms

With the help of these time scales, the time-shift effect can be reconstructed. Figure 5.16 and 5.17 show the measured and the reconstructed temperature distribution of the plate in a series of camera pictures.

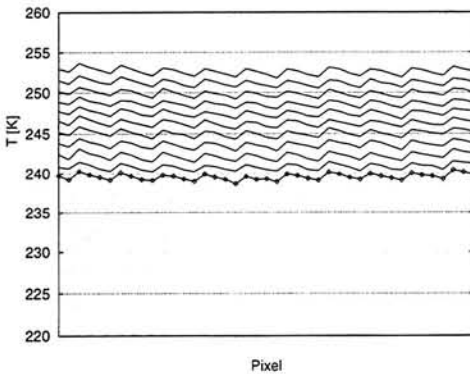


Figure 5.16: $T(y)$ (measured).

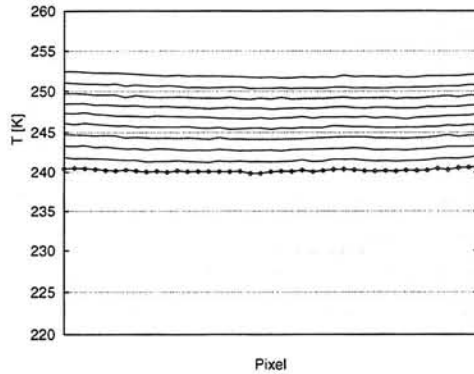


Figure 5.17: $T(y)$ (reconstructed).

Figure 5.17 shows that this reconstruction is able to correct the time shift effect significantly, because there are no periodic patterns in the reconstructed temperature distribution.

The small remaining disturbances are generated by signal noise of the IR-camera. This noise can be minimized by averaging a series of pictures for steady applications or by using noise reduction filters for transient measurements. The decrease of the temperature distribution in the middle of the plate is caused by non-homogeneous heating.

5.3.4 Emissivity of real objects

Blackbodies emit their energy with a constant power over the hemisphere. The emissivity of real bodies show a strong dependence on the optical angle of incidence. This relation between the emissivity ϵ_r and the angle ϕ is highly material dependent. In general, electrical conductors exhibit complete different behaviour as compared to non-conductors. Non-conductors have a higher emissivity and they radiate their thermal energy mainly at an angle between 0° to 60° . The maximum in $\epsilon_r(\phi)$ for conductors lies close to 80° . The angle dependence of different materials can be found in standard text books [7].

Three examples for the dependence of the emissivity $\epsilon_r(\phi)$ on the angle ϕ are given in figure 5.18 and 5.19.

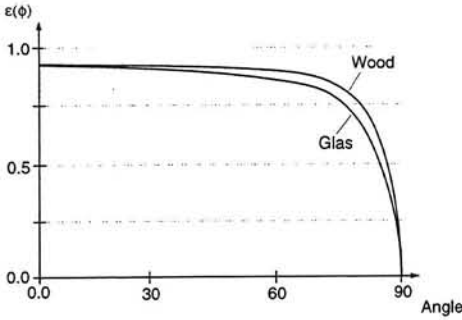


Figure 5.18: $\epsilon_r(\phi)$ for non-conductors.

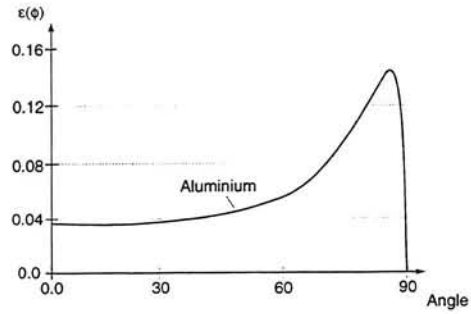


Figure 5.19: $\epsilon_r(\phi)$ for conductors.

To apply IR-thermography to wall-shear stress measurements, different requirements on the surface of the object have to be satisfied. In the first place, the emissivity has to be maximized to increase the emitted energy and reduce the influence of the surroundings. If the emissivity of the object is smaller than 0.8, the surface has to be coated. Unfortunately most available high emissivity colour coatings for IR-thermography try to achieve a blackbody, which has diffuse radiation, by applying a rough surface. This diffuse radiation is an advantage for quantitative IR-thermography, but the roughness of these coatings may also influence the flow and might falsify the drag measurement. Thus a compromise between high emissivity and smoothness has to be found.

The angle dependence of the emissivity $\epsilon_r(\phi)$ of the object surface has to be determined, if the temperature of a curved body, like an airfoil, is measured. The relation $\epsilon_r(\phi)$ of a commercial dull black colour is compared with the angle dependence of the high emissivity rough colour coating NEXTEL. The developed experiment to determine $\epsilon_r(\phi)$ is sketched in figure 5.20 and the results of the comparison in figure 5.21.

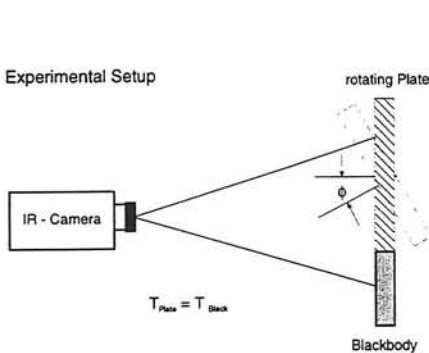


Figure 5.20: Test setup.

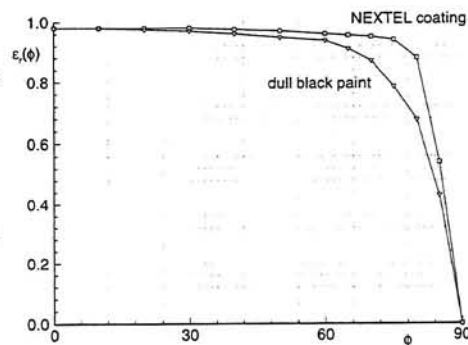


Figure 5.21: $\epsilon_s(\phi)$ for two coatings.

The function $\epsilon_r(\phi)$ is determined by the ratio between the actual measured sample value $S(T, \phi)$ and output of the IR-sensor for the blackbody $S_b(T)$ at the same temperature:

$$\epsilon_r = \frac{S(T, \phi)}{S_b(T)}. \quad (5.4)$$

From figure 5.21 it can be concluded that the emissivity ϵ_r is constant up to $\phi = 30^\circ$ for both colours tested. Because of the rough surface of the NEXTEL coating, the emissivity has higher values at steeper ϕ angles compared with a commercial dull black paint.

Although the NEXTEL coating has less angle dependence than the black paint, the black paint will be used, as it is smoother and thus has less effect on the laminar-turbulent transition in the velocity boundary layer.

5.4 Experimental setup

To measure wall-shear stresses with IR-thermography, a series of components are necessary:

- o test object
- o IR-camera
- o camera operation module
- o external heater (IR-lamp, laser)
- o post-processing module

Figure 5.22 sketches a typical experimental test situation.

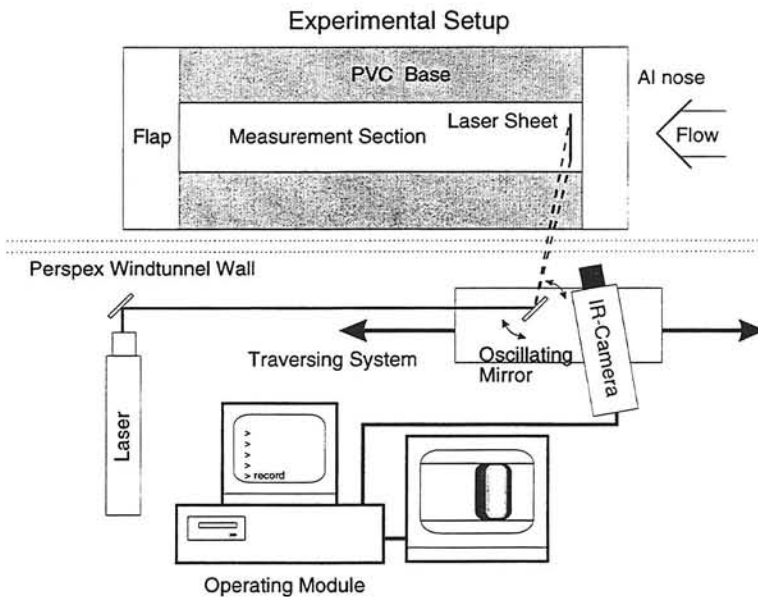


Figure 5.22: Standard experimental setup.

The IR-camera is monitoring the laser-generated hot sheet, which decays in temperature under the influence of the flow. The laser and the IR-camera are mounted on a plate, that can be moved in flow direction. In this way the position of the measurement point can easily be varied. The camera watches the plate through a slit in the wind tunnel wall, which is made of perspex. Since the transmissivity of perspex is close to zero for IR-radiation, a slit has to be milled in the wall. To prevent disturbances in the flow generated by the slit, it is covered with a thin transparent foil, which has a transmissivity close to one.

The measurement data are sent through an insulated wire to the operating module, which controls the camera and builds up the images on a monitor. For data postprocessing the images can be transferred via an internet card to a workstation.

This experimental setup leads to following radiative conditions for the IR-camera.

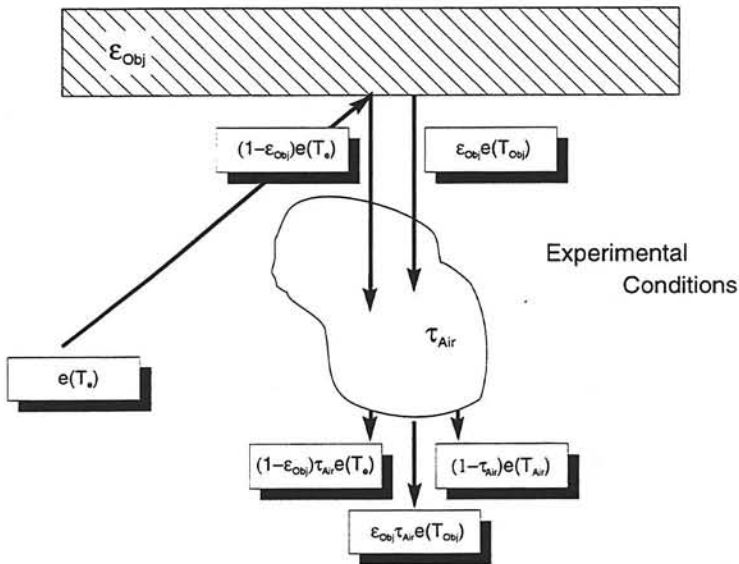


Figure 5.23: Radiative conditions for the IR-camera.

As can be concluded from figure 5.23, the emissivity ϵ_{obj} and the transmissivity τ_{air} have to be maximized to receive maximum emissive power $e(T_{obj})$ from the object with minimum disturbances from the surroundings. If the term $(1 - \epsilon_{obj})$ is not close to zero, the so called "Narcissus-effect" can arise. This effect can be explained as follows. Generally it is advantageous to place the camera perpendicular to the model surface, to minimize the influence of the angle dependence of the coating. However in that case the camera watches part of itself, namely the liquid nitrogen cooled Devar, which can be seen as a cold spot on the temperature image.

Reflections from the surrounding have to be aware of, even in closed wind tunnel sections. These reflections can produce disturbances, caused by the radiation of warm fences and honeycombs reflecting through the wind tunnel, which can be monitored on the model with the IR-camera.

The second important radiative property, the transmittance τ_{air} , can be assumed to be one for the typical distance of a few meters between object and camera in a wind tunnel experiment (see figure 5.22).

To complete the overview of the experimental setup, some details about the capabilities of the camera operating module and the different types of lasers will be given in the following sections.

5.4.1 IR-Camera operating module

The AGEMA BRUT V3.1 operating module consists of the following components:

- o processor unit
- o internal memory (storage up to 92 picture)
- o floppy drive
- o tape streamer
- o 2 monitors (interactive command screen, graphical output)
- o network connection

Its main task is to create a picture from the IR-camera data. These pictures can be presented in the interlaced frame mode or in the low-resolution field mode, which increases the picture frequency to 25 Hz. The unit of the output data can be optionally chosen as the degree centigrade, degree Kelvin or a sample value.

Next to the pure visualization there are some options to read out values on-line from the camera images:

- o temperature values in 5 positions in the camera image
- o minimum, maximum and average temperatures in a pre-defined area
- o temperatures along a line
- o temperature histogram
- o two temperature isolines

For additional data postprocessing there are possibilities to store IR-pictures on floppy, tape or directly on a workstation disk via internet. Generally speaking the binary output of the internal AD converter is saved. These sample values S are saved pixel after pixel in the same pattern as they are scanned (see section 5.2.2).

To calculate temperatures T in Kelvin from the sample values the BRUT software of the operating system uses the following calibration formula:

$$T = \frac{B}{\ln\left(\frac{R}{P_{IU} S} + F\right)}, \quad (5.5)$$

sample values	=	S
IU per sample value	=	$P_{IU} = 6.1042 \cdot 10^{-2}$
spectral factor	=	B
response factor	=	R
shape factor	=	F .

The necessary parameters P_{IU} , B , R , F are specified in the header of the BRUT output files. Except for the constant P_{IU} , the other parameters depend on the specific combination of scanner, lens and aperture. AGEMA finds these parameters by fitting equation 5.5 to a measured calibration curve.

Since equation 5.5 is developed for a large temperature spectrum, a higher accuracy of the temperature measurement can be achieved, if a special calibration curve is determined between temperature and digital output for the specific temperature range.

Further information can be found in section 5.5.

5.4.2 Laser

There are many ways to generate temperature gradients. The use of a laser, however, seems to fulfill the demands of a local heating best.

Lasers differ in the irradiated wavelength and in the maximum emissive power. Because of their tiny beam diameter they offer a large energy density. A typical size of a laser beam can be estimated as $1-3\text{ mm}^2$. Thus high local temperatures can be achieved.

Unfortunately using a laser requires to find a compromise between different factors. On the one hand the total power of a laser is small compared to an electrical heater. The laser power is proportional to the time scale of the temperature decay of the hot spot in the unsteady method. This time scale must stay in a certain range because of the limited time response of the camera ($> 1\text{ s}$). On the other hand increasing the laser power means increasing the temperatures in the hot spot, which violates the assumption of constant flow properties.

For heating purposes, three different types of lasers were tested:

Table 5.3: Laser types.

Power	reacting Gases	Wavelength
0.5 <i>mW</i>	<i>HeNe</i>	0.632 μm
5.0 <i>W</i>	<i>Ar</i>	0.476 μm
		0.488 μm
		0.514 μm
10.0 <i>W</i>	<i>CO₂</i>	10.5 μm

Compared with the others, the *HeNe*-laser radiates the less energy and it generates a temperature gradient which is insufficient to be detectable with an IR-camera.

The *CO₂*-laser with its high power is difficult to use in experiments due to two reasons. First of all, the laser beam is not visible with the human eye and can be extremely hot. This makes it crucial and dangerous to adjust lenses or mirrors in the optical path. These lenses and mirrors for are also very expensive because of their special coating. Second the laser

does not run continuously, but it is pulsating. The total emissive power is proportional to its pulse frequency. This leads to interferences with the field frequency of the IR-camera in steady measurements, which completely destroys the image.

The *Ar*-laser is the best choice for external heating. It combines steady radiation with a *Gaussian* intensity distribution across the laser beam. This distribution can be handy, if the measurements are compared with numerical calculations. For moderate conductivities of the surface layer ($< 10 \frac{W}{Km^2}$), it can generate sufficiently large temperature gradients. Some more details about the relation between the maximum temperature gradient and the surface conductivity can be found in chapter 7.

Generally the external heater has to be placed under a certain angle with respect to the model to avoid reflections striking the IR-camera. Even for high emissivities these reflections lead to large errors in the surface temperature measurement.

5.5 Calibration procedure

The calibration of the IR-camera is an important procedure at the beginning of any series of experiments. It is decisive for the accuracy of the measurement.

The calibration links the irradiated energy and thus the digital output of the AD converter with the absolute temperature. This can be done with the help of equation 5.5 as obtained by AGEMA. This relation was developed for a rather wide temperature range (-200°C to 1200°C). Accurate measurements are expected to be obtained with the help of a special calibration curve for the main temperature range in the present experiments ($10^{\circ}\text{C} - 40^{\circ}\text{C}$). Basically there are two methods to perform the calibration.

To compensate the influences of the surroundings, surface emissivity, windows in the optical path et cetera, a reference temperature measurement device has to be fixed inside the test object. It is necessary to make sure that the measured temperature is equal to the surface temperature. If the calibration curve is made under exactly the same conditions as the measurement itself, the amount of error sources is minimized.

For cases in which external surface temperature measurements on the object can not be performed, a blackbody is required as a reference. With the help of a blackbody the radiative properties of each participated material can be evaluated separately. Although a blackbody does not exist in nature, it can be approximated by a certain construction.

Figure 5.24 shows an experimental blackbody.

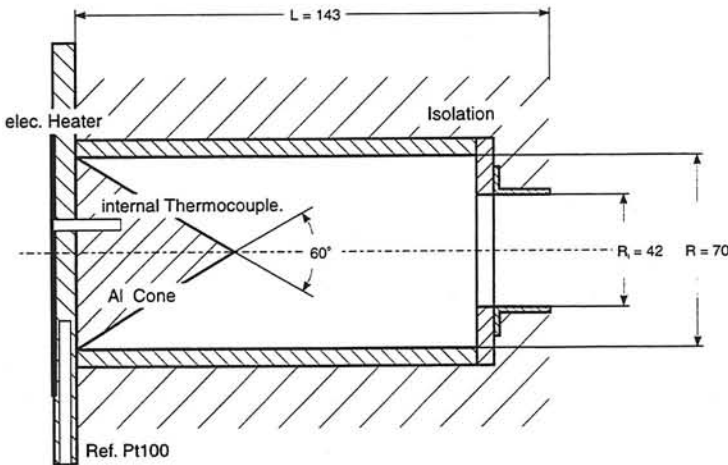


Figure 5.24: Experimental blackbody.

A blackbody is a perfect absorber of radiation. This demand is approximated by a cylindrical cavity with a small aperture. If incident radiation, passing the opening, strikes the

inside surface of the cylinder, a part of it is absorbed and the remainder is reflected. The reflection hits other parts of the wall and again this radiation splits into an absorbed and a reflected part. The ratio of reflection and absorption is defined by the emissivity ϵ_w of the inside surface. It is evident, that if the opening to the cavity is very small, very little of the original incident beam will manage to escape the cavity through the opening. Thus, if the opening is made sufficiently small, the opening area approaches the behaviour of a blackbody, because essentially all the radiation entering through it is absorbed. To keep the cavity at a uniform temperature, so that the internal radiation is in thermal equilibrium, the cavity is constructed from an aluminium cylinder and is surrounded by isolation. By heating the cavity, a source of black radiation is obtained at the opening, since a perfect absorber is also a perfect emitter (see Kirchhoff's law).

The apparent emissivities ϵ_b of the bottom of the experimental blackbody for different geometries denoted by the ratios R_i/R and L/R and different emissivities of the inside walls of the cavity ϵ_w are presented in the following table 5.4 [4].

Table 5.4: Apparent emissivity at the centre of cavity bottom.

ϵ_w	R_i/R	$L/R = 2$	$L/R = 4$	$L/R = 8$
0.25	0.4	0.916	0.968	0.990
	0.6	0.829	0.931	0.981
	0.8	0.732	0.888	0.969
	1.0	0.640	0.844	0.965
0.50	0.4	0.968	0.990	0.998
	0.6	0.932	0.979	0.995
	0.8	0.887	0.964	0.992
	1.0	0.839	0.946	0.989
0.75	0.4	0.988	0.997	0.999
	0.6	0.975	0.993	0.998
	0.8	0.958	0.988	0.997
	1.0	0.939	0.982	0.996

Since the emissivity ϵ_w of the coating (NEXTEL) inside the cavity is much higher than 0.75, the emissivity of the experimental blackbody can assumed to be one with good approximation.

With the help of this blackbody the IR-camera can be calibrated. To determine the function $S_b(T)$ the blackbody must be heated. The heating at the bottom of the blackbody is regulated by an electronical system (WATLOW). The electronics send current pulses to the heater. With the help of the temperature measurement of the internal thermocouple, the system calculates the pulse frequency and intensity. After one hour fully steady conditions are reached.

To check the accuracy of the internal thermocouple, the measured temperature values were compared with an external Pt100, inserted in the centre of the aluminium cone, and the IR-camera measurement. Figure 5.25 presents the temperature difference between the temperature measurements of the internal thermocouple and the Pt100, and between the IR-camera and the Pt100. The temperature of the camera measurement is calculated with the BRUT software calibration equation 5.5.

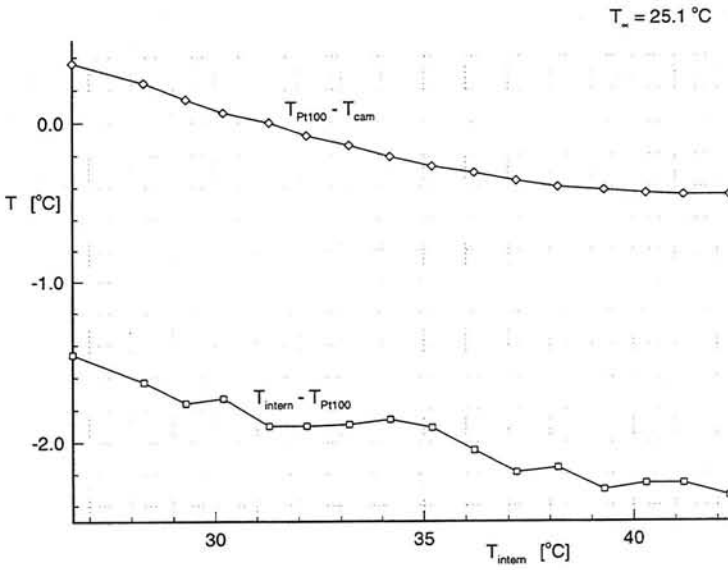


Figure 5.25: Temperature measurements in the blackbody.

Two important conclusions can be drawn from figure 5.25:

1. Since the temperature measurement of the Pt100 can be assumed to be correct (see section 5.1.3), the internal thermocouple is not correctly calibrated. Thus the Pt100 has to be used to measure the temperature of the blackbody.
2. The temperature difference between the Pt100 and the IR-camera measurement, which is up to $0.4^{\circ}C$ in the temperature range between $25^{\circ}C$ and $45^{\circ}C$, shows clearly that equation 5.5 is insufficiently accurate. This leads to the necessity to perform a special calibration of the IR-camera for this temperature range.

The calibration consists of following steps:

First a certain temperature is adjusted with the WATLOW circuit. After a steady state condition has been reached (approximately after one hour), a series of pictures are recorded with the camera, while the temperature is also measured with the external Pt100. To reduce

the noise in the signal, the sample values have to be averaged out of the series of pictures. The procedure is repeated for other temperatures.

Figure 5.26 presents the temperature of the blackbody versus the sample values of the AD converter from the calibration procedure.

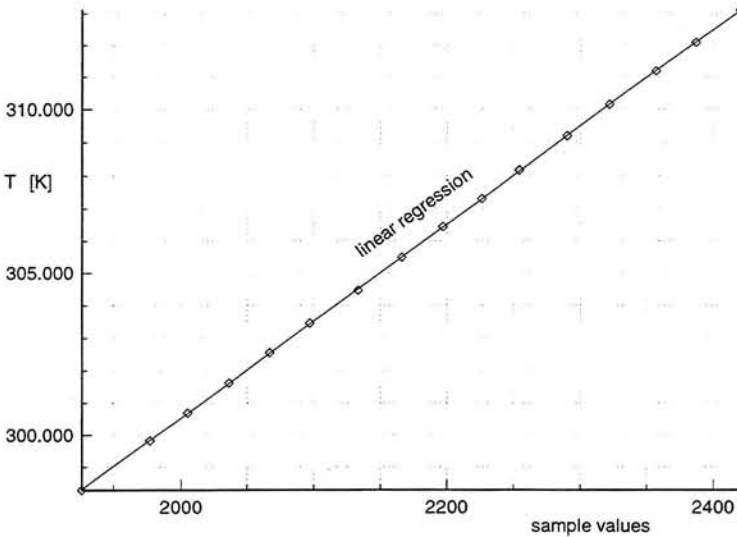


Figure 5.26: Calibration of the AGEMA 880 LWB IR-camera.

With the help of these calibration points, the temperature T for arbitrary sample values S can be calculated by linear interpolation. Since the temperature seems to be proportional to the S values, the calibration curve can be approximated by a linear regression. The maximum relative error between the calibration and the regression is less than 0.5%. The use of linear regression leads to an improvement in the data post-processing time.

As long as the calibration curve $S_b(T)$ is determined accurately, the radiative properties of all applied objects, like the emissivity of the surface or transmissivity of the transparent foil in front of the camera, can be determined by the following relation:

$$\text{Radiative Property} = \frac{S_{\text{Object}}(T)}{S_b(T)}. \quad (5.6)$$

Since the radiative properties of the employed materials can be assumed to be independent of the temperature in this temperature range, one temperature measurement is sufficient to determine the values of their radiative properties. The radiative property of the complete optical path can be calculated by multiplying the subsequent properties.

5.6 Laser irradiation measurement

As already mentioned in the theoretical part of this report, the accurate determination of the heat source power is essential, if measurements are made in the steady state. The irradiated energy of the laser q_{in} can be measured by a simple experiment.

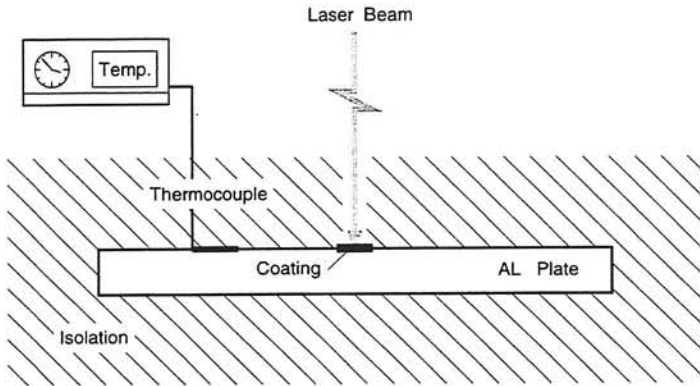


Figure 5.27: Laser irradiation measurement device.

Due to the high conductivity of aluminium and due to a sufficient isolation around the aluminium plate, the Biot number for the heat transport in the aluminium is much smaller than one. Thus the heating power P can be determined by (see equation 4.20):

$$P = \epsilon_{pl} P_{laser} = \rho_{pl} c_{pl} V_{pl} \frac{\partial T}{\partial t}. \quad (5.7)$$

where the subscript pl denotes the plate and V_{pl} denotes the volume of the plate. The laser striking the aluminium plate, which is coated with a colour of emissivity ϵ_{pl} , irradiates energy constantly. While the plate is heated, the temperature difference in time is measured with a thermocouple. Because the Biot number is small, the temperature in the plate can be assumed to be constant. Thus only one temperature measurement point is needed. This assumption was verified in a preliminary experiment with the help of a second temperature measurement at another point of the aluminium plate. Due to the isolation, no heat is able to escape and thus the first derivative of the temperature in time is constant. The heat loss along the entry hole for the laser can be neglected, because of its small diameter. The term ϵ_{pl} defines how much of the irradiated heat is actually used for heating purposes. Its value can be determined with the help of the blackbody (see section 5.5). However, in the presented measurement technique only the heating power P is of interest. Since the aluminium plate is covered with the same high-emissivity coating as the test object, it is possible to measure the value of P directly with the help of this experiment.

Figure 5.28 presents the temperature increase in time for different laser power P_{laser} , which is adjusted by varying the electrical field inside the laser tube. The electrical field influences the amount of stimulated Ar-atoms. The values for the heating power P in the table of the graph are calculated with the help of equation 5.7.

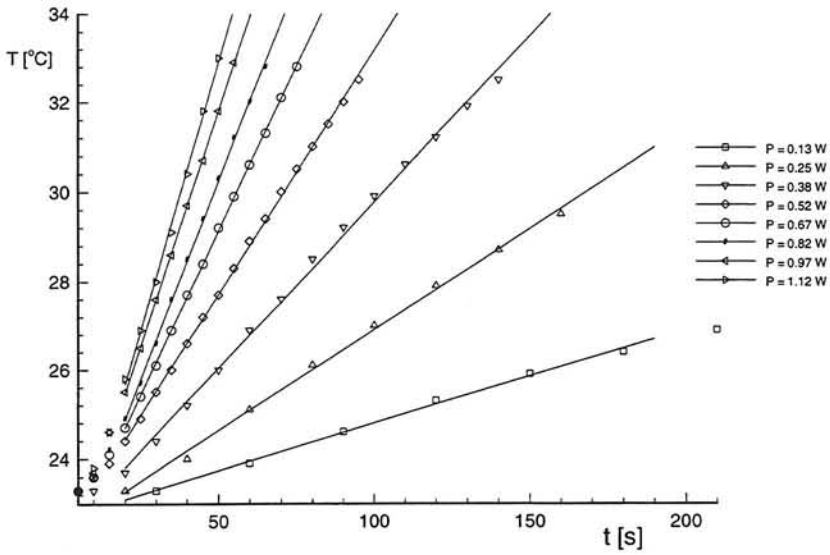


Figure 5.28: Radiated power of the laser.

Chapter 6

Numerical analysis

The calculation of wall shear-stresses from unsteady temperature measurements, performed by the IR-camera, leads to a relatively large numerical effort.

The following sections describe the evaluation of accurate temperature values from the camera output and the determination of the heat flux from the solid to the flow. Finally this chapter deals with a closer look at the wall-shear stress calculation.

6.1 Data acquisition

Although it is rather simple to visualize the temperature measurement of the IR-camera on the monitor of the BRUT system, a series of data-processing routines had to be developed to determine the temperature distribution of the hot spot. At the beginning of this section the different components of the data acquisition are presented. These components are used in the data-processing program BRUT_S, which is described in subsection 6.1.3.

6.1.1 Format of the BRUT output file

To calculate temperature data from the sample values saved in the output file, it is necessary to understand the format of the file.

For any IR-camera measurement many different parameters can be set. These are stored in the file header. In this header the calibration factors R, B and F can be found. With the help of these factors and equation 5.5 the temperatures can be calculated from the given sample values, which are stored after the header.

Table 6.1 describes the layout of the file header in detail.

Table 6.1: File header.

Byte offset	Description	Type
0	identification of the file (constant hex. number 98233289)	integer
4	image width (constant 140 pixel)	integer
8	image height (constant 180 pixel)	integer
12	pixel representation (constant 16)	integer
16	number of fields per frame (constant 4)	integer
20	user comment	string
100	date of file (00, year, month, day)	integer
104	time of file (h, min, s, ms)	integer
108	scanner type	string
134	scanner comment	string
142	date of trigger (00, year, month, day)	integer
146	time of trigger (h, min, s, ms)	integer
150	R-factor	float
158	B-factor	float
166	F-factor	float
174	α atmospheric attenuation	float
182	β atmospheric attenuation	float
190	distance scanner to calibration blackbody	float
198	temperature of the atmosphere	float
206	temperature of the ambient	float
214	P_{IU} isothermal unit per sample value	float
222	emissivity for the spot temperature calculation	float
230	distance scanner to spot	float
238	emissivity for the area temperature calculation	float
246	distance scanner to area	float

The parameters, which are of a float type, are stored as a UNIX type 8 byte floating point number. The presented file header belongs to files saved on floppy or transferred via the internet card to a workstation. The file header of a tape streamer file is slightly different (see AGEMA manual).

After an offset of 256 byte the sample values of the IR-sensor are stored in the same pattern as they are generated (see section 5.2.2). These sample values are UNIX type 2 byte integer numbers. Since the output of the AD-converter is a 12 bit number bit 13 to 15 are zero. The 16th bit is used by the BRUT system. To guarantee a correct reading of the data, the 16th

bit must be set to 0. It has to be emphasized, that if the camera data is processed on a PC, the two bytes of the sample value have to be swapped.

The different camera frames, which contain $140 \times 280 \times 2$ bytes, are directly saved behind each other.

6.1.2 Raw data manipulation

The IR-camera measures the temperature in the $x - z$ plain on the surface of the object. The raw measurement data are influenced by noise and reflected irradiation. Much attention has to be paid on noise reducing routines.

Subtracting reference frame

In some cases, especially if the emissivity of the surface is low, reflected radiation, which is not emitted by the observed surface, reaches the sensor and leads to temperature measurement errors. In this cases it is advantageous to subtract a reference frame from each measured frame. As long as the reflected energy is constant and independent of the observed effect, the errors can be eliminated.

Noise reduction

As already mentioned, the motors for the mirrors and the sensor in the camera introduce noise into the signal. To minimize this noise different methods can be applied. The choice of the method depends on whether the measured temperatures are steady or unsteady.

For steady measurements the frames can be averaged. To achieve a sufficient noise reduction at least ten frames have to be used. The striking advantage of averaging is the elimination of noise without flattening the temperature peaks as occurs in many filtering methods.

Obviously averaging can not be used in unsteady measurements. In the presented investigation two different filter methods were tested. In contrast to splines each filtering method changes the data, thus the more the data is filtered, the more information of the raw data is lost. Thus usually a compromise between smoothness and data loss has to be found. Best results have been obtained by a 5 point cubic data fit (CPF). Additionally a fast Fourier transformation (FFT) method has been tested. The high frequencies of the noise are cut off by a low pass filter. But especially these frequencies, which are cut off by the filter, are necessary to reconstruct high spatial temperature gradients. Comparing these two filters the FFT filter reduces noise much better than the CPF, but it tends to give a strong decrease of the maximum temperature in the hot spot.

Figure 6.1 to figure 6.6 presents the temperature of the complete laser sheet and the temperature $T(x)$ in the middle of the field of view for the different filters.

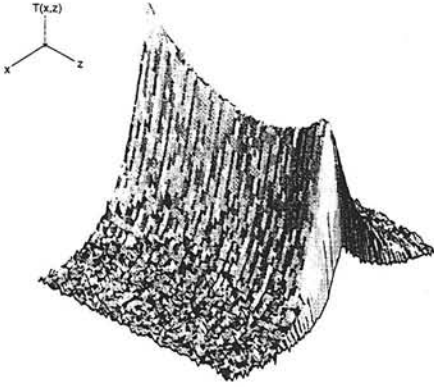


Figure 6.1: $T(x, z)$ in a laser sheet (raw).

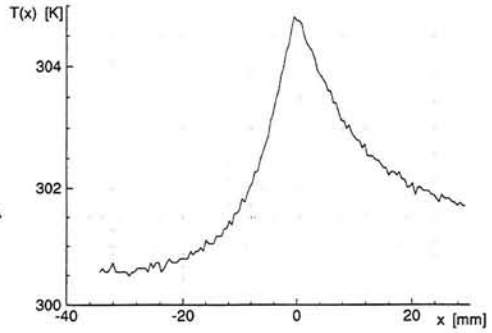


Figure 6.2: $T(x)$.

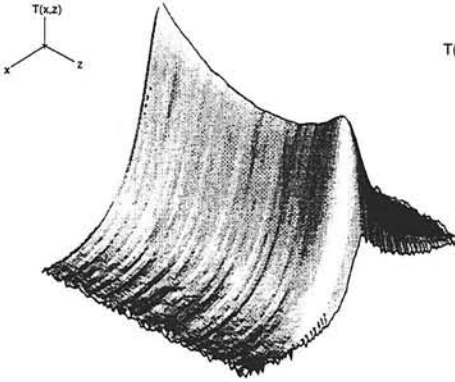


Figure 6.3: $T(x, z)$ in a laser sheet (cubic fit).

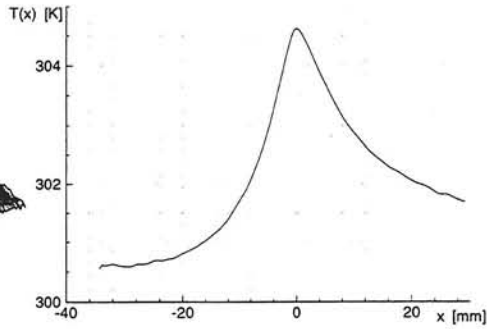


Figure 6.4: $T(x)$.

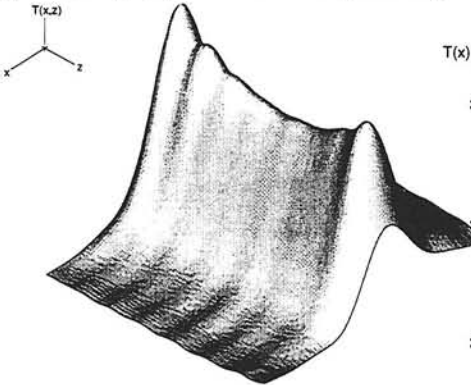


Figure 6.5: $T(x, z)$ in a laser sheet (Fourier).

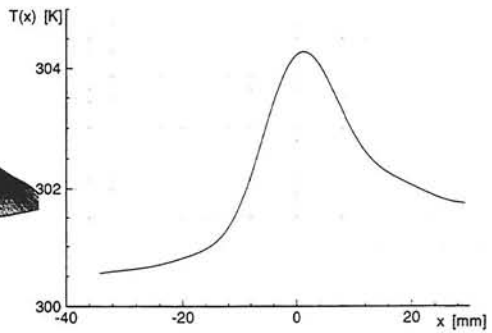


Figure 6.6: $T(x)$.

6.1.3 Data-processing program BRUT_S

The following list presents a chronological overview of the data-processing steps:

1. At the beginning the program reads in the first frame (reference frame) of the IR-camera output file.
2. To determine the position of the hot spot inside the frame the program is searching for the maximum temperature in x -direction in the reference frame. In z -direction the position with the smallest temperature gradient in z -direction is taken. The corresponding pixel-position is $i = i_{spot}$ for the x -direction and $k = k_{spot}$ for the z -direction.

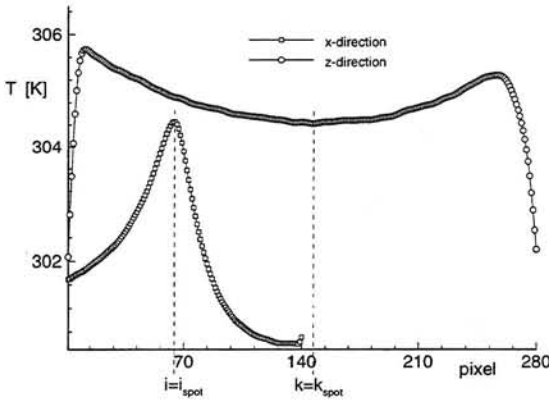


Figure 6.7: Hot spot position in a frame.

3. In the following step the temperature in z -direction for all k pixels with $i = i_{spot}$ are read and averaged with the pixels $k - 4$ and $k + 4$.

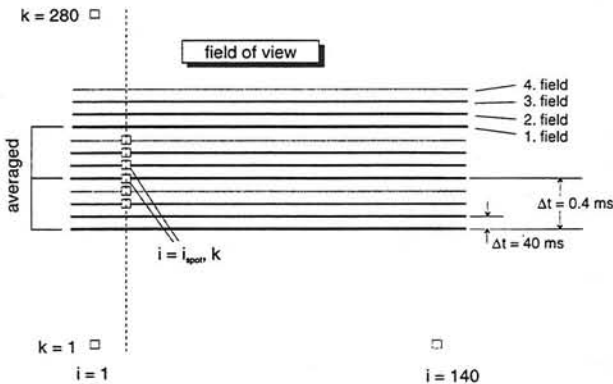


Figure 6.8: Pixel in one camera frame.

4. Due to the serial scanning of the pixels and thus due to the time shift between the pixels in the field of view of the camera, it is possible to determine the laser turn off time (LTO) with the help of the temperature in z -direction. First these temperatures are subtracted from the corresponding temperature of the same pixel of the reference frame. This is necessary since $T(z)$ is not 100% constant due to variations in the irradiated energy. The temperature differences $\Delta T = T_{i_{spot},k}^{ref} - T_{i_{spot},k}$ are approximately zero until the laser is turned out. Since the generation time of the scanned pixels is known, the time at which the first pixel is found with a ΔT that is above a certain criterion defines the laser turn off time.

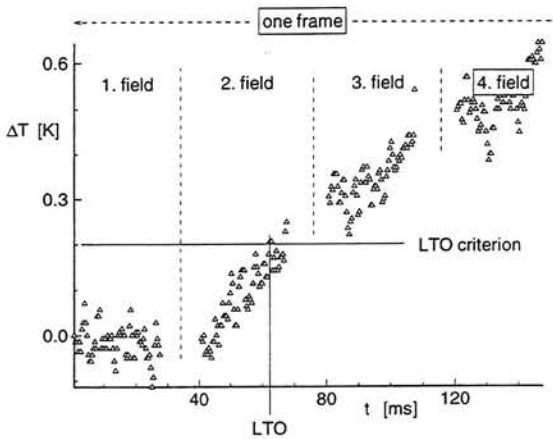


Figure 6.9: ΔT in time.

5. After the determination of the LTO the temperatures in x -direction are read. Since the camera operates in a 4:1 interlace mode one $T(x)$ distribution per field can be used instead of one per frame. These are the pixel lines for $k = k_{spot}$, $k = k_{spot} - 1$, $k = k_{spot} - 2$ and $k = k_{spot} - 3$. They have nearly the same z -position in the field of view, but are scanned 40ms after each other. This short time interval between two measurements is essential to measure the rapid change of the spot temperature directly after turning off the laser.
- Like in the other steps the $T(x)$ distribution per field is averaged with 11 other lines of the same field ($k = k_{spot} - 20$, $k = k_{spot} - 16$, ... $k = k_{spot}$, ... $k = k_{spot} + 20$ for the first field (the same for the other fields)). This averaging step leads to a very good noise reduction.
6. In this step all temperatures in x -direction are averaged until the laser is turned off.
7. The program, which calculates the heat flux to the flow from the measured surface temperatures, requires one $T(x)$ distribution in the hot spot at steady state conditions.

The temperature distributions after turning off the laser must be taken at equidistant time intervals with respect to LTO. Thus an interpolation procedure has to be introduced to calculate $T(x)$ for a time step of $\Delta t = 40\text{ms}$.

Figure 6.10 shows the difference between the maximum spot temperature T_{max} for $i = i_{spot}$, $k = k_{spot}$ and the ambient temperature T_{∞} before and after the interpolation.

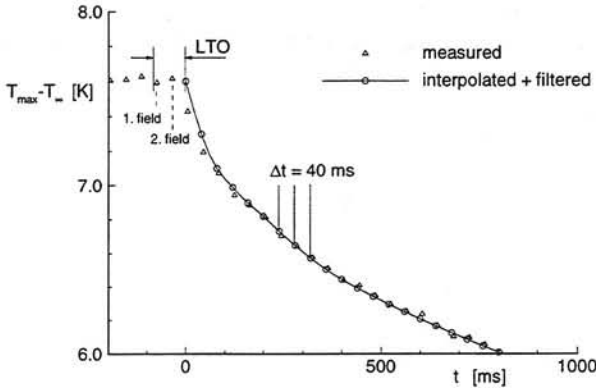


Figure 6.10: T_{max} before and after LTO.

8. Next to various averaging steps also filtering is applied to $T(x, t)$. In x -direction the CPF is used because of the strong temperature peak. With this filter the decrease of the maximum spot temperature T_{max} is less than 1%.

Since the calculation of the heat flux q_c to the flow is extremely sensitive to scatter in $T(t)$, the FFT with a low pass filter has been chosen to reduce the high frequencies of the signal noise.

9. Finally the data are stored in an output file, which is the input file of the heat flux calculation. The header consists on the one hand of physical parameters like spot position, flow velocity and ambient temperature and on the other hand of numerical parameters like the number of pixels in x -direction and the number of time steps. After the header, $T(x)$ for the steady state condition (laser on) is stored in one line. The following lines are $T(x)$ for time steps $\Delta t = 40\text{ms}$ after turning off the laser.

The following chapters will show that the accuracy of this wall-shear stress measurement technique mainly depends on the noise reduction procedure. This has two reasons.

In the first place huge errors occur in the first and second order derivatives from scattered data. In the second place the wall-shear stress τ_w is proportional to the third power of q_c (see eqn. 4.10 and eqn. 4.12). Thus errors in q_c are approximately amplified by a factor 3.

6.2 Numerical calculation of heat transfer in solids

The IR-camera measures the temperature of the surface of an object. To determine the wall-shear stress with the help of the similarity equation (see eqn. 4.12), the convective heat flux to the flow has to be calculated.

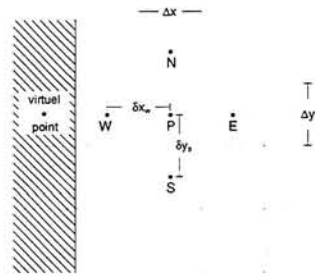
In many applications the temperature gradient inside the solid in normal direction to the surface is assumed to be zero. Numerical simulations have shown that this assumption is not fulfilled by solid materials with a low heat conductivity k or in unsteady temperature distributions (see section 7.3). Since only a few analytical solutions of the Poisson equation exists (see eqn. 4.14), the unsteady Poisson equation is solved numerically.

$$\rho c \frac{\partial T}{\partial t} = \frac{\partial}{\partial x} \left(k_x \frac{\partial T}{\partial x} \right) + \frac{\partial}{\partial y} \left(k_y \frac{\partial T}{\partial y} \right) \quad (6.1)$$

Discretizing equation 6.1 leads to following expression [9]:

$$a_P T_P + a_N T_N + a_S T_S + a_W T_W + a_E T_E = b \quad (6.2)$$

$$\begin{aligned} a_E &= -\frac{k_E \Delta y}{\delta x_E} & a_W &= -\frac{k_E \Delta y}{\delta x_E} \\ a_N &= -\frac{k_N \Delta x}{\delta y_N} & a_S &= -\frac{k_S \Delta x}{\delta y_S} \\ a_P^\circ &= \frac{\rho c \Delta x \Delta y}{\Delta t} & b &= S \Delta x \Delta y + a_P^\circ T_P^\circ \\ a_P &= -a_N - a_S - a_W - a_E + a_P^\circ \end{aligned}$$



The superscript $^\circ$ in the discretization represents the values at the centre point P for the previous time step.

The boundary conditions can be implemented with the help of the virtual point outside the computational grid. If the temperature gradient and thus the heat flux is given, this boundary condition is called a *Neumann* boundary condition. The boundary condition for a given temperature is called a *Dirichlet* boundary condition.

The following equations show the discretized equations for the different boundary conditions at the west boundary (same for the other boundaries).

Neumann boundary condition

$$(T_W - T_P) \frac{k_W}{\delta x_W} = q_W \quad (6.3)$$

$$\Rightarrow (a_W + a_P) T_P + a_N T_N + a_S T_S + a_E T_E = b - \left(\frac{\delta x_W}{k_W} q_W \right) a_W \quad (6.4)$$

$$\vec{T} \cdot [A] = \vec{b} \quad \text{with} \quad \vec{T} = \begin{pmatrix} T_1 \\ \vdots \\ T_{imax \times jmax} \end{pmatrix} \quad \vec{b} = \begin{pmatrix} b_1 \\ \vdots \\ b_{imax \times jmax} \end{pmatrix} \quad (6.8)$$

There are many different solvers for this kind of matrix system. In the present study the LU decomposition is used to solve the matrix, since it requires three times less operations than the Gauss elimination.

It is advantageous to number the grid-points in the direction of the smaller number of grid points (in this case $jmax$), because this decreases the width of the diagonal in the matrix and thus the number of operations in the LU decomposition. As the computational grid is fixed in all time steps the computation of the matrix $[A]$ and the LU decomposition need to be performed only once. In contrast to $[A]$ the right hand side vector \vec{b} changes for each time step, because it consists of the temperatures of the previous time step T_p^o and the boundary conditions.

To solve the Poisson equation for multi-layer solids, like in this investigation (poly carbonate = lower layer + PVC foil = upper layer), the corresponding heat conductivities have to be substituted into the coefficient matrix $[A]$.

The calculation of the temperature inside the solid runs through the following procedure:

1. The temperatures for the steady state conditions (laser on) are read from the BRUT.S output file.
2. Keeping these Dirichlet boundary conditions on the upper surface constant the program calculates the temperatures inside the solid, until the variation of the temperature is of the order of 10^{-10} . The convergence of the temperature has a strong influence on the accuracy of the calculation for the heat flux q_c .
3. The time step for the following calculation is set to 0.4 ms (= time step of the IR-camera measurement).
4. For each following time step the surface temperature is read and prescribed as Dirichlet boundary condition.
5. Finally the $q_c(x)$ is calculated from the temperature gradient in y -direction at the surface of the solid.

To evaluate the local wall-shear stress from the heat transfer to the flow and from the measured temperatures further details have to be given. These are presented in section 6.3.

6.3 Wall-shear stress calculation

To calculate the local wall-shear stress similarity solution 4.12 is transformed to

$$C \left(\frac{\tau_w L^2}{\mu a} \right)^{1/3} = \left(\frac{q_c L}{k \Delta T} \right) \left[\Theta_{step}(0) \xi^{-1/3} + \int_0^\xi (\xi - \xi_0)^{-1/3} \frac{d\Theta_{step}}{d\xi_0} d\xi_0 \right]^{-1} \quad (6.9)$$

$$\tau_w = \frac{\left(\frac{L}{k \Delta T} \right)^3}{\left(\frac{C^3 L^2}{\mu a} \right)} \left[\frac{q_c}{\Theta_{step}(0) \xi^{-1/3} + \int_0^\xi (\xi - \xi_0)^{-1/3} \frac{d\Theta_{step}}{d\xi_0} d\xi_0} d\xi_0 \right]^3 \quad (6.10)$$

in which q_c is the integrated heat transfer over the hot spot.

In this investigation a simulation of the wall-shear stress measurement has been made. For this simulation the numerical solution of the Poisson equation is coupled to a numerical solution of the boundary layer equations, which calculates the temperatures and the velocities in the fluid. With the help of this simulation the wall-shear stress can be determined either by the given velocity profile, calculated from the solution of the boundary layer equations, or by equation 6.10. In the following the dimensionless wall-shear stress c_f (see eqn. 2.7) will be compared. To distinguish the two different calculations, c_f calculated with the similarity equation 6.10 is called $c_{f\ sim}$ and c_f calculated with the boundary layer equations is called $c_{f\ bl}$.

As already described in section 4.2 equation 6.10 has been derived under the assumption that τ_w is constant along the hot spot. To validate this assumption the relative error $\Delta c_f = (c_{f\ sim} - c_{f\ bl})/c_{f\ bl}$ in [%] has been calculated for a simulated experiment, in which the laser continuously heats up the solid until steady state conditions are reached. Figure 6.12 and 6.13 presents Δc_f depending on the spot width w_{spot} for different x -positions and different free stream velocities U_e . (w_{spot} is defined as the width between points having a temperature of 50% of the maximum spot temperature).

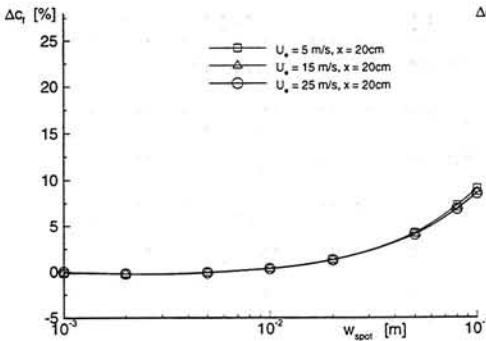


Figure 6.12: $\Delta c_f(w_{spot})$ for different U_e .

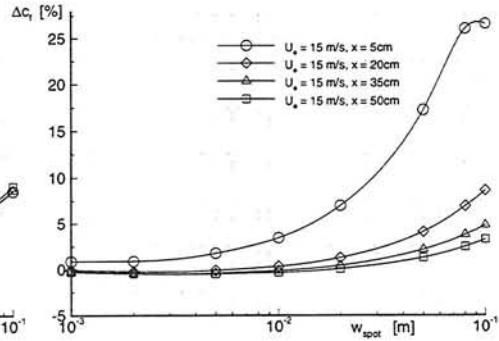


Figure 6.13: $\Delta c_f(w_{spot})$ for different x .

The simulated experiment shows that the error Δc_f is small for $w_{spot} \leq 1 \text{ cm}$. Since w_{spot} is about 5–6 mm in the real experiment, equation 6.10 is sufficiently accurate to calculate the local wall-shear stress. The increasing error for smaller x -positions is caused by the boundary of the calculation domain for $x = 0.01 \text{ m}$. If the hot spot reaches the boundary, a part of the hot spot is cut. This decreases the value of the integration in equation 6.10 and thus increases $c_{f \text{ sim}}$.

By using equation 6.10 the local wall-shear stress can be determined with the measured temperatures for any x -position with $\Theta_{step} \neq 0$ and for any time level. It has been investigated where inside the hot spot and at which time after turning off the laser the wall-shear stress has to be calculated.

To determine the position x_{cf} and the time t_{cf} of the wall-shear stress calculation, the influence of these two independent variables x and t on the relative error has been investigated. Figure 6.14 presents $\Delta c_f(x)$ with $x \geq x_{spot}$ for each time step in one measurement.

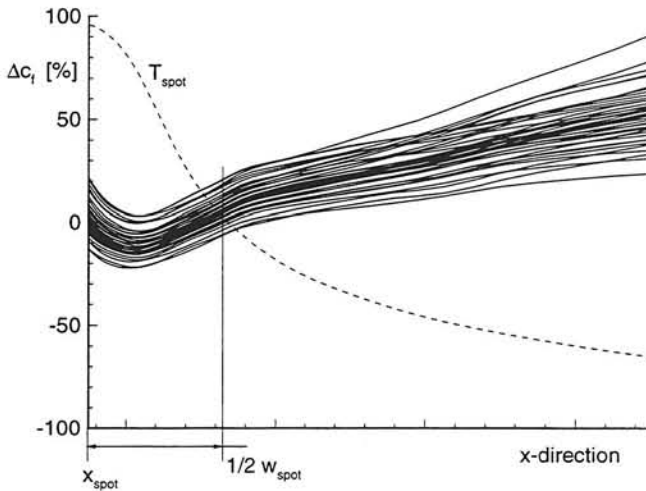


Figure 6.14: $\Delta c_f(x)$ at different time steps.

As can be seen in figure 6.14 the position $x_{cf} = x_{spot} + 1/2 w_{spot}$ approximately leads to the smallest Δc_f . This has three reasons. First 90% of the total heat flux to the flow is transferred up to this position. Thus most information about the boundary conditions is given in this area. Second a position x_{cf} further downstream would contradict the assumption of local heating and would increase the error caused by the use of the similarity equation (see figure 6.12 and 6.13). Third the signal to noise ratio is decreasing with decreasing $T_w - T_e$ which leads to a larger scatter in the calculation of τ_w . This can be seen from the divergence of the

lines for increasing x in figure 6.14.

Figure 6.15 shows the variation of $\Delta c_f(t)$ with $t \geq LTO$.

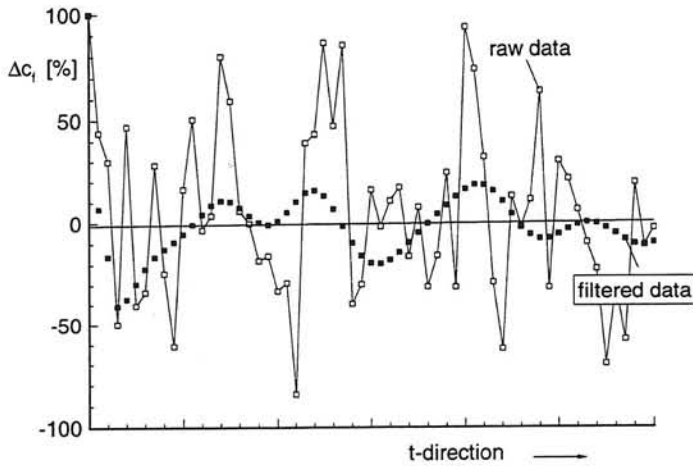


Figure 6.15: $\Delta c_f(t)$ at $x_{cf} = x_{spot} + 1/2w_{spot}$.

Figure 6.15 shows distinctly the reduction of the scatter in the calculated wall-shear stress, due to the filtering of the temperature data, described in section 6.1. But it is even more important that the wall-shear stress can be averaged in time as long as the flow conditions are steady. The constant c_f can be approximated by the horizontal solid line in figure 6.15, which represents a linear fit of the filtered data. The averaging of the wall-shear stress is essential to obtain sufficiently accurate results.

Chapter 7

Results

Since this investigation deals with experimental as well as numerical aspects, this chapter is divided in an experimental part and a numerical part. In the beginning some details on the setup of the test plate and the essential preliminary experiments are given. Before presenting the results of the wall-shear stress measurements, the numerical calculations are inserted. Here the influence of the thermal properties of the solid and the different boundary conditions on the temperatures inside the solid and the fluid can be found.

7.1 Test plate

As already mentioned, the choice of the solid material has a large influence on the size of the hot spot and thus on its maximum temperature and on the time scale of the temperature decay.

The first configuration consists of 0.9 mm aluminium, which has a black dull colour coating on the upper surface (IR-thermographical reasons) and is glued on a 38.5 mm PVC base. On the one hand the aluminium has been chosen to increase the size of the hot spot by tangential heat conduction, which increases the number of camera pixels in the hot spot. On the other hand aluminium decreases the maximum temperature in the centre. Large temperature differences between wall temperature and ambient temperature may vary the density of the air and contradict the mathematical assumption of constant flow properties. The 16 mm holes through the PVC base are used to insert thermocouples onto the backside of the aluminium strip. The aluminium nose of the test plate has a triangular cross section with a rounded tip of 4 mm radius.

Figure 7.1 sketches the first configuration of the test plate and figure 7.2 gives a cross-section of the measurement strip.

1. Plate configuration

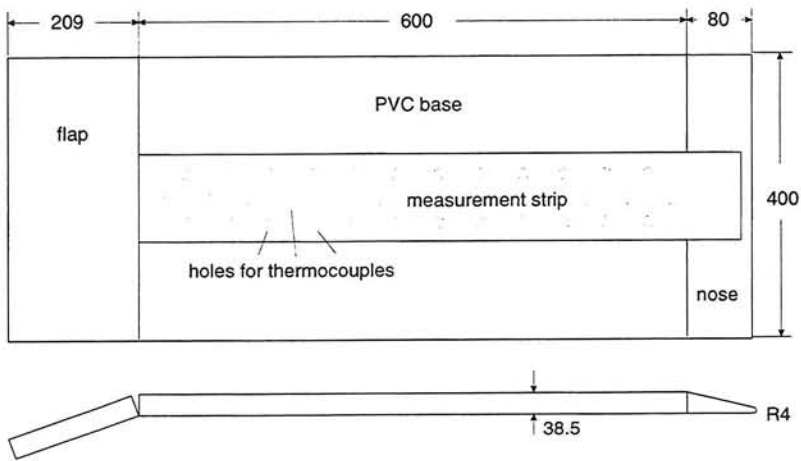


Figure 7.1: Set-up of the test plate.

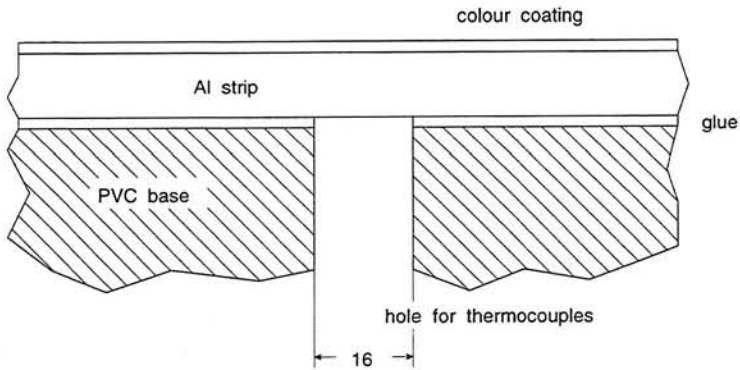


Figure 7.2: Cross-section of the measurement strip (first configuration).

For this first configuration of coating, aluminium strip, glue and PVC-base a series of experiment has been performed to check whether its thermal properties can be applied to hot spot quantitative IR-thermography.

7.2 Preliminary experiments

Before performing measurements under flow conditions, it has to be checked whether the maximum temperature T_{max} in the hot spot for continuous heating is constant along the measurement area on the test plate under no-flow conditions.

Experiment 1.1

The laser is positioned at an arbitrary x position on the measurement strip and is turned on at $t = 0$. While the laser is continuously heating, the increase of the maximum temperature T_{max} in the hot spot from the ambient temperature to a final asymptotic value is measured by the IR-camera.

Experiment 1.2

After the laser has led to steady conditions, the laser is turned off and the temperature decay is monitored.

The results of experiment 1.1 and 1.2 are given in figure 7.3 and 7.4.

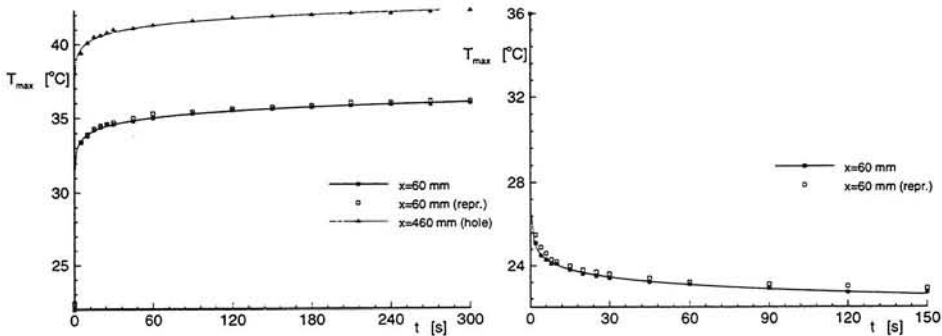


Figure 7.3: Increase of T_{max} in a laser spot. Figure 7.4: T_{max} decay (laser turned off).

Results

At $x = 60$ mm experiment 1.1 has been performed two times to check whether the results can be reproduced. Neglecting the small temperature difference of about $0.2^\circ C$, which is caused by an increase of the ambient temperature between these two measurements, the results are equal. Thus the irradiated energy of the laser can be assumed to be constant in time.

120 seconds turns out to be a sufficiently long time scale to achieve quasi-steady conditions. Of course the characteristic timescale to reach steady state conditions is smaller than 120 s, if there is the flow along the plate.

It has to be noted that the temperature is influenced by the holes on the backside of the aluminium strip. Obviously, the lower heat conductivity of air ($k_{air} = 0.026 W/mK$) compared with heat conductivity of PVC ($k_{PVC} = 0.15 W/mK$) leads to smaller heat loss on the backside of the Al strip and thus to a higher maximum temperature.

Experiment 1.3

To determine the dependence of the maximum temperature (120s after turning on the laser) on the x position, measurements have been performed sequentially on different positions with an intermediate distance of 20 mm. To avoid influences between two measurement points the test plate has cooled down to ambient temperature after each measurement. If the temperature increase is caused by the presence of the thermocouple holes, the position of the holes should be visible in the measured temperature distribution.

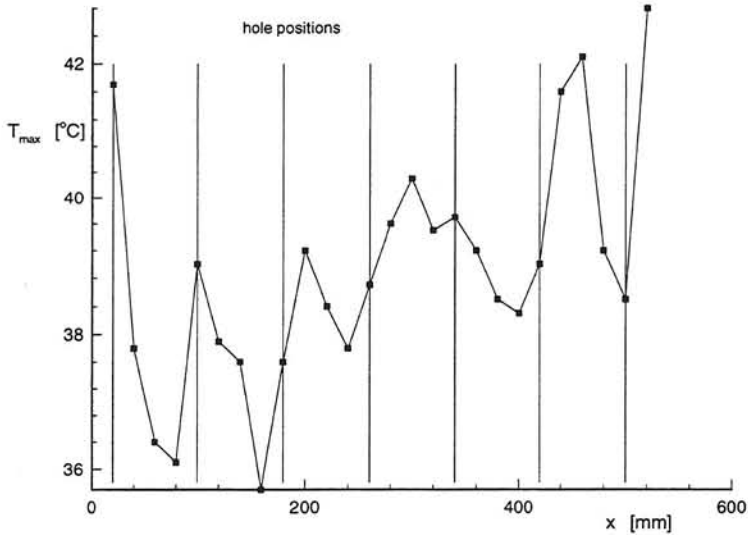


Figure 7.5: Influence of the PVC-base on T_{max} .

Results

Figure 7.5 shows clearly that the local temperature maxima do not only occur at the positions of the holes. As there are significant temperature variations in areas where the material should be homogeneous (between the holes), there must be other effects that influence the temperature measurements.

Experiment 1.4

In this experiment the maximum temperatures around a thermocouple hole are measured with a finer resolution ($\Delta x = 1 \text{ mm}$). Since T_{max} is influenced by air in the holes on the backside, a cylinder of 16 mm diameter has been inserted in the hole in a second measurement series to simulate a full homogeneous PVC-base.

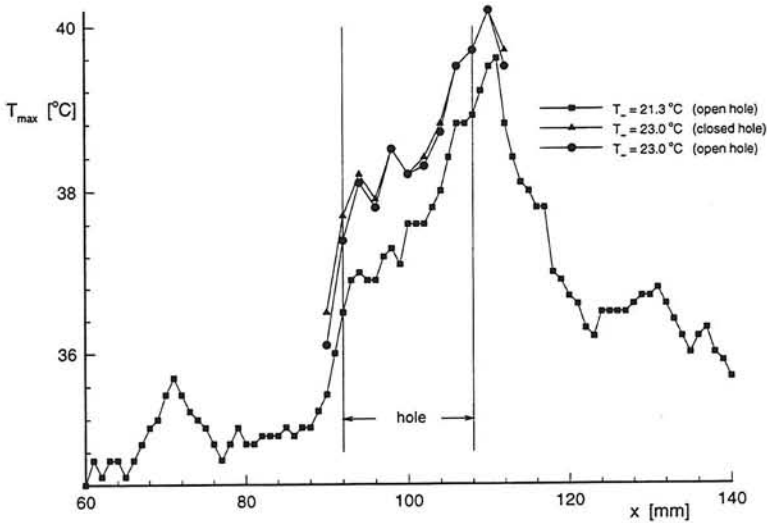


Figure 7.6: Influence of the thermocouple hole on T_{max} .

Results

Figure 7.6 shows that the temperature increases along a hole and next to the hole. After this experiment the aluminium strip has been removed from the PVC-base and it was found that at $x = 110 \text{ mm}$ the strip was not homogeneously glued and thus a thin air bubble has been formed in the glue layer, which leads to higher temperatures. Additionally an increasing thickness of the glue influences the temperature T_{max} ($x = 70 \text{ mm}$).

Comparing the lines in figure 7.6 shows that the temperature distribution remains unchanged with or without inserting the PVC cylinder to close the hole. This result underlines the influence of the thin air layers underneath the aluminium strip. Since the cylinder has just been pressed in the hole lightly without glue, an air layer between the cylinder and the strip can not be prevented.

The temperature difference between the curve with the squares and the other curves is caused by an increase of the ambient temperature.

It is obvious that an absolute temperature variation of $\Delta T = 7^\circ\text{C}$ is not tolerable and new material configurations with constant properties in x -direction have to be tested.

Experiment 1.5

As a first test for a single material configuration a 0.2 mm Capton (400 × 20mm) tape has been spanned between two metal bars and coated with black dull colour. Since the metal bars have an influence on the heat transfer, no temperatures have been measured close to the bars. Due to the air around the tape, constant thermal boundary conditions can be assumed. As for experiment 1.4 and 1.5 the maximum steady temperature is measured for different x positions on the tape.

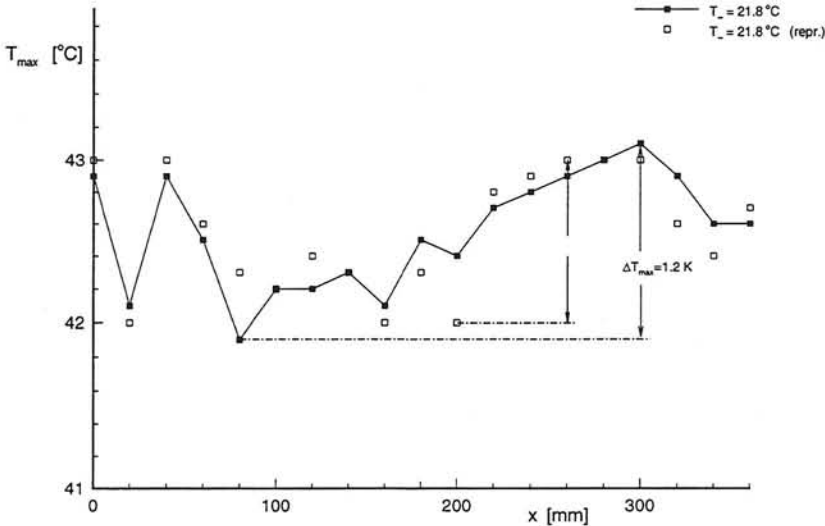


Figure 7.7: T_{max} on a Capton tape.

Results

In this experiment the absolute temperature variation ΔT_{max} has been reduced by a factor six, which is mainly evoked by the constant thermal boundary conditions on the backside, because of the absence of any intermediate air bubbles or glue. Due to the low thermal conductivity of Capton the laser spot is very small and thus a high maximum temperature T_{max} is generated, because less heat is transported within the Capton tape by heat conduction. Even with a little irradiated power, T_{max} can easily exceed the melting temperature of Capton and a hole is burned in it.

Since the air layer on the backside for insulation purposes leads to a decreasing variation of ΔT_{max} , a stiff material has to be found, which can be spanned in the PVC-base to get a resting air layer beneath it and to guarantee a flat surface on the flow side.

Experiment 1.6

In this experiment the Capton tape has been replaced by a 0.1 mm stainless steel foil with a colour coating. Stainless steel combines stiffness with a relatively low heat conductivity compared with high heat conductivity of other metals ($k_{Al} = 204 \text{ W/mK}$, $k_{steel} = 14 \text{ W/mK}$). As already mentioned a low heat conductivity means less irradiated energy to generate a certain T_{max} . In this experiment a laser sheet perpendicular to the later flow direction, generated by an oscillating mirror, is compared with a laser spot. Due to the larger irradiated area for a sheet than for a spot, the irradiated energy density is reduced, which leads to a lower temperature. Thus the maximum sheet width decreases with increasing conductivity of the surface material to generate the same T_{max} .

Basically the laser sheet is used to simplify the heat transfer phenomena from three-dimensional to two-dimensional, because for a sheet with constant irradiated power along the sheet the temperature perpendicular to the flow is constant and no heat is transported in this direction.

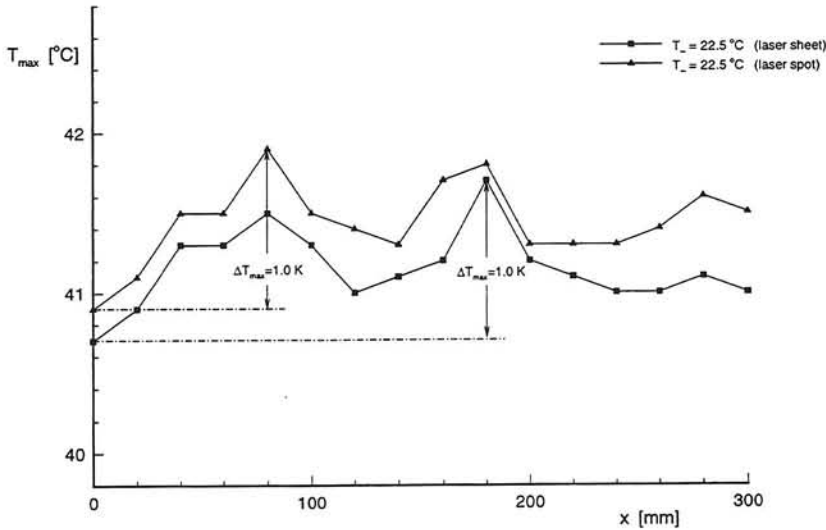


Figure 7.8: T_{max} on a stainless steel foil (0.1 mm).

Results

Compared with experiment 1.5 the absolute temperature variation ΔT_{max} has been further improved. Over wide areas ΔT_{max} is smaller than $0.4 \text{ }^\circ\text{C}$.

Since the test with stainless steel has been rather successful, it seems to be advantageous to replace the aluminium strip by a stainless steel strip and to provide the resting air layer on the backside of the strip.

2. Plate configuration

To achieve a non-moving air sub-layer beneath the stainless steel foil a ditch of 5 mm depth has been milled starting at 15 mm behind the nose up to 10 mm before the end of PVC-base. The foil has been fixed by two-sided adhesive tape. The surface has been again coated with black dull paint.

Figure 7.9 sketches the cross-section of the test plate perpendicular to the direction of the flow.

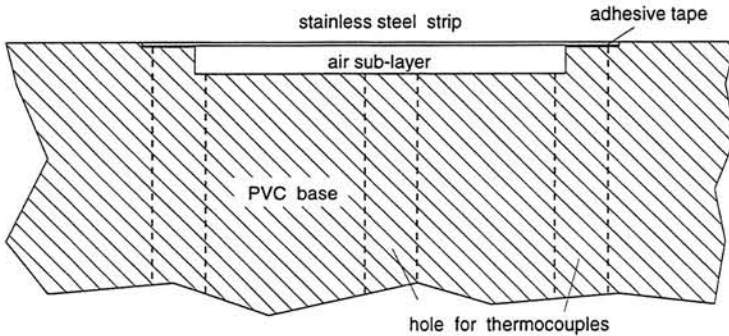


Figure 7.9: Cross-section of the measurement strip (second configuration).

While inserting the steel foil into the base, the foil is stretched to obtain a flat surface. But in the area of the thermocouple holes, where the foil can not be glued, tensions in the steel are generated, which lead to a tiny wave in the surface at this position. Since the amplitude of the waves are small, their influence is assumed to be negligible.

As can be seen in figure 7.8 there are still variations of the maximum steady temperature. After eliminating the influence of non-constant thermal boundary conditions, these variations may probably be caused by:

- o tolerances in the thickness of the steel foil
- o tolerances in the thickness of the colour coating
- o variation of the irradiated power of the laser due to scratches or dirt on the Perspex wall of the wind tunnel
- o influence of irregular free convection

To check if the temperature variations are caused by the test-plate itself or by variations of the irradiated power of the laser, the following experiment has been performed.

Experiment 1.7

The maximum steady temperature T_{max} has been measured for different positions in x -direction. In a second measurement series, the plate has been moved 50 mm down-stream. The origin of the coordinate system in this experiment is fixed at the wind tunnel wall and not at the nose of the plate as usual.

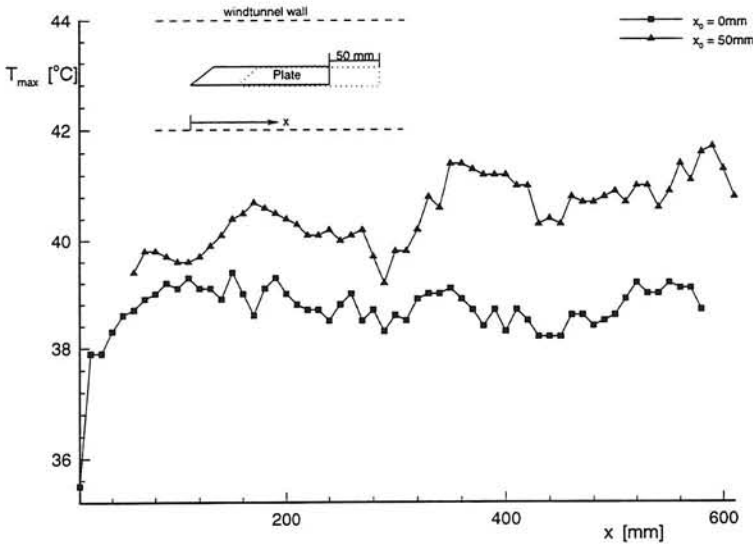


Figure 7.10: T_{max} on the test plate (second configuration) for different x -positions.

Results

Comparing the two temperature distributions in figure 7.10, no correlation between them seems to exist. If the variations would have been caused by the perspex wall, the two curves should coincide with a probably constant temperature difference due to an increasing ambient temperature T_{∞} . Otherwise the two lines should have a shift in x -direction of 50 mm, which would prove that the variations are generated on the plate.

Since this experiment does not deliver new information about the origin of the temperature variations, more attention has to be paid to the influence of tolerances in the thickness of the colour coating (tolerances in the thickness of the steel plate can be neglected). To minimize scratches and dirt on the perspex wall, it has been cleaned and polished before each experiment.

Experiment 1.8

To determine the influence of different thicknesses of the colour coating the stainless steel strip has been coated with one or two layers of paint. Additionally parts of the coating have been roughed with sandpaper to check whether scratches on the surface lead to variations in the maximum steady temperature T_{max} .

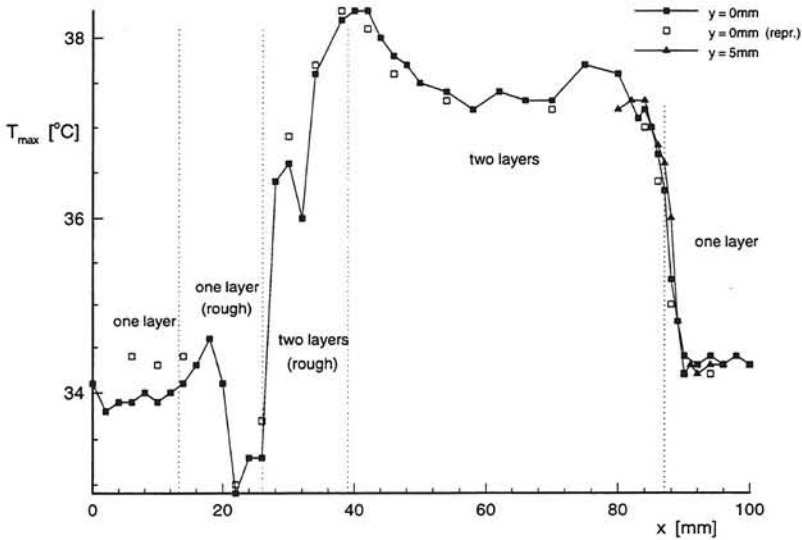


Figure 7.11: T_{max} on the test plate for different coatings.

Results

Figure 7.11 shows a clear dependence of T_{max} on the thickness of the coating. The temperature difference between one and two layers of paint is more than $4^{\circ}C$. By coating the stainless steel with a spray, a thickness of 0.013 mm with an uncertainty of $\pm 0.003\text{ mm}$ can be achieved. This 20% tolerance of the thickness may lead to a ΔT of one degree Celsius. Comparing numerical calculations proves that tolerances are more critical when the coating becomes thinner.

To determine whether the temperature variation of one degree Celsius is negligibly small compared to the ΔT caused by the boundary-layer, a few experiments have been performed under flow conditions to estimate the variation of T_{max} along the plate.

Experiment 1.9

Like in experiment 1.7, T_{max} has been measured for different x -positions, but with a flow of $U_{\infty} = 10\text{ m/s}$ along the plate.

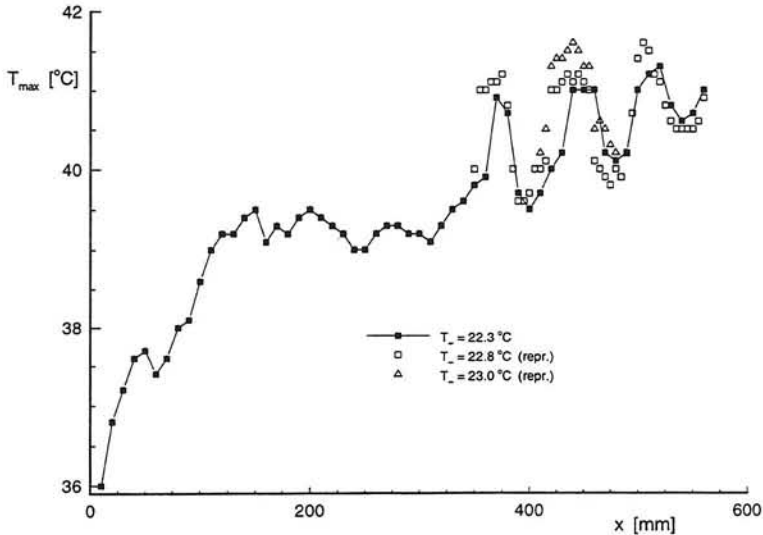


Figure 7.12: T_{max} on the test plate with flow.

Results

According to the theory the temperature will increase with growing thickness of the thermal boundary layer. However from $x = 360\text{ mm}$ a periodic increase and decrease in T_{max} occurs. Since the wavelength of this periodic pattern is 80 mm , which is equivalent to the distance of the holes of the thermocouples, this leads to the conclusion that this local temperature maxima are caused by the holes in which the steel strip is not glued to the PVC base.

The influence of the hole and the tolerances in the thickness of the coating require another modification of the measurement strip.

3. Plate modification

First, to get a thicker coating with a more constant thickness and good IR-thermographical properties, the colour is replaced by a black self-adhesive PVC tape of 0.12 mm thickness. Second, the holes are filled with PVC-cylinders, which are accurately polished. With the help of these modifications a smooth surface without any waves can be achieved. Unfortunately there are still a few air bubbles between the tape and the steel strip, but they can be easily detected by the human eye or in the thermogram.

Experiment 1.10

As a final test this new test plate has been tested again in the absence of any flow.

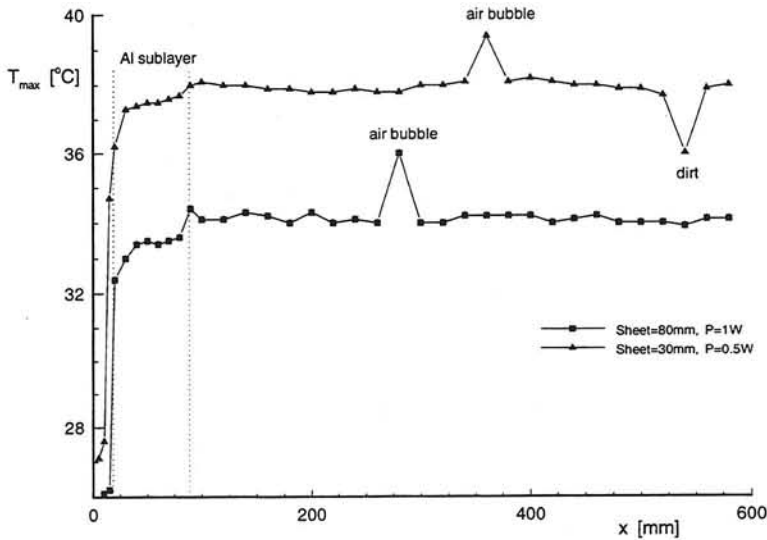


Figure 7.13: T_{max} on the test plate (3. configuration) for two different widths of the laser sheets.

Results

The last test plate modifications generate a rather constant temperature along the whole plate, if peaks caused by air bubbles and dirt on the perspex wall are neglected. The decrease of T_{max} in the area of the aluminium nose (between 15 and 90 mm) is caused by an insufficient insulation of the steel strip from the nose. The curvature of the nose produces the rapid temperature decrease between 0 and 15 mm (see section 5.3.4).

Additionally figure 7.13 proves that a higher temperature can be achieved with less irradiated power for a smaller laser sheet.

Since the temperature variations in the absence of any flow are finally rather small, this material configuration for the test plate is tested for different free stream velocities U_{∞} . The results are presented in the following subsection.

Experiment 2.1

In this experiment T_{max} is measured for different x -positions and for four different free stream velocities U_∞ . First the different points from the nose to the end of the test plate have been measured for constant velocity. After adjusting another U_∞ , the temperature has been measured at the same x -positions again.

Since T_{max} depends on the ambient temperature, this influence is eliminated by presenting $\Delta T = T_{max} - T_\infty$ instead of T_{max} .

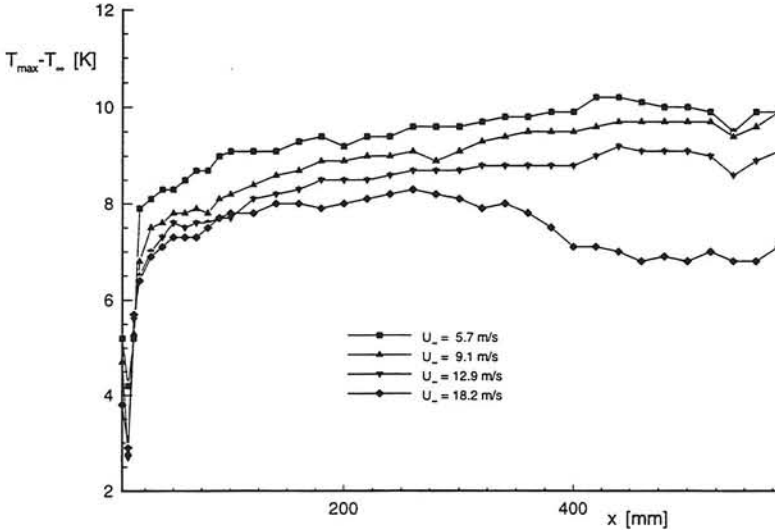


Figure 7.14: T_{max} for different x -positions.

Results

Like in experiment 1.9, the influence of the growing thickness of the thermal boundary layer δ_T on T_{max} can be seen. For larger δ_T the Nusselt number Nu decreases, which leads to a lower heat transfer to the flow and thus to a larger temperature difference $T_{max} - T_\infty$. Since Nu increases with increasing free stream velocity U_∞ , ΔT decreases with increasing U_∞ .

The decrease of ΔT between $x = 250$ mm and $x = 450$ mm in the temperature measurement for $U_\infty = 18.2$ m/s is caused by the flow transition from laminar to turbulent, which leads to an increase of Nu .

Experiment 2.2

In contrast to the previous experiment, now the free stream velocity U_∞ is varied from 2.8 m/s to 21.6 m/s at a certain x -position before the laser and the IR-camera are traversed to another measurement position.

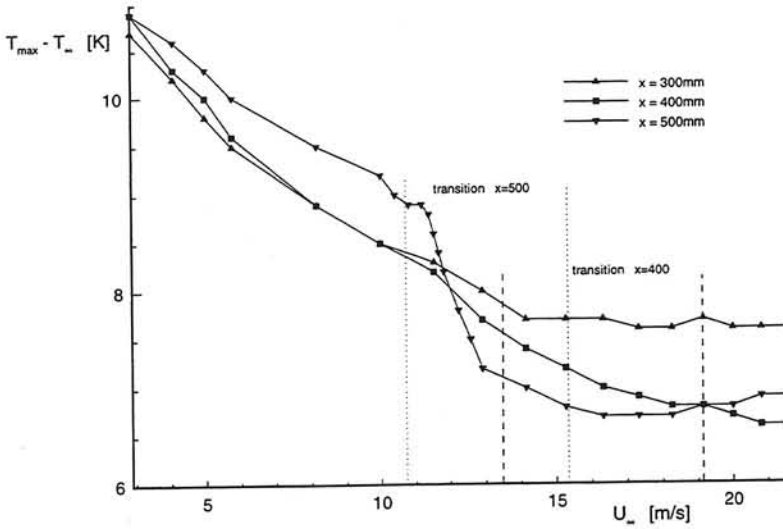
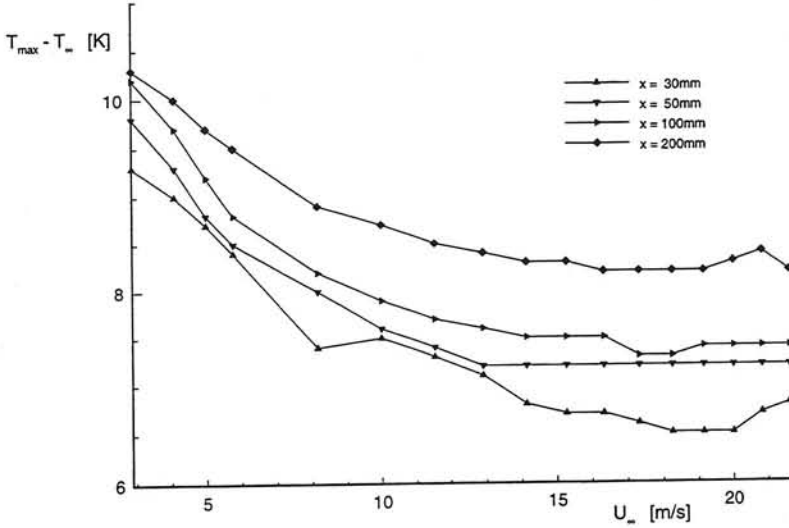


Figure 7.15: T_{max} for different velocities U_∞ .

The theoretical relations between the quantities x , U_∞ , Nu and ΔT generally correspond to the results presented in figure 7.14. However two other phenomena must be noted.

First the deviations from the smoothly declining temperature distribution at $x = 30 \text{ mm}$ are caused by local disturbances of the flow at the transition from the nose to the stainless steel strip, where a small step could not be prevented. Second the transition from laminar to turbulent is visible rather well at $x = 500 \text{ mm}$. The transition causes a rapid decrease in $\Delta T = T_{max} - T_\infty$ between $U_\infty = 10.7 \text{ m/s}$ and $U_\infty = 15.3 \text{ m/s}$, which is equal to the Reynolds number $Re = 3.5 \times 10^5$ and $Re = 5.0 \times 10^5$ for $x = 500 \text{ mm}$. These are the margins of the critical Reynolds number given in literature, where transition usually occurs in a flow along a flat plate.

For $x = 400 \text{ mm}$ transition should occur between $U_\infty = 13.4 \text{ m/s}$ and $U_\infty = 19.2 \text{ m/s}$. The fact that ΔT is lower for $x = 400 \text{ mm}$ than for $x = 300 \text{ mm}$ proves that the flow is turbulent in this velocity area. Unfortunately the transition can not be indicated by a rapid decrease of $\Delta T = T_{max}$.

In general the detection of the transition area is rather difficult since temperature gradients in x -direction are smeared out by heat conduction in the stainless steel strip. This implies that the transition seems to start at a smaller Reynolds number than it actually does.

7.2.1 Temperature decay

In the unsteady measurement technique the temperature decay of the hot spot after turning off the laser has been monitored. Typical temperature distributions in x -direction for different timesteps are given in figure 7.16 and 7.17.

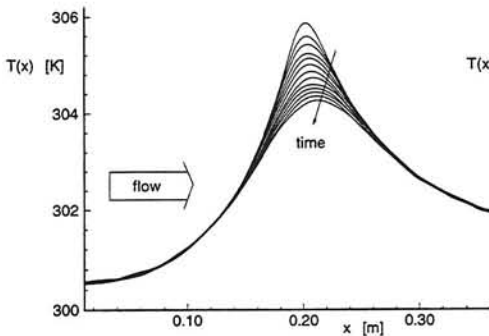


Figure 7.16: $T(x)$ for $U_\infty = 5 \text{ m/s}$.

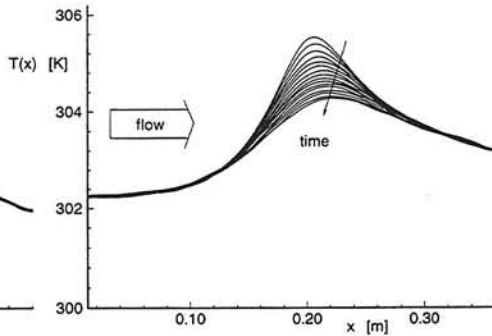


Figure 7.17: $T(x)$ for $U_\infty = 25 \text{ m/s}$.

As already mentioned in the previous section the ambient temperature T_∞ has to be taken into account. Figure 7.17 shows for the upwind position $x = 0$ a higher temperature than in figure 7.16. This difference is caused by the huge heat production of the propeller of the

wind tunnel at high velocities, which leads to an increase of the fluid temperature. Even more important for the calculation of the wall-shear stress is the fact that the hot spot does not fit in the field of view of the camera. To reduce the hot spot size a surface material with a lower heat conductivity than stainless steel has been chosen. On the other hand the diameter of the laser beam has been expanded to guarantee a sufficient number of pixels in the area of T_{max} . For the following experiments the stainless steel is replaced by a 1 mm polycarbonate plate with a tolerance in the thickness of $\pm 5\%$. Like the stainless steel strip the polycarbonate has been covered with the black dull PVC foil. Since the hot spot is generated by a laser sheet in y -direction and the measured temperatures are averaged in the same direction (see section 6.1.3) the influence of air bubbles underneath the PVC foil can be minimized.

A second advantage of the use of the polycarbonate is that thickness variations of the upper layer (paint or foil) have only a small influence on the shape of the hot spot, due to the smaller differences in heat conductivity and heat capacity between the two solid layers. This can be verified with the help of a numerical simulation (see section 7.3).

7.3 Numerical calculations

In this investigation, next to experiments, also numerical simulations of the experiment were performed. With the help of these calculations the optimum solid material, which matches the assumption of local heating and the capabilities of the IR-camera, can be determined. The influence of the different boundary conditions in the steady and the unsteady method on the wall-shear stress has also been calculated.

A typical result of a numerical simulation of a flow along a flat plate is presented in figure 7.18. The dots represents the boundary layer thickness δ_U calculated at each x -grid point.

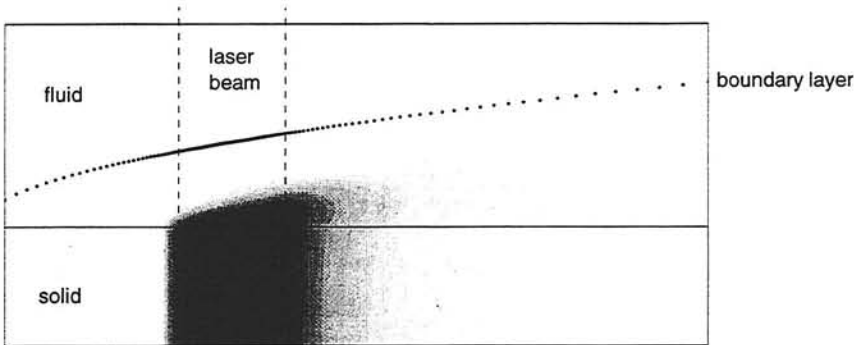


Figure 7.18: Numerical calculation of the temperature in the fluid and in the solid (black=warm, white=cold).

The calculation grid is built up with 200 points in x -direction, 100 points in y -direction in the fluid and 40 points in y -direction in the solid. The grid is refined at the position of the hot spot and at the interface between fluid and solid.

7.3.1 Thermal properties of the solid

The thermal properties of the solid material determine the characteristics of the hot spot, like the spot width w_{spot} , the time scale of the temperature decay t_{spot} and the maximum spot temperature T_{max} . As already mentioned w_{spot} is defined as the distance between the two x -positions where the temperature equals 50% of T_{max} and t_{spot} defines the time at which T_{max} has decreased to 50% of the maximum temperature at steady state conditions.

Since the present measurement technique uses two different solid material layers (measurement strip + coating for IR-thermography), the influence of the specific heat capacity c , the density ρ , the thickness h and the thermal conductivity k of the two layers on w_{spot} , t_{spot} and T_{max} has to be investigated.

In these experiments standard available metals and plastics have been used. Thus the ρ and

c of the solid material are prescribed and only the thicknesses can be varied. To get an impression of the relation between the thickness of the two layers h and the two characteristics the following figures present w_{spot} for constant irradiated power of the laser and t_{spot} after turning off the laser. The experiment has been numerically simulated for a Reynolds number of 10^5 , which is based on the length of the plate, and a laser diameter of 2 mm. For the solids standard available thicknesses have been chosen.

Figures 7.19 and 7.20 present the influence of the thicknesses of the lower stainless steel layer and of the upper PVC layer on w_{spot} and t_{spot} . The solid line represents the simulation for a varying thickness of the lower layer with a constant thickness of the upper layer and the dashed line for a varying thickness of the upper with a constant thickness of the lower layer.

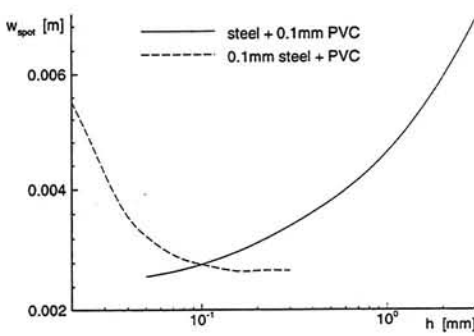


Figure 7.19: w_{spot} for different h .

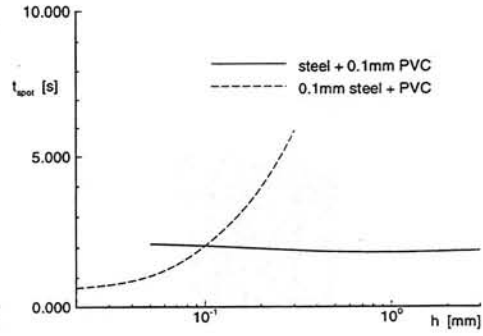


Figure 7.20: t_{spot} for different h .

In another simulation the stainless steel layer is replaced by a polycarbonate layer.

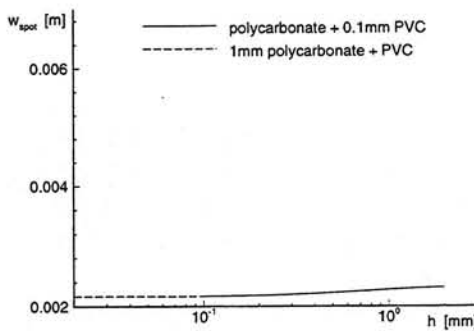


Figure 7.21: w_{spot} for different h .

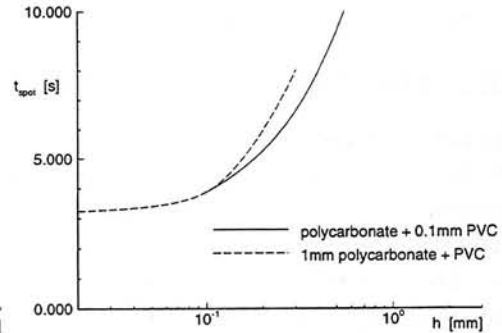


Figure 7.22: t_{spot} for different h .

The unsteady heat transfer in the solid depends on heat conduction, which is determined by

k and h , and heat capacity of the material, which is determined by ρ , c and h . Table 7.1 presents the thermal properties of stainless steel, PVC and polycarbonate.

Table 7.1: Thermal properties of the solids

solid	ρ	$\frac{kg}{m^3}$	c	$\frac{J}{kg K}$	k	$\frac{W}{m K}$
stainless steel	7900.0		510.0		14.00	
polycarbonate	1200.0		1060.0		0.20	
PVC	1600.0		1200.0		0.16	

For the configuration stainless steel + PVC it can be seen in figure 7.19, that the spot size w_{spot} is mainly influenced by heat conduction. Due to the high conductivity of stainless steel, the tangential heat flux can be significantly increased by increasing the thickness of the steel layer, which increases the size of the hot spot. The time t_{spot} depends on the heat capacity of the solid. Since c_{PVC} is larger than c_{steel} , t_{spot} depends much more on a variation of h_{PVC} than of h_{steel} . In experiment 1.8, presented in section 7.2, an increase of the maximum spot temperature T_{max} due to an increasing thickness of the colour coating (similar thermal properties as PVC) has been detected. The increase of T_{max} is caused by a decrease of w_{spot} . This relation between w_{spot} and h_{PVC} can also be found in figure 7.19.

In case of the polycarbonate + PVC configuration w_{spot} is rather independent of the thickness of polycarbonate or the thickness of PVC. In contrast to w_{spot} the spot size t_{spot} strongly depends on the thickness of the polycarbonate (see figure 7.22). Thus it is very important for the calculation of the heat transfer to the flow q_c , that the thickness of the polycarbonate is as constant as possible. The resulting variations in t_{spot} leads to errors in q_c and even larger errors in the calculated wall-shear stress τ_w .

Finally a 1 mm polycarbonate plate covered by a 0.1 mm PVC foil has been chosen for the wall-shear stress measurement.

7.3.2 Thermal boundary conditions

In section 6.2 the two different boundary conditions have been introduced. In a first step heat fluxes (Neumann boundary conditions) are prescribed at the surface of the solid.

To get an impression of the conditions at the surface of the solid, two different experiments have been simulated. Starting at ambient temperatures for $t = 0$ the solid is continuously heated by the laser for $t > 0$ (laser diameter 2 mm, constant irradiated power distribution across the beam). The heat transfer to the flow q_c is calculated with the help of equation 2.10. The temperature gradient in y -direction is given by the temperatures close to the surface in the fluid. Since the flow conditions are unknown in the wall-shear stress calculation, q_c is calculated additionally with the temperature gradient in y -direction inside the solid that is direct underneath the surface.

Figure 7.23 and 7.24 show the temperature distribution in y -direction at $x = x_{spot}$ and the

heat transfer between solid and fluid in x -direction calculated in the fluid and in the solid as a function of time. The symbols in figure 7.23 and 7.24 represent the position of the grid points.

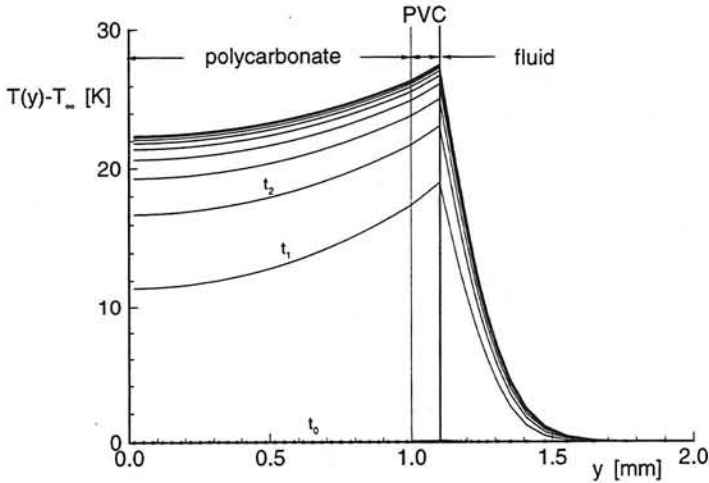


Figure 7.23: $T(y)$ for the solid and the fluid (laser on).

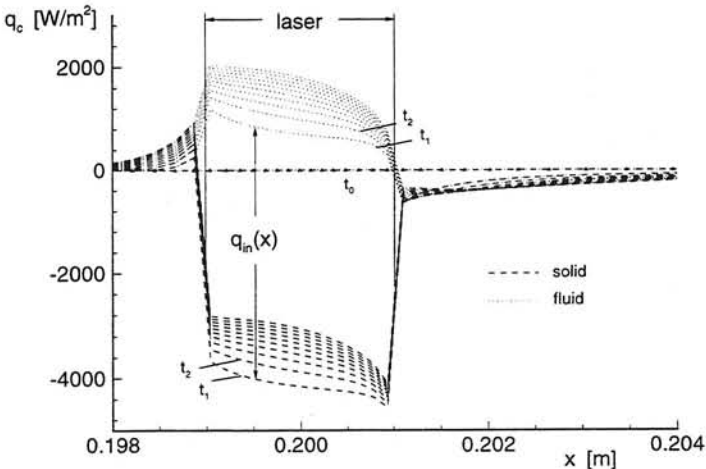


Figure 7.24: $q_c(x)$ in the solid and in the fluid (laser on).

The second numerical calculation simulates a typical wall-shear stress measurement. After

reaching steady state conditions the laser is turned off and the temperatures in the hot spot decreases.

The corresponding $T(y)$ and $q_c(x)$ are given in figure 7.25 and 7.26.

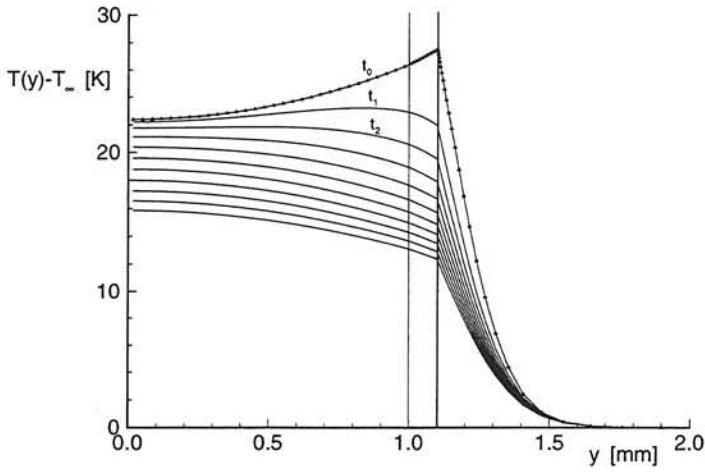


Figure 7.25: $T(y)$ for the solid and the fluid (laser off).

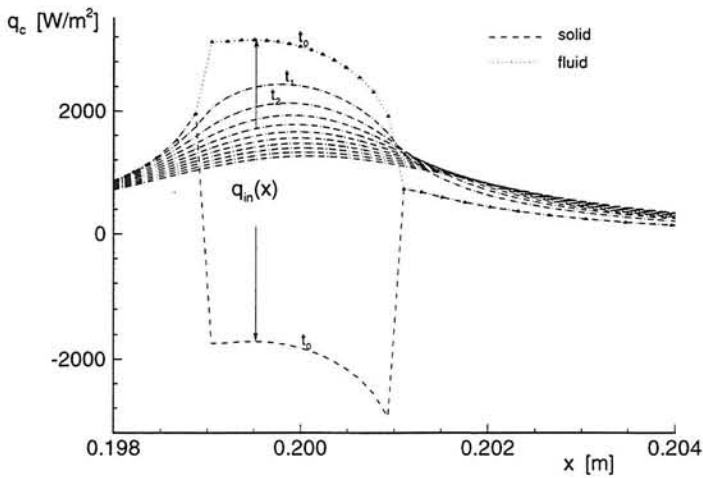


Figure 7.26: $q_c(x)$ in the solid and in the fluid (laser off).

Figures 7.23 and 7.24 show that the temperatures and the heat transfer tend asymptotically

to the steady state conditions. As long as the laser is turned on there is a difference Δq_c between the heat flux calculated for the fluid $q_{c\ fluid}$ and the solid $q_{c\ solid}$ at the same time step. This difference represents the local energy density $q_{in}(x)$ of the laser, which is constant between $x = 0.199\ \text{m}$ and $x = 0.201\ \text{m}$. Δq_c becomes zero after turning off the laser at $t = 0$. This discontinuity in $q_{c\ solid}$ leads to a change in the sign of the temperature gradient in y -direction underneath the surface ($y = 1.1\ \text{mm}$).

In these two simulations Neumann boundary conditions have been used at the interface between fluid and solid. This means that the program calculates the heat flux in the fluid, adds the local power of the laser and prescribes this flux to the solid. In case of a real wall-shear stress measurement first the flow conditions are unknown and second the IR-camera just measures surface temperatures. Thus it has to be checked, whether the Neumann boundary conditions can be replaced by the corresponding Dirichlet boundary conditions, given by the camera measurements. To answer this question, the surface temperatures of the previous temperature decay (see figure 7.25) have been stored. As already described in section 6.2 the program first calculates the temperatures inside the solid with the given surface temperatures at steady state conditions ($t \leq 0$). Afterwards the different Dirichlet boundary conditions are prescribed for each time step $t_1, t_2 \dots$ and the temperature distribution for these time steps inside the solid are calculated. $q_{c\ solid}$ for these temperatures is presented in figure 7.27.

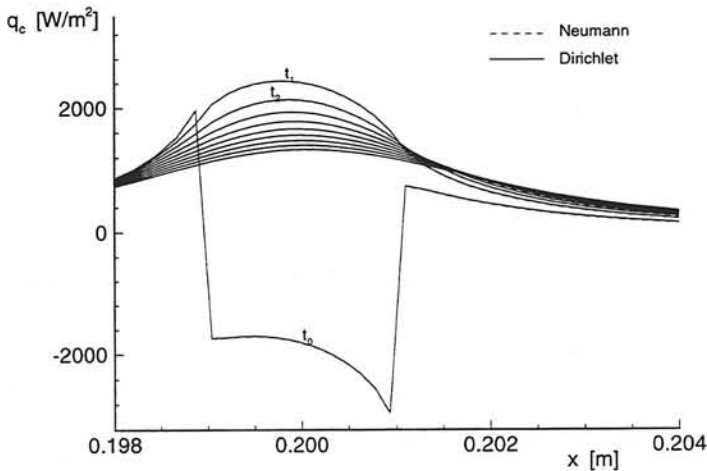


Figure 7.27: $q_c(x)$ in the fluid (Dirichlet + Neumann boundary conditions).

Obviously the two different boundary conditions can be interchanged. This fact makes it possible to determine the unsteady heat transfer to the flow and thus the local wall-shear stress with quantitative IR-thermography.

7.4 Wall-shear stress measurement

This section deals with the measurement of the local wall-shear stress on a flat plate. Since the amount of temperature data in the hot spots to determine the wall-shear stress is quite large, only the wall-shear stress c_f at the test flat plate is presented.

To validate the results the values for c_f are compared with the theoretical c_f values for a Blasius flow (see eqn. 2.27). c_f has been measured at three x -positions on the test plate and for a series of different velocities U_∞ ranging from 4 m/s to 23 m/s.

Figure 7.28 presents c_{fx} against the Reynolds number Re_x .

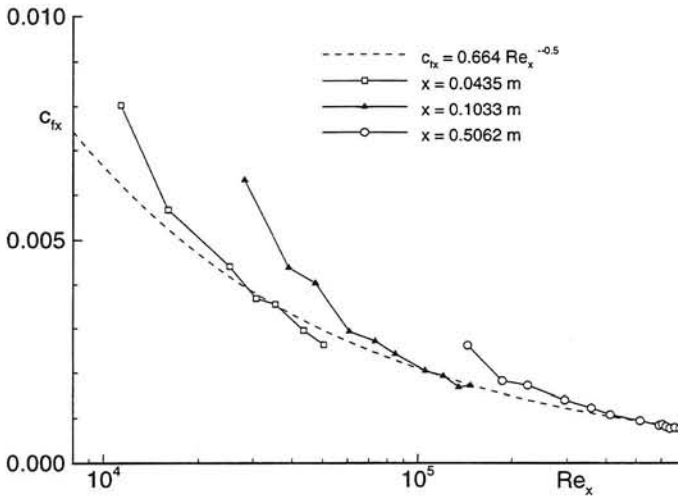


Figure 7.28: c_{fx} on a flat plate.

Figure 7.28 shows that the deviation of c_f from the theoretical value for a constant x -position is decreasing with increasing Re . Thus the error increases with decreasing velocity U_∞ . This effect seems to be caused by natural convection.

Close to heated walls the temperature of a fluid increases locally and therefore the density of the fluid decreases. This variation in the density leads to a flow along the wall in vertical direction opposite to the gravity field. In the considered case an additional velocity component in z -direction is generated, which leads to an additional heat transfer q_{nat} next to the heat transfer q_c caused by the imposed flow (forced convection). Reminding the similarity equation 4.12, the calculated c_f increases due to the increased total heat transfer $q_{nat} + q_c$. Since the ratio q_{nat}/q_c encounters zero asymptotically with increasing U_∞ the accuracy of this measurement technique increases for higher velocities.

To get a better view of the relation between the measurement error Δc_f and the velocity U_∞ ,

figure 7.29 presents the same results of the wall-shear stress measurement in a different way.

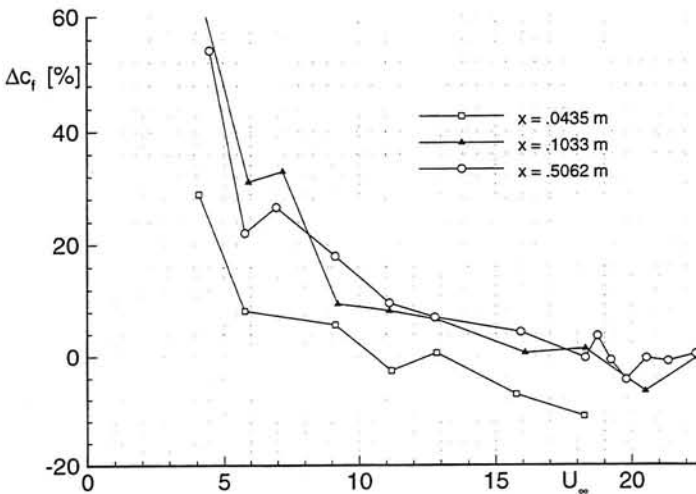


Figure 7.29: Δc_f against U_∞

According to the results in figure 7.29 the error in the wall-shear stress measurement is $\pm 10\%$ for velocities larger than ≈ 10 m/s, which is mostly the case in aerodynamics of aeronautics. Comparing the three lines in figure 7.29, Δc_f for $x=0.0435$ m is on average 15% smaller than at the other x -positions. Since the drop in c_f is not influenced by flow effects like separation at the nose of the plate, which generates a decrease in the wall-shear stress, the reduction is caused by a decrease in the heat transfer q_c to the flow. As already mentioned in section 7.2, for small x -positions a part of the irradiated energy is lost by heat conduction through the aluminium nose of the test plate. These heat losses are rather small ($\leq 4\%$) compared with the heat transfer to the flow, but as the present measurement technique is very sensitive to variations in q_c , the decrease in the measured wall-shear stress can be significant.

Chapter 8

Conclusions

In this report the applicability of the quantitative IR-thermography in wall-shear stress measurements has been evaluated. Since this measurement technique requires experimental as well as numerical considerations, many different issues were considered:

- o relation between wall-shear stress and heat transfer
- o accuracy of temperature measurement with IR-thermography
- o capabilities of the IR-camera concerning spatial resolution and time response
- o numerical calculation of the heat transfer
- o data-processing routines

For validation purposes this measurement technique has been tested in a wind tunnel for the flow along a flat plate.

Measurement technique

In this new measurement technique the heat transfer from a locally heated (hot spot) test object to the flow is determined by measuring the surface temperature of the object. This may either be the steady heat transfer while the heating is turned on or the unsteady heat transfer after the heating is turned off. With the help of this heat transfer the local wall-shear stress can be evaluated. This technique relies on very accurate temperature measurements. The application of quantitative IR-thermography in this technique has led to a series of difficulties.

The accuracy of a temperature measurement of an IR-camera mainly depends on its calibration. With the help of a blackbody the relation between the digital output of the camera and the surface temperature can be determined. This blackbody is also necessary to evaluate the radiative properties of the participating objects like the emissivity of surface of the object, the transmissivity of the wind tunnel wall and the transmissivity of the fluid. In the present investigation an absolute accuracy in the temperature measurement which is below 1% has

been achieved.

This absolute accuracy is limited by the spatial resolution of an IR-camera, which depends on the used lens of the camera. Thus the size of the hot spot must be larger than a certain limit to get an accurate temperature measurement. But on the other hand a too large hot spot violates the assumption of local heating, and requires a much larger laser power to generate the hot spot. Since the size of the hot spot and the time scale of its temperature decay depend on the material of the test object, the wall-shear stress measurement is restricted to solids with a low conductivity.

Data processing

Another difficulty, especially in this technique, is the signal to noise ratio of the temperature measurement. With a "Noise Equivalent Temperature Difference" of $\pm 0.2^\circ\text{C}$, temperature measurements at ambient temperatures require an intensive noise reduction procedure. In steady measurements the noise can be nearly eliminated by averaging the temperatures in time for a constant point in space. Since the output file of one camera image is about 80 kB a compromise between noise reduction and data handling has to be found. For unsteady measurements the temperatures have to be filtered. The choice of the filter depends on the size of the object and the time scale of the phenomena.

The present measurement technique is extremely sensitive to signal noise. In the first place this is due to the scatter in the temperature measurements, which leads to huge errors in the temperature derivatives and thus in the calculated heat transfer to the flow. In the second place the wall-shear stress is proportional to the third power of the heat transfer. This relation amplifies the error in the wall-shear stress approximately with a factor 3. Even if the error of the temperature measurement of the IR-camera is rather small, a sufficient accuracy in the wall-shear stress can only be achieved by a combination of many averaging and filtering steps.

Overall conclusions

- o The quantitative IR-thermography is a reasonably accurate and flexible measurement technique for surface temperatures. But in case of wall-shear stress investigations some limitations have to be accepted.
- o In a laminar flow along a flat plate the wall-shear stress can be measured with an accuracy of $\pm 10\%$ for flow velocities larger than 10 m/s . In slower flows natural convection effects falsify the measurement. But as the flow velocities are much higher than 10 m/s in most aerodynamical investigations, this error can be neglected.

- o To increase the accuracy of the measurement technique, the steady method with a continuous heating can be applied. However the steady method is much less flexible than the unsteady technique. In the steady case the determination of the heat transfer to the flow is becoming much easier, but the irradiated power of the laser must be determined with a beam analyser or with a wall-shear stress reference measurement in a known well-defined flow.
- o This report has been shown that quantitative IR-thermography can be applied to local wall-shear stress measurements, but to transfer this technique from a laboratory environment to large scale flight tests it requires IR-cameras with a much better spatial resolution, time response and signal to noise ratio.

In a next step of our study this measurement technique has to be extended to flows with pressure gradients, higher velocities and turbulence.

REFERENCES

- [1] D.M. Bushnell, J.M. Hefner, (1990) **Viscous drag reduction in boundary layers**, American institute of aeronautics and astronautics, Washington, Progress in astronautics and aeronautics Vol. 123.
- [2] H. Schlichting, (1987) **Boundary layer theory**, McGraw-Hill series, 7th edition.
- [3] B.W. van Oudheusden, (1989) **Integrated silicon flow sensors**, PhD thesis, Laboratory of aerospace engineering, TU Delft.
- [4] R. Siegel, J.R. Howell, (1981) **Thermal radiation heat transfer**, Hemisphere publication corporation, 2nd edition.
- [5] L. de Luca, G. Cardone, G. Carlomagno, (1990) **Image restoration in thermo-fluid-dynamic applications of IR digital imagery**, Infrared technology and applications Vol. 1320, pp. 448-457, SPIE.
- [6] D.L. Balageas, (1993) **Fundamentals of infrared techniques**, ONERA, Châtillon, France Measurement techniques, VKI lecture series 1993-05.
- [7] (1977) **VDI Wärmeatlas**, 3. Auflage.
- [8] G.W. Burns, M.G. Scroger, (1982) **Calibration methods and procedures for thermocouples and thermocouple materials**, NIST, Special Publication 250-35.
- [9] S.v.Patankar, (1980) **Numerical heat transfer and fluid flow**, Series in computational methods in mechanics and thermal sciences.

Series 01: Aerodynamics

01. F. Motallebi, 'Prediction of Mean Flow Data for Adiabatic 2-D Compressible Turbulent Boundary Layers'
1997 / VI + 90 pages / ISBN 90-407-1564-5
02. P.E. Skåre, 'Flow Measurements for an Afterbody in a Vertical Wind Tunnel'
1997 / XIV + 98 pages / ISBN 90-407-1565-3
03. B.W. van Oudheusden, 'Investigation of Large-Amplitude 1-DOF Rotational Galloping'
1998 / IV + 100 pages / ISBN 90-407-1566-1
04. E.M. Houtman / W.J. Bannink / B.H. Timmerman, 'Experimental and Computational Study of a Blunt Cylinder-Flare Model in High Supersonic Flow'
1998 / VIII + 40 pages / ISBN 90-407-1567-X
05. G.J.D. Zondervan, 'A Review of Propeller Modelling Techniques Based on Euler Methods'
1998 / IV + 84 pages / ISBN 90-407-1568-8
06. M.J. Tummers / D.M. Passchier, 'Spectral Analysis of Individual Realization LDA Data'
1998 / VIII + 36 pages / ISBN 90-407-1569-6
07. P.J.J. Moeleker, 'Linear Temporal Stability Analysis'
1998 / VI + 74 pages / ISBN 90-407-1570-X
08. B.W. van Oudheusden, 'Galloping Behaviour of an Aeroelastic Oscillator with Two Degrees of Freedom'
1998 / IV + 128 pages / ISBN 90-407-1571-8
09. R. Mayer, 'Orientation on Quantitative IR-thermography in Wall-shear Stress Measurements'
1998 / XII + 108 pages / ISBN 90-407-1572-6
10. K.J.A. Westin / R.A.W.M. Henkes, 'Prediction of Bypass Transition with Differential Reynolds Stress Models'
1998 / VI + 78 pages / ISBN 90-407-1573-4
11. J.L.M. Nijholt, 'Design of a Michelson Interferometer for Quantitative Refraction Index Profile Measurements'
1998 / 60 pages / ISBN 90-407-1574-2
12. R.A.W.M. Henkes / J.L. van Ingen, 'Overview of Stability and Transition in External Aerodynamics'
1998 / IV + 48 pages / ISBN 90-407-1575-0
13. R.A.W.M. Henkes, 'Overview of Turbulence Models for External Aerodynamics'
1998 / IV + 40 pages / ISBN 90-407-1576-9

Series 02: Flight Mechanics

01. E. Obert, 'A Method for the Determination of the Effect of Propeller Slipstream on a Static Longitudinal Stability and Control of Multi-engined Aircraft'
1997 / IV + 276 pages / ISBN 90-407-1577-7
02. C. Bill / F. van Dalen / A. Rothwell, 'Aircraft Design and Analysis System (ADAS)'
1997 / X + 222 pages / ISBN 90-407-1578-5
03. E. Torenbeek, 'Optimum Cruise Performance of Subsonic Transport Aircraft'
1998 / X + 66 pages / ISBN 90-407-1579-3

Series 03: Control and Simulation

01. J.C. Gibson, 'The Definition, Understanding and Design of Aircraft Handling Qualities'
1997 / X + 162 pages / ISBN 90-407-1580-7
02. E.A. Lomonova, 'A System Look at Electromechanical Actuation for Primary Flight Control'
1997 / XIV + 110 pages / ISBN 90-407-1581-5
03. C.A.A.M. van der Linden, 'DASMAT-Delft University Aircraft Simulation Model and Analysis Tool. A Matlab/Simulink Environment for Flight Dynamics and Control Analysis'
1998 / XII + 220 pages / ISBN 90-407-1582-3

Series 05: Aerospace Structures and Computational Mechanics

01. A.J. van Eekelen, 'Review and Selection of Methods for Structural Reliability Analysis'
1997 / XIV + 50 pages / ISBN 90-407-1583-1
02. M.E. Heerschap, 'User's Manual for the Computer Program Cufus. Quick Design Procedure for a CUT-out in a FUSELAGE version 1.0'
1997 / VIII + 144 pages / ISBN 90-407-1584-X
03. C. Wohlever, 'A Preliminary Evaluation of the B2000 Nonlinear Shell Element Q8N.SM'
1998 / IV + 44 pages / ISBN 90-407-1585-8
04. L. Gunawan, 'Imperfections Measurements of a Perfect Shell with Specially Designed Equipment (UNIVIMP)
1998 / VIII + 52 pages / ISBN 90-407-1586-6

Series 07: Aerospace Materials

01. A. Vašek / J. Schijve, 'Residual Strength of Cracked 7075 T6 Al-alloy Sheets under High Loading Rates'
1997 / VI + 70 pages / ISBN 90-407-1587-4
02. I. Kunes, 'FEM Modelling of Elastoplastic Stress and Strain Field in Centre-cracked Plate'
1997 / IV + 32 pages / ISBN 90-407-1588-2
03. K. Verolme, 'The Initial Buckling Behavior of Flat and Curved Fiber Metal Laminate Panels'
1998 / VIII + 60 pages / ISBN 90-407-1589-0
04. P.W.C. Provó Kluit, 'A New Method of Impregnating PEI Sheets for the *In-Situ* Foaming of Sandwiches'
1998 / IV + 28 pages / ISBN 90-407-1590-4
05. A. Vlot / T. Soerjanto / I. Yeri / J.A. Schelling, 'Residual Thermal Stresses around Bonded Fibre Metal Laminate Repair Patches on an Aircraft Fuselage'
1998 / IV + 24 pages / ISBN 90-407-1591-2
06. A. Vlot, 'High Strain Rate Tests on Fibre Metal Laminates'
1998 / IV + 44 pages / ISBN 90-407-1592-0
07. S. Fawaz, 'Application of the Virtual Crack Closure Technique to Calculate Stress Intensity Factors for Through Cracks with an Oblique Elliptical Crack Front'
1998 / VIII + 56 pages / ISBN 90-407-1593-9
08. J. Schijve, 'Fatigue Specimens for Sheet and Plate Material'
1998 / VI + 18 pages / ISBN 90-407-1594-7

Series 08: Astrodynamics and Satellite Systems

01. E. Mooij, 'The Motion of a Vehicle in a Planetary Atmosphere'
1997 / XVI + 156 pages / ISBN 90-407-1595-5
02. G.A. Bartels, 'GPS-Antenna Phase Center Measurements Performed in an Anechoic Chamber'
1997 / X + 70 pages / ISBN 90-407-1596-3
03. E. Mooij, 'Linear Quadratic Regulator Design for an Unpowered, Winged Re-entry Vehicle'
1998 / X + 154 pages / ISBN 90-407-1597-1





3021858

Wall-shear stresses are highly important in the aerodynamic design of aircraft, because they determine the drag and thus the fuel consumption of an airplane. Due to this importance many different measurement techniques have been developed. Most of these techniques are intrusive, which means that the flow is disturbed by the presence of a measurement probe. The hot film technique is non-intrusive, because hot films measure the heat transfer from an electrically heated surface of an object to the flow, which is related to the wall-shear stress. Using the theory of the hot film technique, we have developed a new non-intrusive wall-shear stress measurement technique, which is based on quantitative IR-thermography. In this technique a hot spot is externally generated by a laser. The surface temperature measurements, from which the heat flux to the flow is derived, is measured externally by an IR-camera. The external heating and the external temperature measurement provides three main advantages:

- * the measurement is non-intrusive
- * the measurement point can easily be varied
- * this technique can be applied in flight tests

This measurements technique has been tested for a laminar flow along a flat plate in a wind-tunnel. The laser generates a hot spot on the plate until the steady state condition is reached. After turning off the laser the IR-camera monitors the temperature decay. From these data the heat flux to the flow and the wall-shear stress can be derived. The results show that it is indeed possible to apply quantitative IR-thermography to measure local wall-shear stresses. The obtained accuracy of the measurement technique is +/- 10% for free stream velocities larger than 10 m/s. However it has to be noted that this technique has some limitations due to the capabilities of the IR-camera, such as the spatial resolution and the signal to noise ratio. In the near future this measurement technique will be extended to flows with nonzero pressure gradients and with turbulence.

ISBN 90-407-1572-6



9 799040 715722

